Czech Technical University in Prague
Faculty of Electrical Engineering
Department of Electromagnetic Field

Microwave Hyperthermia for Treatment of Head and Neck Tumors Controlled by Non-invasive Temperature Monitoring Based on UWB Radar

DOCTORAL THESIS

ONDŘEJ FIŠER

Prague, March 2018

Ph.D. Programme: Electrical Engineering and Information Technology (P2612)
Branch of study: Radioelectronics (2601V010)

Supervisor: Prof. Ing. Jan Vrba, CSc.
Supervisor-Specialist: Doc. Ing. David Vrba, Ph.D.

Prohlášení

Prohlašuji, že dizertační práci „*Microwave Hyperthermia for Treatment of Head and Neck Tumors Controlled by Non-Invasive Temperature Monitoring Based on UWB Radar*“ jsem vypracoval samostatně s použitím literatury, kterou uvádím v seznamu přiloženému k této práci.

V Praze dne 26.3.2018

Podpis autora

Abstract

This dissertation thesis is mainly focused on microwave hyperthermia for treatment of head and neck tumors. This thesis is divided into three parts. Each part represents original scientific contribution to the thesis topic. These parts are as follows:

1. Microwave hyperthermia in head and neck region with definition of the main procedure for the effective multi-applicator proposal.
2. Feasibility study of the non-invasive temperature change detection based on UWB radars for usage in microwave hyperthermia.
3. Combinations of the proposed microwave hyperthermia system and non-invasive differential temperature measurement system based on UWB radar for hyperthermia treatment of head and neck region.

The first part of the dissertation thesis deals with the design of new microwave hyperthermia applicator for treatment in area of head and neck. We carried out a parametrical numerical study of possibilities of the microwave energy focusing the target (tumor) on the frequency 434 MHz using waveguide applicators. The prototype of applicator system was realized and main parameters were measured and compared with the EM simulations.

The second part of this dissertation thesis concerns the investigation of novel approach of temperature monitoring using UWB radar. We derived analytical relationship between transmitted signal intensity and reflected signal intensity from the heated area. Based on this derived relationship we performed set of numerical studies based on a simplified Mason graphs. We conclude that the expected relationship between reflected signal intensity and temperature change is of a linear character. All assumptions were verified by several experiments with a real UWB radar system (in cooperation with TU Ilmenau, Germany). We proved that the UWB radar is able to detect temperature changes in the tissue remotely. According to the numerical simulation results we demonstrated that this method is of sufficient spatial and temperature resolution.

In the third part of this thesis we proposed possible treatment setup which consists of the hyperthermia system and 8 UWB bowtie antennas attached to the patient body. We proved numerically that it is possible to detect the changes up to distance 7 cm from antennas.

Keywords: Microwave hyperthermia, waveguide applicator, UWB radar, non-invasive temperature measurement, head and neck region.

Anotace

Dizertační práce je zejména zaměřena na mikrovlnnou hypertermii pro léčbu nádorů hlavy a krku. Dizertační práce je rozdělena na tři části. Každá z těchto částí představuje originální vědecký přínos k danému tématu. Tyto části jsou následující:

1. Mikrovlnná hypertermie v oblasti hlavy a krku s definováním způsobu návrhu efektivního aplikátorového systému.
2. Studie proveditelnosti neinvazivního měření změny teploty pomocí širokopásmového radaru pro využití v mikrovlnné hypertermii.
3. Kombinace navrženého mikrovlnného hypertermického systému a neinvazivního měření změny teploty v oblasti hlavy a krku.

První část dizertační je věnována návrhu nového mikrovlnného hypertermického aplikátoru pro léčbu v oblasti hlavy a krku. Provedli jsme parametrickou studii fokuzace mikrovlnné energie do cíle (tumoru) na frekvenci 434 MHz v této specifické oblasti. Na základě získaných znalostí jsme navrhli mikrovlnný aplikátor, který je schopen efektivně fokusovat energii do nádoru. Prototyp mikrovlnného aplikátoru byl sestrojen, jeho základní parametry byly změřeny a úspěšně porovnány s výsledky numerických simulací.

Druhá část dizertační práce je věnována výzkumu nového přístupu monitorace teploty pomocí širokopásmového radaru. Odvodili jsme analytický vztah mezi intenzitou vyslaného signálu a odraženého signálu od oblasti se zvýšenou teplotou. Na základě odvozeného vztahu jsme provedli numerické studie pomocí zjednodušeného Masonova grafu. Dospěli jsme k závěru, že vztah mezi intenzitou odraženého signálu a velikostí změny teploty je téměř lineární. Všechny předpoklady byly potvrzeny několika námi provedenými experimenty s využitím reálného širokopásmového radaru (ve spolupráci s Technickou univerzitou v Ilmenau, Německo). Dalšími numerickým simulacemi a měřením jsme demonstrovali, že tato metoda má dostatečné prostorové i teplotní rozlišení pro využití v mikrovlnné hypertermii.

Ve třetí části dizertační práce jsme navrhli možné rozložení 8 širokopásmových antén a čtyř aplikátorů pro mikrovlnnou hypertermii a detekci změny teploty v oblasti hlavy a krku. Z provedených numerických simulací jsme zjistili, že širokopásmový radar je v této oblasti schopen detekovat změny až do vzdálenosti 7 centimetrů.

Klíčová slova: Mikrovlnná hypertermie, vlnovodný aplikátor, UWB radar, neinvazivní měření teploty, oblast hlavy a krku.

Acknowledgments

First of all, I would like to thank to my supervisor, Prof. Ing. Jan Vrba, Ph.D and Doc. Ing. David Vrba, Ph.D, for their valuable consultations and advises during my whole Ph.D studies. It helped me to achieve good results which are presented in this doctoral thesis. My thanks also go to TU Ilmenau (Germany), especially to Dr. Marko Helbig, Dr. Juergen Sachs and Dipl-Ing. Sebastian Ley, for the possibility to be a member of their research team, for valuable consultations and inspirations.

I would also like to thank to the whole Department of electromagnetic field of the CTU in Prague, especially to the head of department Prof. Ing. Pavel Pechač, Ph.D for a very nice and inspiring working environment and support.

Last but not least I thank to my girlfriend Kate for complete support and patience during my whole studies.

Notation

Symbol	Unit	Quantity
S_{11}	(dB)	Module of S-parameter
SAR	($W \cdot kg^{-1}$)	Specific absorption rate
σ	($S \cdot m^{-1}$)	Electric conductivity
ρ	($kg \cdot m^{-3}$)	Tissue density
$\widehat{\boldsymbol{E}}$	($V \cdot m^{-1}$)	Intensity of electric field, vector phasor
x	(m)	Distance
ϑ	(°C)	Temperature
t	(s)	Propagation time
c_t	($J \cdot kg^{-1} \cdot K^{-1}$)	Specific heat coefficient
k	($W \cdot m^{-1} \cdot K^{-1}$)	Tissue thermal conductivity
P_b	($ml \cdot s^{-1}$)	Blood perfusion
Q	(J)	Generated heat
w_b	(K)	Blood temperature
c_b	($J \cdot kg^{-1} \cdot K^{-1}$)	Specific heat coefficient of blood
ϑ_b	(°C)	Blood temperature
SAR_{25}	(%)	Volume fraction of *SAR*
T_{41}	(%)	Volume fraction of temperature
V	(m^3)	Volume
R_f	(m)	Focal point in tissue
λ	(m)	Wavelength
ε_r	(-)	Relative permittivity
c_0	($m \cdot s^{-1}$)	Speed of light
$\hat{\varepsilon}$	($F \cdot m^{-1}$)	Complex permittivity
$\hat{T}$	(-)	Transmission coefficient
$\hat{I}_R$	(V)	Received signal intensity
$\hat{I}_T$	(V)	Transmitted signal intensity
$\hat{\Gamma}$	(-)	Reflection coefficient
$\hat{\gamma}$	(m^{-1})	Propagation constant
f	(Hz)	Frequency

L	(m)	Phantom length
μ	(H·m^{-1})	Permeability
$\hat{Z}$	(Ω)	Impedance
$\hat{\alpha}$	(-)	Temperature coefficient
τ	(s)	Observation time
ε	(F·m^{-1})	Permittivity
ε_0	(F·m^{-1})	Permittivity of vacuum
ε'	(F·m^{-1})	Real part of complex permittivity
ε_r'	(-)	Real part of relative complex permittivity
ε''	(F·m^{-1})	Imaginary part of relative complex permittivity
ε_r''	(-)	Imaginary part of relative permittivity
ε_∞	(F·m^{-1})	Permittivity at infinite frequency
$\Delta\varepsilon_k$	(F·m^{-1})	Dispersion magnitude
τ_k	(s)	Relaxation constant
ω	(s^{-1})	Angular frequency
ζ_k	(-)	Broadening parameter
a	(V)	Transmitting signal in Mason graphs
b	(V)	Receiving signal in Mason graphs
$k_{1,2}$	(-)	Multiple reflections
α	(m^{-1})	Attenuation coefficient
y_d	(-)	Differential signal
y_H	(-)	Signal in case of heating
$\bar{y}_0$	(-)	Mean signal template

Contents

1 INTRODUCTION 1

1.1 THERMOTHERAPY 1
1.2 HYPERTHERMIA 2
1.2.1 BIOLOGICAL EFFECTS OF HYPERTHERMIA 3
1.3 NANOPARTICLES 4
1.4 MAIN AIMS OF DISSERTATION THESIS 4

2 CHAPTER: MICROWAVE HYPERTHERMIA IN HEAD AND NECK REGION 6

2.1 CLINICAL STUDIES OF HYPERTHERMIA IN TREATMENT OF HEAD AND NECK TUMORS 7
2.2 HYPERTHERMIA APPLICATORS FOR HEAD AND NECK REGION 9

3 CHAPTER: APPLICATOR PROPOSAL FOR HEAD AND NECK REGION 11

3.1 INTRODUCTION 12
3.2 NUMERICAL SIMULATION AND TREATMENT PLANNING IN MICROWAVE HYPERTHERMIA 12
3.2.1 TREATMENT PLANNING 12
3.3 APPLICATOR ARRAY WORKFLOW PROPOSAL 13
3.3.1 IMPEDANCE MATCHING OF APPLICATOR TO BIOLOGICAL TISSUE 14
3.3.2 *SAR* DISTRIBUTION IN BIOLOGICAL TISSUE 14
3.3.3 MODELING OF TEMPERATURE DISTRIBUTION 14
3.3.4 SIMULATION RESULTS EVALUATION 15
3.3.5 *SAR* OPTIMIZATION 16
3.4 APPLICATOR REQUIREMENTS FOR HEAD AND NECK REGION 16
3.5 MATERIALS AND METHODS CONCERNING APPLICATOR PROPOSAL 16
3.5.1 FREQUENCIES FOR MICROWAVE HYPERTHERMIA 17
3.5.2 ARRAY OF APPLICATORS/NUMBER OF ELEMENTS 17
3.5.3 SINGLE ELEMENT 18
3.5.4 ROLE OF WATER BOLUS 18
3.6 STUDY I- BENEFITS OF OPTIMIZATION PROCESS ON TUMOR COVERAGE 19
3.6.1 NUMERICAL PHANTOM FOR STUDY I AND II 20
3.6.2 RESULTS AND CONCLUSION OF STUDY I 20
3.7 STUDY II 24
3.7.1 RESULTS OF STUDY II 24
3.8 STUDY III - OPTIMIZATION OF POSITION OF MICROWAVE HYPERTHERMIA APPLICATOR SYSTEM FOR DEEP PLACED TUMORS TREATMENT IN HEAD AND NECK AREA 25
3.8.1 NUMERICAL PHANTOMS USED IN STUDY III 25
3.8.2 RESULTS OF STUDY III 27
3.8.3 CONCLUSION OF STUDY III 29
3.9 STUDY IV - APPLICATOR ROBUSTNESS 29
3.9.1 INFLUENCE OF WATER BOLUS TEMPERATURE 29
3.9.2 INFLUENCE OF NECK DIMENSIONS ON $|S_{11}|$ PARAMETER AND *SAR* COVERAGE 30
3.9.3 RESULTS OF STUDY IV- NUMERICAL VERIFICATION PERFORMED ON 3D ANATOMICAL MODEL 31
3.9.4 CONCLUSION OF STUDY IV 31
3.10 STUDY V – INFLUENCE OF METAL IMPLANTS 31
3.10.1 NUMERICAL PHANTOM FOR STUDY V 33
3.10.2 RESULTS OF STUDY V 34
3.10.3 CONCLUSION OF STUDY V 36
3.11 STUDY VI - NUMERICAL STUDY OF CLINICAL USABILITY OF PROPOSED APPLICATOR 37
3.11.1 PHANTOMS USED IN STUDY VI 37
3.11.2 RESULTS OF STUDY VI 40
3.11.3 AGAR PHANTOM FOR VERIFICATION MEASUREMENT (EXPERIMENTS) 42
3.11.4 LABORATORY PROTOTYPE 43
3.11.5 RESULTS: MODEL VERIFICATION 46
3.11.6 CONCLUSION OF STUDY VI 47

4 CHAPTER: NON-INVASIVE DETECTION OF TEMPERATURE CHANGE USING UWB SIGNAL 49

4.1 THERMOMETRY IN MICROWAVE HYPERTHERMIA 50

4.1.1 INVASIVE THERMOMETRY 50
4.1.2 NON-INVASIVE THERMOMETRY 51
4.2 RADAR IN MEDICINE 53
4.2.1 BREAST CANCER DETECTION 54
4.3 PHYSICAL PRINCIPLES OF DIFFERENTIAL TEMPERATURE CHANGE DETECTION USING UWB SIGNAL 55
4.4 TEMPERATURE DEPENDENCE OF USED PHANTOMS 58
4.4.1 MEASUREMENT OF TEMPERATURE DEPENDENCY OF COMPLEX PERMITTIVITY (OF WATER AND AGAR PHANTOM) AND ITS ESTIMATION VERIFICATION 60
4.5 NUMERICAL SOLUTION IN 1D 63
4.5.1 NUMERICAL 1D STUDIES 64
4.5.2 RESULTS OF NUMERICAL 1D STUDY (1D1) 65
4.5.3 RESULTS OF NUMERICAL STUDY (1D2) 66

5 CHAPTER: FEASIBILITY STUDY OF TEMPERATURE CHANGE DETECTION USING UWB RADAR SYSTEM 68

5.1 INTRODUCTION 69
5.2 RADAR DEVICE 69
5.3 SIGNAL PROCESSING 69
5.3.1 DRIFT AND CLUTTER 70
5.3.2 ATTENUATION CORRECTION 70
5.4 FEASIBILITY EXPERIMENTS 70
5.4.1 ANTENNAS 71
5.4.2 EXPERIMENT I: RESISTOR 71
5.4.3 EXPERIMENT II: WATER HEATING SYSTEM 72
5.5 EXPERIMENT III: HOT STATIC WATER 76
5.5.1 NUMERICAL SIMULATION (USING PROPOSED 1D MODEL) 77
5.5.2 RESULTS FROM THE NUMERICAL MODEL: VERIFICATION BY MEASUREMENT 79
5.5.3 EXPERIMENT III RESULTS 80
5.6 EXPERIMENT IV: DIFFERENTIAL TEMPERATURE IMAGING USING MIMO SYSTEM 84
5.6.1 SPECIAL BREAST SHAPE PHANTOM 84
5.6.2 2D IMAGE RECONSTRUCTION 85
5.6.3 EXPERIMENT AND 2D IMAGING RESULTS 85
5.7 CONCLUSION OF CHAPTER 5 87

6 CHAPTER: COMBINATION OF MICROWAVE HYPERTHERMIA APPLICATOR SYSTEM AND UWB TEMPERATURE CHANGE DETECTION SYSTEM 89

6.1 INTRODUCTION 90
6.2 EXPECTED INTERFERENCE PROBLEMS 91
6.3 THE NUMERICAL FEASIBILITY STUDY IN HEAD AND NECK REGION 91
6.3.1 DIFFERENTIAL TEMPERATURE IMAGING SYSTEM 91
6.3.2 UWB ANTENNAS FOR DIFFERENTIAL TEMPERATURE IMAGING SYSTEM 92
6.3.3 NUMERICAL PHANTOM DESIGN 92
6.3.4 SIMULATION SETUP AND IMAGE RECONSTRUCTION 94
6.3.5 RECONSTRUCTION RESULTS 95
6.4 Chapter 6 conclusion 101

7 CHAPTER: MEASUREMENT OF TRANSMISSION BETWEEN HYPERTHERMIA WAVEGUIDE APPLICATOR AND UWB ANTENNAS 102

7.1 INTRODUCTION 102
7.2 USED HYPERTHERMIA WAVEGUIDE APPLICATOR 102
7.3 TESTED UWB ANTENNAS 103
7.3.1 DIFFERENTIAL FEEDING OF UWB ANTENNAS 103
7.3.2 ANTENNA POSITIONING AND POLARIZATION 103
7.4 RESULTS 104

8 THESIS CONCLUSION 106

REFERENCES 111

AUTHOR'S PUBLICATIONS 121

List of figures

Fig. 1.1 The hyperthermia hallmarks defining six consequences of heat to the tissue taken from [18]. 4
Fig. 2.1 The head and neck anatomy of the numerical model of virtual family. (A) front view, (B) transversal and (C) sagittal cross section. 7
Fig. 2.2 Hypercollar, system for head and neck cancer treatment by microwave hyperthermia (A) and hyperthermia applicator system developed at Chalmers University (B). 10
Fig. 3.1 Waveguide applicator with dimension symbols (A), applicator from the front (B) and from the top (C). 19
Fig. 3.2 Simplified numerical model of neck with average neck dimensions and with five selected targets for hyperthermia treatment. 20
Fig. 3.3 The comparison of the *SAR* coverage of optimized and non-optimized *SAR* distribution for various number of applicators. 21
Fig. 3.4 The 3D distribution of SAR_{25} contour in the phantom for 1-5 applicators of non-optimized (A, B, D, F, H) and optimized field distribution (C, E, G, I). 23
Fig. 3.5 The cumulative *SAR* histograms for all four targets (A-E) and the *SAR* coverage of different number of applicators. 25
Fig. 3.6 Homogenous phantom with inserted cylindrical tumor (A) and 3D anatomical phantom (B). 26
Fig. 3.7 RMS $|E|$ distribution in cross section of the 3D anatomical model: perpendicular polarization (A) and (C), longitudinal polarization (B) and (D). 27
Fig. 3.8 Reflection coefficient sensitivity on distance (A) and the SAR tumor coverage (B). 28
Fig. 3.9 Reflection coefficient for each simulated temperature of the water bolus. 30
Fig. 3.10 The results of $|S_{11}|$ (A) and *SAR* coverage (B) for various neck diameters. 31
Fig. 3.11 Optimized *SAR* distribution (A), (B) and temperature iso-surface contour of T_{41} (C), (D) with marked tumor position. 32
Fig. 3.12 Used numerical phantom (A) stent in artery and (B) stent in oesophagus. 33
Fig. 3.13 Used numerical phantom (A) screws in vertebras and (B) part of cochlear implant. 34
Fig. 3.14 *SAR* distribution in numerical phantom with stent in artery (A) longitudinal and (B) transversal cross section. 35
Fig. 3.15 *SAR* distribution in numerical phantom with stent in oesophagus (A) longitudinal and (B) transversal cross section. 35
Fig. 3.16 *SAR* distribution in numerical phantom with screws in cervical vertebras (A) longitudinal and (B) transversal cross section. 36
Fig. 3.17 *SAR* distribution in numerical phantom with cochlear implant (A) longitudinal and (B) transversal cross section. 37
Fig. 3.18 Homogenous phantom cross-section with applicator array (A) and real modulus of E-field (B). 38
Fig. 3.19 Numerical Human model Ella: (A) targets and (B) applicators position. 39
Fig. 3.20 Numerical model of real patient with tumor (A) and applicators configuration (B). 39
Fig. 3.21 Optimized *SAR* distribution in transversal (index 1), longitudinal cross sections (index 2) and temperature iso-surface T_{41} (index 3 and 4); tongue (A), tumor (A), thyroid gland (C) and real tumor (D). 41
Fig. 3.22 Cumulative optimized *SAR* histogram. 42
Fig. 3.23 Photo of the laboratory prototype, top view (A) and measurement setup (B). 44
Fig. 3.24 Simulated and measured return loss. 45
Fig. 3.25 Measurement setup with two power dividers (D_1 and D_2). 46
Fig. 3.26 Numerical simulation of temperature distributionin homogenous phantom (cross section). 47
Fig. 3.27 Thermograms after power deposition, front view (A) and cross section (B). 47
Fig. 4.1 Layered model of locally heated medium under test (MUT). 56
Fig. 4.2 Estimation of temperature dependency of real part relative permittivity (A) and imaginary part of relative permittivity (B) of agar phantom using equation (4.11) or (4.12). 60
Fig. 4.3 Measurement setup for temperature dependency measurement of complex permittivity of agar phantom (A) and photo of actual measurement (B). 61
Fig. 4.4 Comparison of measured temperature and frequency dependency of distilled water with the model from Ellison, (A) relative permittivity and (B) specific conductivity. 62
Fig. 4.5 Comparison of estimated and measured temperature dependency of relative permittivity (A) and specific conductivity (B) of the agar phantom. 63
Fig. 4.6 Mason graph of the locally heated MUT with three layers (sandwich structure) corresponding to Fig. 4.1. 63
Fig. 4.7 The simulation setup for the frequency response of the 1 °C difference between layers in case of changing of distance between antenna and the second layer. 64

Fig. 4.8 The simulation setup for signal response of different temperature contrasts with constant distance between antenna and the second layer. 65
Fig. 4.9 Results of reflected signal amplitude dependency on the distance from antennas in case of fixed temperature difference of 1 °C. (A) in linear scale and (B) in logarithmic scale. 66
Fig. 4.10 Reflected signal amplitude dependency on the temperature difference between layers for whole frequency spectrum (A), (B) and for selected frequencies with linear behavior (C) and (D). 67
Fig. 5.1 Three tested antennas (A) double ridged horn antenna filled with phantom material, (B) double ridged horn antenna filled with ceramic material and (C) active bowtie antenna with their impulse responses (below each antenna). 72
Fig. 5.2 Schematic measurement setup for preliminary detection experiment with resistor. 73
Fig. 5.3 Reflection change at a distance 0.5 cm from the resistor. 73
Fig. 5.4 Measured impulse response of the phantom. 74
Fig. 5.5 (A) Schematic measurement setup for temperature experiment with heating tube, (B) photo of phantom with the heating tube. 74
Fig. 5.6 Background subtracted radargrams with drift and clutter removal (top) and with additional attenuation correction (bottom). 75
Fig. 5.7 Measured signal difference corresponding to T_1 (A_1) and T_2 (B_1) position, A_2 and B_2 are measured temperatures from T_1 and T_2 probes in case of heating. 75
Fig. 5.8 Scatterplots of measured difference in reflection (T_1 top and T_2 bottom) as a function on actual temperature. 76
Fig. 5.9 Measurement setup for the third experiment. 77
Fig. 5.10 Temperature distribution in the phantom with heating tube (A) and in the phantom only (B). 79
Fig. 5.11 Simulated radargram (A) and measured radargram (B). 80
Fig. 5.12 Radargrams for temperature stabilized phantom (A) and heated phantom (B) after clutter removal, drift and losses elimination (the heating tube was 4 cm from antennas). In (B) the estimated positions of heating tube and temperature sensors (T_1, T_2, T_3) are marked. 81
Fig. 5.13 Radar response in position T_1 (A_1), T_2 (B_1) and T_3 (C_1) with simulated courses (A_2), (B_2) and (C_2). 82
Fig. 5.14 The temperature change dependence of UWB radar reflectivity with linear regression curve of one measurement (A) and three independent measurements (B). Heating tube distance from antennas: Measurement 1 x = 4 cm, Measurement 2 x = 3 cm, Measurement 3 x = 5 cm. 83
Fig. 5.15 Breast phantom with antennas placement (A), active dipole antenna 8x4 mm used for imaging (B) and MIMO measurement setup. 84
Fig. 5.16 Reconstructed 2D results images obtained each 60 seconds. 86
Fig. 5.17 Normalized rooted point intensity $\boldsymbol{I(r0)}$ of reconstructed 2D figures from Fig. 5.16 and corresponding temperature plotted in time dependence. 87
Fig. 6.1 Schema of the microwave hyperthermia system controlled by UWB radar system as a thermometer. 90
Fig. 6.2 Bow-tie imaging antenna (A) and antenna reflection coefficient $\boldsymbol{S11}$ (B). 92
Fig. 6.3 Transmitted Gaussian pulse in time domain (frequency bandwidth 1-8 GHz). 93
Fig. 6.4 Estimated frequency and temperature dependence of relative permittivity (A) and specific conductivity (B). 93
Fig. 6.5 Numerical model of homogenous phantom with 8 UWB antennas (A), numerical model of oncological patient with hyperthermia system with differential temperature imaging system (B) and temperature distribution in tumor after 6 minutes of heating (C). 95
Fig. 6.6 Numerical 3D model of real patient with large tumor (A) and another view with number of antennas (B). 96
Fig. 6.7 2D reconstructed images with marked position and shape of inhomogeneity for the first position (A) and second position (B). (C) is the cross section of reconstructed images (A) and (B) in centre position X=80 mm. 97
Fig. 6.8 Signals received as reflections from heated part in the homogenous numerical phantom for specific antennas. 97
Fig. 6.9 Temperature distribution gained from numerical simulation (A) and reconstructed image (B) with marked neck and tumor position. 98
Fig. 6.10 A_1, A_2, A_3 are temperature distribution after 2,4 and 6 minutes of heating (total power 100 W). B_1, B_2, B_3 are reconstructed images of each temperature distribution. 99
Fig. 6.11 Cross section through reconstructed images $B_{1\text{-}3}$ from Fig. 6.10 when X=80 mm. 99
Fig. 7.1 Measured reflection coefficient of waveguide applicator in the measured frequency band. 102
Fig. 7.2 Used UWB passive antennas of the differential feeding. 103

Fig. 7.3 Measurement setup of different polarisation (Pol) and position (Pos) of applicator and UWB antennas. 104
Fig. 7.4 Transmission between waveguide applicator and various UWB antennas labelled according to the Fig. 7.3. Polarisation is labelled “Pol” and position “Pos”. 105

List of tables

Table 2.1 The treatment responses between radiotherapy only and combination of radiotherapy and hyperthermia from randomized trial from India [26]. 8
Table 3.1 Frequencies usable for microwave hyperthermia [2]. 17
Table 3.2 Tissue properties used in simulation of simplified numerical model of neck [47]. 20
Table 3.3 The overview of the difference between optimized and non-optimized SAR distribution in the Target by SAR_{25} contour. 22
Table 3.4 Overview of SAR_{25} and T_{41} for all test-cases 28
Table 3.5 Maximum temperature in the numerical phantom in with/without metal implant 37
Table 3.6 Targets volume summary 39
Table 3.7 Dielectric and thermal properties used in simulations for frequency 434 MHz [47]. 40
Table 3.8 Phase (P, degrees) and relative amplitude (A,-) setting for each applicator for all targets 42
Table 3.9 SAR_{25} and T_{41} iso-contour target volume coverage 42
Table 3.10 Ingredients quantity of healthy and tumorous tissue phantom [94]. 43
Table 3.11 Measured dielectric parameters of heterogeneous phantom for 434 MHz. 43
Table 3.12 Applicator amplitude and phase settings for measurement 44
Table 4.1 Overview of the usable bandwidth for the variable distances between source and second layer (contrast in temperature). 66
Table 5.1 100 Ω Resistor body temperature-voltage dependence (measured). 72
Table 5.2 Distances of temperature probes from antennas and heating tube 78
Table 5.3 Estimation of Temperature resolution and standard deviation of used Method 84

1 Introduction

Cancer treatment is one of the most challenging fields in medicine. Cancer is the second cause of death in the world (beside illness of cardiovascular system). For the proper cancer treatment the complex and effective treatment is needed. The modern oncological care is starting with more and more increasingly earlier tumor detection and offers several types of treatment. To the "traditional" tumor treatment we can include surgery, chemotherapy or radiotherapy. Nowadays, to these therapies we can also assign the biological (hormonal) therapy which is able to focus the treatment effect more targeted and thus increase the effect of the treatment.

Thanking to the improvements the progress in therapy of the tumor treatment is more accurate in supplying active substances (drugs) or in physical treatment (energy) to the tumor with higher protection for healthy tissues. This enables the possibility of higher doses (of drugs or energy) while maintaining lower toxicity and damage of healthy tissues. It is obvious that the combination of techniques for cancer treatments is opening new possibilities with higher treatment effectiveness.

This thesis is mainly focused on microwave hyperthermia which is a part of the medical thermotherapy. For logical consequences the State of the art of this doctoral thesis is disseminated in chapters 1, 2, 3 and 4.

1.1 Thermotherapy

Thermotherapy is a medical treatment aimed at triggering the many therapeutic effects of heat on patient's body. Treated area is heated up or cooled down to the required temperature according to the treatment application. In this thesis, we would consider only a part of thermotherapy where the tissues are heated. Thermotherapy can be classified in accordance with the size of the heated area in local and regional treatment or according to reached temperature in treated area by using external heating source according to [1].

- Physiotherapy (38 – 41 °C)
- Hyperthermia (41 – 45 °C)
- Coagulation (50 – 60 °C)
- Thermal ablation (60 – 90 °C)

In the further text, we will be dealing only with the hyperthermia treatment.

1.2 Hyperthermia

Hyperthermia is a modern nontoxic adjuvant oncological treatment of tumors. The goal of the hyperthermia treatment is to achieve temperature between 41 - 45 °C (for 40-90 min or longer) [2], [3] and [4] in target area. This temperature leads to tumor cell apoptosis and it is causing greater cell sensitivity to ionizing radiation [5].

The hyperthermia can be divided after the type of heating. For heating of tissues placed on the body surface or deeper (more than 3 cm under skin) the microwaves are very convenient method for heating. Microwaves have ability to enter the human body and propagate in it. The human tissues are from the point of view of electromagnetic (EM) field high loss dielectric materials in which the electromagnetic wave is attenuated while most of lost energy is transformed to the heat.

Commonly used frequencies for microwave hyperthermia are 60-120, 434, 915 or 2450 MHz [2]. The choice of the proper frequency is based on the tumor position and on the volume to be heated. According to Valdagni [6] the factors influencing the outcome of combined radiation and hyperthermia from hyperthermia point of view are thermal variables, number of heat treatments, sequence of hyperthermia and radiation treatments and hyperthermia device.

By the combination with the common treatments (e.g. radiotherapy or chemotherapy) there is an evidence that hyperthermia brings benefits for patients in the monitored parameters as tumor response or 5-years survival rate [6]. According to the phase III trials, the most effective hyperthermia treatment is for tumors in head and neck region [7], breasts region [8] and in pelvic area [9]. The biological principles and the treatment effectiveness are more described by different authors e.g. Horsman [5], Milani [10] or Kubeš [11].

The microwave hyperthermia system consists of the following functional parts:

a) Microwave power generator (generating microwave power usually of 50 - 1000 W)
b) Coaxial line capable transfer of high frequency power
c) Microwave applicator which is matched to the biological tissue
d) Temperature control system

The new scientific activities from the engineering point of view related to the microwave hyperthermia can be divided in to three areas.

1. Temperature measurement during therapy
2. New types of applicator systems with energy focus ability
3. Treatment planning

1.2.1 Biological effects of hyperthermia

The healthy tissue is changing to the tumorous tissue by failure of protective and regulatory processes which are intended to avoid the tumor growth. Each cell has its own regulatory mechanism which are responsible for the recognition of intrusion of the cell cycle. When the cycle intrusion is recognized the cell starts the apoptosis (self-destruction) [10]. When this mechanism fails, the lymphocytes (CD8+T) are activated and the immune system destroys the cancer cell [12]. In case the immune system is weakened the immune response can be insufficient and the cancer cell can get out of control and begins uncontrollably reproducing [13]. For the very fast cancer cells reproduction the environment around cancer cells have to be changed to be able to supply nutrients consumed for cell division (i.e. creating sufficient number of venous) [13].

The positive effect of heat on cancer treatment is not clarified in all aspects from the biological point of view. During the hyperthermia treatment, the tumorous tissue is heating up to temperature over 41 °C and not exceeding temperature of 45 °C [14]. Above 41 °C the cell death is caused by the highest probability by the protein denaturation in membranes.

After hyperthermia treatment, each cell is producing heat stress proteins which are stimulating the protection of the cell and starting apoptosis when the cell is damaged by heat [15]. In the tumor cells, higher number of lysosomal enzymes is produced due to the high nutrient consumption. These enzymes are very heat sensitive and helping to increase the hyperthermia effectivity. The next advantage of hyperthermia treatment is the demonstrably increased sensitivity for radiotherapy of the heated cells which is improving the treatment outcome without any increased toxicity [2]. The increased sensitivity on ionizing radiation is caused by distraction of the cell environment as hypoxia and decrease of pH in cell [16]. This requires the selective heating of cancerous cells with the smallest possible overlap to healthy tissue. This requirement is a new challenge for the designing special applicator systems which are able to do selective heating of cancerous cells as much as possible. The selective heating can be done using the applicators arrays with field steering possibilities. Each region is very specific (different types of tumors, blood circulation and location where it is necessary to heat). When the cancerous tissue is heating up the veins delivering blood for cooling down the tissue are collapsing and it’s also helping the selectively heating of tumors [17].

In the Fig. 1.1 the main six effects of hyperthermia against tumor cells were identified by Issels et al. in article [18] from 2016.

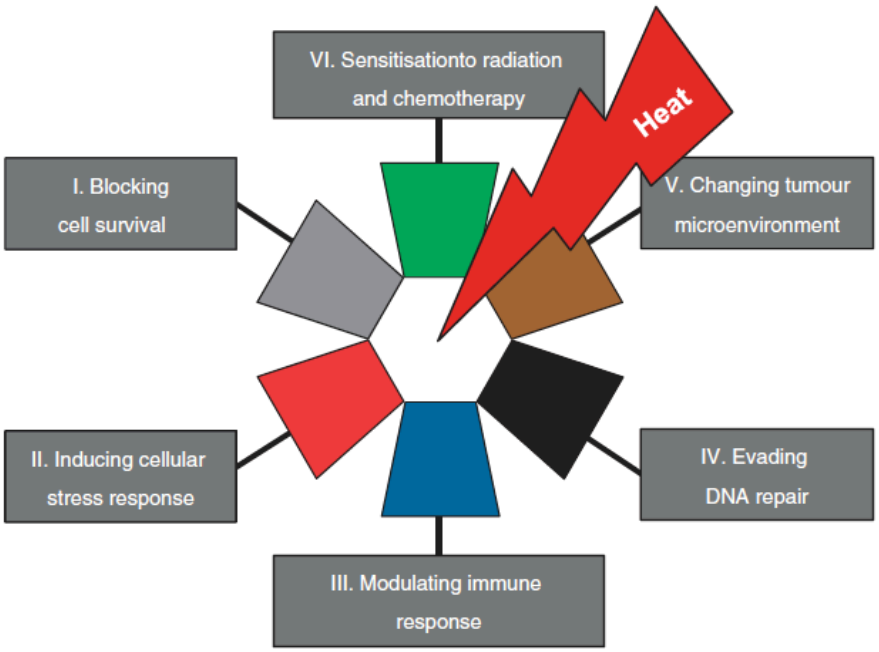

Fig. 1.1 The hyperthermia hallmarks defining six consequences of heat to the tissue taken from [18].

1.3 Nanoparticles

The use of microwave hyperthermia combined with heat sensitive nanoparticles injected into the patient is a relatively new method. The magnetic nanoparticles can significantly increase drug delivery to the tumor or increase field focusing in treatment area [19].

1.4 Main aims of dissertation thesis

This dissertation thesis is mainly focused on new technological approach to clinical applications of microwave hyperthermia in head and neck region. This area of human body is very complicated from anatomical point of view due to many various types of tissues, each having different dielectric and thermal parameters. In relatively small volume are organs and senses important for the patient's life (e.g. brain, eyes, ears, center of stability etc.). It is not easy to deliver electromagnetic (EM) power needed for sufficient temperature increase inside the tumor to be treated with the necessary spatial accuracy. That's why it is very important to have a special hyperthermia applicator equipment for this type of treatment and, as well, to have technology for non-invasive temperature monitoring to perform detailed planning before each treatment to get information about of *SAR* distribution and temperature 3D distribution during the treatment.

In order to reach above mentioned requirements we plan to perform three following main steps for improvement of microwave technology to be used for microwave hyperthermia in head and neck region:

1) Numerical study of *SAR* and heating by using applicators array composed of waveguides for head and neck hyperthermia treatment.
   - Proposal of an efficient applicator system intended for head and neck region with possible EM field steering for better temperature coverage of treated tumor using standard optimization techniques in this field. Realization of the prototype and measurement of the applicators abilities comparing to the EM and temperature simulations.
   - Numerical study of steering of electromagnetic power to the tumors of different size and distance from the body surface using waveguide applicators.
   - Numerical study of potential risk of hot spots creation by oncological patients with metal implants in head and neck region.

Our main research motivation of this dissertation thesis was to propose a power effective applicator for head and neck hyperthermia treatment with sufficient penetration depth for most of large tumors in that region.

2) Noninvasive measurement of differential temperature using UWB radar
   - Analytical derivation of the reflected UWB radar signal dependence on the temperature change in the human body.
   - Numerical 1D study of reflected UWB signal from locally heated material under test (MUT)
   - Phantom proposals with local heating for the feasibility study of the detectability of the local temperature changes
   - Feasibility study of the detectability of the temperature changes in the phantom imitating human tissue.
   - Feasibility study of the possible usage of the UWB radar temperature measurement for the breast hyperthermia treatment. (2D reconstruction)
3) Combination of the applicator system with noninvasive temperature measurement system based on UWB radar for head and neck region.
   - Numerical feasibility study of system for microwave hyperthermia combined with the UWB radar change detection.

2 Chapter: Microwave Hyperthermia in Head and Neck Region

In this chapter we would like to describe the state of the art of microwave hyperthermia in head and neck region. Head and neck cancer is the sixth most common cancer type in the European Union [20]. This is due to smoking and excessive alcohol consumption [20]. Other carcinogens causing cancer in head and neck region are human papillomavirus (HPV) and Epstein-Barr virus (EBV) [20] and [21]. The frequently occurring head and neck cancers, which are appropriate for microwave hyperthermia treatment, are tumors of the vocal cords, thyroid gland and adjacent lymph-nodes [2]. The region of head and neck is containing various tissues with different dielectric parameters. The anatomical cross section with described tissues can be seen in the Fig. 2.1.

The head and neck region is very complicated due to the large amount of different tissues. In the Fig. 2.1 (A) there is a front view of the 3D model of head and neck reconstruct from CT scans of real human. This model is a part of the Virtual Family from Speag [22]. According to the Fig. 2.1 (A) and (B), the head and neck region is intertwined by many big arteries/veins capable of an effective heat dissipation from the treated tumor. The high blood flow is making very difficult hyperthermia treatment in this region. But as hyperthermia is especially efficient for treatment of large and huge tumors, it is often possible to use it technically for the treatment in this area.

In head and neck region there are also present heat sensitive tissues (brain, spinal cord, nervous system or eyes). From this reason, it is necessary to propose a special applicator system for this region with possible EM field steering. Before each treatment it is required to perform treatment planning to optimize the absorbed power distribution and subsequently the temperature distribution for analyzing the expected treatment process.

The Fig. 2.1 (B) shows the cross-section trough the neck area with tissues description. This cross section is divided into four blue rectangles (A, B_L, B_R, C) and one red rectangle. The blue rectangles are indicating areas which are appropriate for the hyperthermia treatment. In the overlap of rectangles A and B there are areas which are very complicated for the hyperthermia heating. This is because of the arteries and veins. The sensitive tissues are situated in the red rectangle.

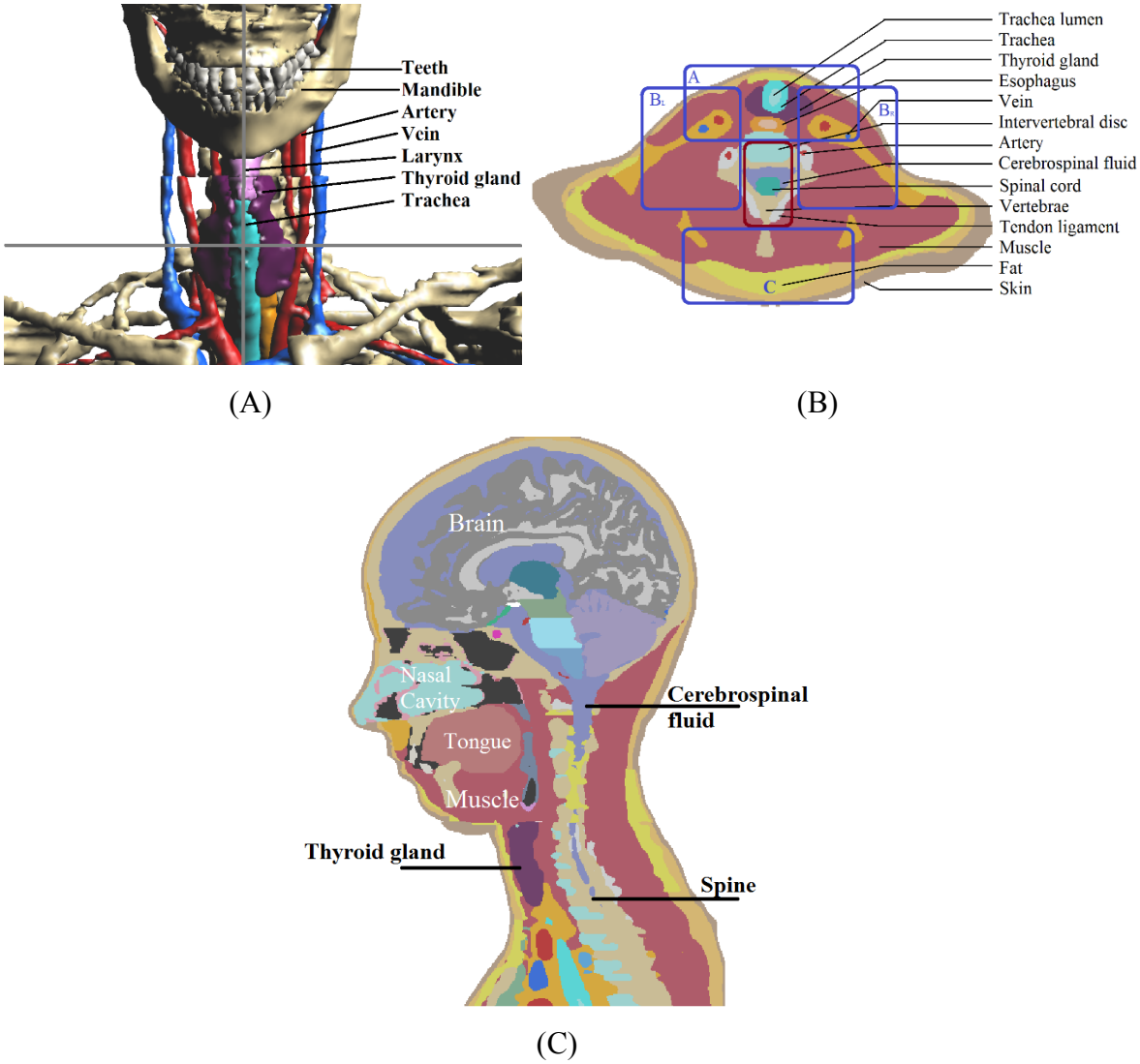

Fig. 2.1 The head and neck anatomy of the numerical model of virtual family. (A) front view, (B) transversal and (C) sagittal cross section.

2.1 Clinical studies of hyperthermia in treatment of head and neck tumors

In this chapter I would like to present an overview of the clinical trials of utilization microwave hyperthermia in oncological treatment of tumors in head and neck region. The first clinical trial (non-randomized) was performed on Villa Flaminia clinic in Rome (Italy) by Arcangeli and his group [23]. In the study 15 patients with cervical nodes cancer (nodes N_2 and N_3) were included. The part of patients was treated by multiple daily fraction (MDF) of radiotherapy (RT) alone and the second part by combination of RT and microwave hyperthermia (HT) with working frequency of 500 MHz. The complete response (after 3 months) of RT alone was 42 % and 79 % of RT in case of combined treatment with HT. After 28 months, the rates of local control were 14 % and 58 % respectively.

Next clinical study (phase III) was carried out by Valdagni et. al. in oncological center in Trento, Italy in 1985-86 [24]. The number of patients was 44 with inoperable metastatic squamous cell lymph-nodes in head and neck region. The average node diameter randomized for treatment was 4.94 cm. The fractional dose of radiotherapy was 64-70 Gy (over 5 weeks). The hyperthermia device was working on frequency 280-300 MHz. The tumor temperature during hyperthermia was maintained at 42.5 °C for 30 minutes twice per week. The response was evaluated 3 months after treatment. The total response was observed by 36.8 % in case of RT alone and 82.3 % of combined RT+HT treatment [24].

Valdagni et. al. is reporting a long-term follow up in the randomized trial. In this study of 41 patients (21 patients treated by RT and 16 by combined RT and HT) from the randomized trial made in 1985 [25] observing 5-year survival chance and late toxicity were evaluated. The 5-year survival chance of only irradiated patients was 0 % and 53.3 % (+/- 21.03 %) for patients treated by combined RT+HT with p-value 0.02.

In the study [26] from Department of radiation oncology in Mumbai, India a randomized trial of group of 54 patients with tumors in head and neck region were reported in 2010. All patients received radiotherapy dose of 70 Gy in 7 weeks. The hyperthermia device was operating at low frequency 8.2 MHz for 30 minutes. The response between group RT and RT+HT are listed in Table 2.1.

Hua et. al from China have done the most extensive phase III clinical study (180 patients) of tumors in nasopharyngeal region using intracavitary hyperthermia. The study is from 2010 and is presented in paper [27]. The authors prescribed for each patient total dose of 70 Gy distributed in 5 weeks. The temperature in treated region was 42.5 °C for 50 minutes twice per week for 7 weeks. The complete response (after treatment) for RT group was 79.5 % and for RT+HT group was 97.1 % (statistically significant for p=0.03). For the 5 years overall survival rate was for RT group 70.3 % while for combined RT+HT group was the rate 78.2 % (not statistically significant p=0.14).

Table 2.1 The treatment responses between radiotherapy only and combination of radiotherapy and hyperthermia from randomized trial from India [26].

	RT		RT+HT	
Response	Number	%	Number	%
Complete	11	42.4	22	78.6
Partial	13	50	3	10.7
No	1	3.8	0	0
Progress disease	1	3.8	3	10.7

In 2014 team of Zhao et al. [28] (China) published the study of 83 patients with tumors in nasopharyngeal region. The patients received complete dose of 70-74 Gy in 7 weeks. For the hyperthermia purposes the commercial capacitive applicator HG-2000 working on frequency 13.56 or 40.68 MHz was used. The temperature of tumor was maintained on 43 °C for 60 minutes. Total number of hyperthermia procedures was 21 within 7 weeks. The 36 months survival rate of RT group was 54 % and RT+HT group 73 % (results were statistically significant when $p<0.041$). This study is very exceptional comparing to the other studies, because also the quality of patients life was observed. In the study 30 parameters defining quality of life (pain, sense, emotional functioning etc.) were monitored. From the results, it is quantitatively obvious that combined therapy RT with HT is improving the quality of life.

According to the results of clinical studies of combined RT and HT available in literature some statistically significant benefits are obvious. The most significant benefits are in treatment of advanced tumors. The studies suffer from low number of patients and also the effect of temperature change was not investigated. Other clinical (phase I – II) study from Trento, Italy is showing the benefits of RT and HT combination which can be found in [29].

2.2 Hyperthermia applicators for head and neck region

Applicator is one of the most important parts of hyperthermia system. Applicators play role like impedance and wave transformers between power source and target (patient body). The microwave applicators are based on waveguide, planar or microstrip structures [2]. The applicator is emitting EM wave which is penetrating to the patient's body. The tissues are loss materials in which the EM wave is attenuated. The absorbed energy is changing mostly to the heat. The created temperature distribution in the tissue is corresponding to the *SAR* in each tissue.

As far as we know there are two applicator systems intended for head and neck region right under development. In type of systems we can include Hypercollar as one good system. This applicator system is one of the first proposed especially for the head and neck region in the Rotterdam medical center. Hypercollar contains 2-3 (depends on version) rings of patch antennas. The proposal of this applicator is described in [30]. In [31] the system is redesigned in the sense of antennas position and electromagnetic point of view. Currently the Rotterdam

group is now developing Hypercollar which is compatible with magnetic resonance imaging systems [32]. The first version (2010) of the applicator can be seen in the Fig. 2.2 (A).

The second applicator system was proposed at the Chalmers University (Sweden). They are developing system for Head and neck hyperthermia treatment based on Time reversal optimization technique described in [33] and [34]. This system is also intended for brain tumors heating by using an array of patch antennas. The system is described in [35] and can be seen in the Fig. 2.2 (B).

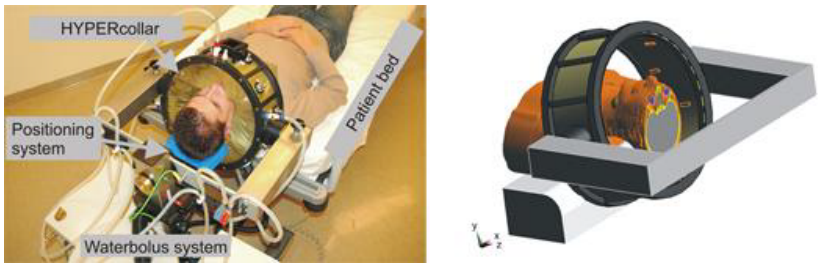

(A)

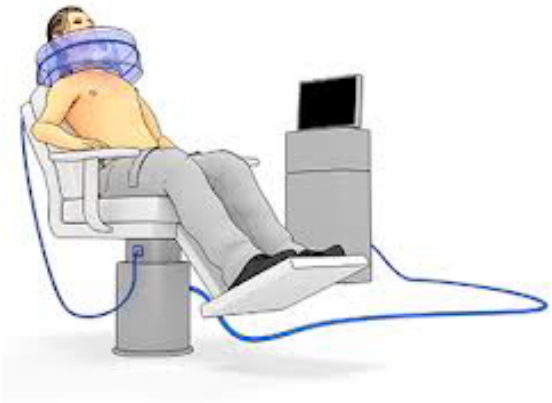

(B)

Fig. 2.2 Hypercollar, system for head and neck cancer treatment by microwave hyperthermia (A) and hyperthermia applicator system developed at Chalmers University (B).

3 Chapter: Applicator Proposal for Head and Neck Region

This chapter is based on following published papers:

- O. Fiser, I. Merunka, and J. Vrba, "Waveguide Applicator System for Head and Neck Hyperthermia Treatment," *J. Electr. Eng. Technol.*, vol. 11, no. 6, pp. 1744–1753, Nov. 2016.
- O. Fiser, I. Merunka, L. Vojackova, and J. Vrba, "Space distribution of SAR and temperature in human body model with tumor using waveguide applicator array," 2014, pp. 484–487.
- O. Fiser, I. Merunka, and J. Vrba, "Optimization of microwave hyperthermia applicator system for deep placed tumors treatment in head and neck area," in *2017 Progress In Electromagnetics Research Symposium - Spring (PIERS)*, 2017, pp. 1733–1738.
- O. Fiser, I. Merunka, and J. Vrba, "Hot Spots by Oncological Patients with Metal Implants in Head and Neck Region", in Progress in Electromagnetics Research Symposium in Prague. Cambridge: Electromagnetics Academy, 2015, pp. 2593-2597.
- O. Fiser, I. Merunka, L. Vojáčková, J. Vrba, Utilization of Waveguide Applicators Combination for Electromagntic Field Focusing, In 24th International Conference Radioelektronika 2014. Bratislava: Slovak University of Technology, 2014.

3.1 Introduction

This chapter is describing the proposal of an applicator system for head and neck region. Patients suffering from advanced primary or metastatic tumors in head and neck region are mostly treated by radiotherapy combined with chemotherapy. According to the results of clinical trials described in the chapter 2.1, the benefits of combination of radiotherapy and hyperthermia are conclusive and thus improving final outcome of whole treatment without increased toxicity.

Most of published clinical trials of combined treatment (RT+HT) were done using non-specific single element applicator for this region [36]. Single element applicator is simple for treatment planning procedure, but in case of very complex region (like head and neck) the multi element applicator offers many benefits. The most important benefit of multi-array applicator is the possibility of electromagnetic steering to improve the power delivery to the target with protection of sensitive tissues with greater achievable penetration depth. According to the results from other authors (who proposed specific applicator presented in [34] and [36]) the composed multi-element antennas for this region brings much new possibilities for the specific treatment of each patient.

3.2 Numerical simulation and treatment planning in microwave hyperthermia

The proposals of the microwave hyperthermia applicator and hyperthermia treatment planning are based on the numerical electromagnetic simulations. For the electromagnetic numerical simulation, mainly two types of the following techniques are used: Finite Difference Time domain (FDTD) and Finite Element Method (FEM).

3.2.1 Treatment planning

Hyperthermia treatment planning is improving the quality of the treatment outcome. Using more complex system composed of more than one antenna it is necessary to perform treatment planning including field optimization to obtain required temperature distribution in the patient. These systems perform treatment planning based on the specific 3D model of the patient composite from CT slices. The planning system predicts the *SAR* and temperature distribution in the patient, optimizes the system properties and through this is improving energy delivery to the tumor, reduces unwanted tissue hotspots and finally whole treatment success. The treatment optimization can be divided into following steps:

1) Simulation of *SAR* distribution created in the area to be treated by each applicator separately.
2) Optimization (adjusting) of the resulting *SAR* distribution by amplitude and phase settings of each applicator. Through this, the energy optimization was enabled in order to cover the largest part of the treated area.
3) Temperature simulation using optimized *SAR* distribution.

Firstly, the field from particular applicators is numerically computed. The main objective of optimization was the adjusting of *SAR* patterns. The results are in the form of phase and amplitude settings of each applicator. Widely used optimization algorithms are Genetic algorithm (GA) and Generalized Eigenvalue Approach (GenEV). There is some planning software currently under development. The VEDO (Visualization Tool for Electromagnetic Dosimetry and Optimization) [37] is being developed in Rotterdam cancer center. The next planning software is being developed in Amsterdam Medical Center and is called HTPS (Hyperthermia Treatment Planning System) [38]. The advantage of HTPS it is that is able to communicate with PACS system generally used for radiotherapy treatment planning. This software will be delivered with new commercial applicator system Alba system 4D.

3.3 Applicator array workflow proposal

For applicator proposal and its properties optimization the simulator of electromagnetic field based on Finite-Difference Time-Domain (FDTD) SEMCAD in version 14.8 (the new version of the software is now renamed to Sim4Life) by Speag company [39]. This numerical simulator is very appropriate for microwave hyperthermia simulations thanks to the possible 3D anatomical models of humans or animals. The workflow of the applicator proposal can be divided into following points:

1) Proposal of the single applicator element.
2) Designation of number of appropriate applicators for head and neck tumors on simple numerical model.
3) Finding the ideal applicators layout (applicators position) in respect to possible EM field steering.
4) Influence of the neck dimensions on *SAR* and temperature distribution and water bolus temperature.
5) Numerical verification of possible usage in patients with artificial or real tumors.

6) Prototype construction and results validation.

For the results evaluation gained from numerical simulation we observed applicator impedance matching ($|S_{11}|$ parameter), *SAR* and temperature distribution in the phantoms.

3.3.1 Impedance matching of applicator to biological tissue

The impedance matching ($|S_{11}|$ parameter) of the applicator is basic parameter, which is describing the ability of the applicator to transfer the energy from the microwave generator of impedance 50 Ω to the area in front of the applicator aperture, i.e. water bolus or biological tissue with higher impedance. The $|S_{11}|$ [dB] complex parameter is defined as a ratio of amplitude of reflected wave to amplitude of transmitted wave. Generally accepted value of reflection coefficient of sufficiently matched hyperthermia applicator is $|S_{11}| \leq -10$ dB [2].

3.3.2 *SAR* distribution in biological tissue

The Specific Absorption Rate (*SAR*) distribution [W/kg] in the phantom is one of the most important and crucial parameter in the workflow of applicator proposal. This parameter is information how much power is absorbed in the treated area and how it is exactly distributed.

SAR parameter is defined according to the following formula [2]:

$$SAR = \frac{\sigma}{2\rho}\left|\widehat{\boldsymbol{E}}^2\right| \tag{3.1}$$

where σ is the tissue conductivity, ρ is the density of the tissue, $\widehat{\boldsymbol{E}}$ is the intensity of electric field.

3.3.3 Modeling of temperature distribution

To information about *SAR* distribution (i.e. contour of SAR_{25}) in the treated area is not a sufficient guarantee that the applicator will be able to achieve the temperature for hyperthermia especially in complicated regions like head or neck which are specific with large amount of flowing blood (through arteries and vessels maintaining brain supply). For this reason it is necessary to perform temperature modeling of each applicator as a part of evaluation.

For the temperature distribution in the biological tissues we used a thermal solver which is included in the SEMCAD X simulator [39]. Thermal solver uses results from the optimized *SAR* distribution as a heat source through Penne's Bioheat equation (3.2). The

Penne's Bioheat equation is describing the temperature behavior in case of microwave hyperthermia with decent accuracy to the reality.

The Penne Bioheat transfer equation:

$$\rho c_t \frac{\delta \vartheta(x,t)}{\delta t} - k \frac{\delta^2 \vartheta(x,t)}{\delta x^2} = P_b + Q_{metabolism} + Q_{external} \quad (3.2)$$

where c_t is specific heat coefficient of tissue, $\vartheta(x,t)$ is temperature at distance *x* and time *t*, *k* is the tissue thermal conductivity, $Q_{metabolism}$ is the heat generated by metabolism itself, $Q_{external}$ is the heat from external source (i.e. from microwave energy generator in case of microwave hyperthermia) and P_b is the blood perfusion coefficient which can be expressed:

$$P_b = w_b c_b (\vartheta_b - \vartheta) \quad (3.3)$$

where w_b is mass flow of blood per volume unit of tissue, c_b is specific heat coefficient of blood and ϑ_b is blood temperature.

Temperature parameters used in temperature calculations (Specific heat capacity, Thermal conductivity and Heat generation rate) are listed in Table 3.7. Blood circulation in arteries and veins are also involved in the calculations.

In the beginning of each temperature simulation, all tissue temperatures were set to 37 °C and the temperature of water bolus was set to 25 °C. The value of the heat transfer coefficient between human body and circulated water was set to 65 [W/m^2/K] [40].

3.3.4 Simulation results evaluation

The effectiveness of the proposed applicator is evaluated through the *SAR* and temperature distribution calculated by SEMCAD X 14.8 [39]. *SAR* distribution is useful especially for technical development and comparison of the discussed applicator system. From a clinical point of view, it is better to utilize the temperature distribution. The thermal simulation keeps us informed about temperature distribution which can be expected during the treatment by the specific setup and applicators setting. The temperature simulation enables us to consider parameters like thermal conduction, blood perfusion and evaluate cooling effect of water bolus.

We propose two parameters SAR_{25} and T_{41} to be used for the evaluation of gained results. SAR_{25} is related to the absorption of energy (eq. (3.4)) and T_{41} is related to the temperature distribution (eq.(3.5)). These parameters are indicating the volume of the lowest value which can be assigned to a lower limit of treatable value. SAR_{25} is a volume

fraction where the *SAR* is greater than 25 % of its maximum in the considered target. T_{41} is the volume fraction of temperature 41-45 °C in the heated target.

$$SAR_{25}\ [\%] = \frac{V_{target}(SAR > SAR_{max} \cdot 0.25)}{V_{target}} \cdot 100\ \% \qquad (3.4)$$

where SAR_{max} is maximum *SAR* in the whole model and V_{target} is the volume of treated target.

$$T_{41}[\%] = \frac{V_{target}(\vartheta > 41\ °C)}{V_{target}} \cdot 100\ \% \qquad (3.5)$$

3.3.5 *SAR* optimization

The important part of the hyperthermia treatment planning is the optimization of the *SAR* distribution. For more complex system composed of more than one applicator, it is desirable to perform treatment planning with the EM field optimization procedure. The planning system predicts the *SAR*, from which the temperature distribution in the patient can be calculated. An optimized *SAR* distribution can be reached by tuning the phase and amplitude of the applicator. For evaluation of our system, the planning software (*SAR* optimizer) as a part of simulator EM-field SEMCAD X based on Genetic algorithm was used. The optimization process is based on the following cost function *L* adopted from [39]:

$$L = \frac{\int_{target} w(x,y,z)\ SAR(x,y,z) dV}{\int_{all-targets} w(x,y,z)\ SAR(x,y,z) dV} \qquad (3.6)$$

where $w\ (x,y,z)$ is a weighting parameter. The weighting function *w* determines the priority and sensitivity of target against the whole phantom volume. The algorithm is searching for maximum of used cost function *L*.

3.4 Applicator requirements for head and neck region

- Reflection coefficient ($|S_{11}|$) of each applicator below - 10 dB.
- Simple construction using water bolus
- Possibility of effective EM field steering to the tumor
- Working frequency 434 MHz

3.5 Materials and methods concerning applicator proposal

In this subchapter we would like to describe the materials and methods which are important for the multi-applicator proposal with the steering possibility of EM energy into the tumor.

3.5.1 Frequencies for microwave hyperthermia

As mentioned in the previous chapter the main task of the microwave applicator is to deliver the microwave energy to the tumorous tissue non-invasively and selectively protect surrounding tissue to ensure safety treatment procedure. Our main goal is to propose an applicator, which can effectively heat the most of treatable tumorous tissues by microwave hyperthermia. The first and crucial task is the right choice of working frequency for the new applicator. Frequencies, which are coming into considerations are so called ISM (Industry, Scientific and Medical) frequency bands and are listed in the following Table 3.1. The size of the focal point muscle phantom was calculated as a half of wavelength ($R_f = \frac{\lambda}{2}$) [2] .

Table 3.1 Frequencies usable for microwave hyperthermia [2].

Frequency [MHz]	**Focal point in muscle tissue R_f [cm]**	**Country**
13.5	87.9	Worldwide
27	56.7	Worldwide
434	4.7	Europe, Russia and Africa
915	2.2	America
2450	0.84	Worldwide

In the literature various frequencies used for microwave hyperthermia treatment of head and neck region can be found. In clinical studies carried out in 80s and 90s described in previous section the used frequency band was 8-500 MHz. In these clinical studies for hyperthermia application only one applicator was used. According to the study in [41] and [42], the ideal frequency for the hyperthermia head and neck applications is 434 MHz. This frequency offers compromise between sufficient penetration depth (for average head and neck size) with required focusing ability for average tumors suitable for hyperthermia treatment in this area.

3.5.2 Array of applicators/number of elements

For our applicator system we choose a waveguide applicator which is intended for superficial hyperthermia. The waveguide applicator is appropriate as a single element for the applicator arrays. The field in front of the waveguide applicator is very homogenous, similar to the planar wave [43]. This feature makes from the waveguide applicator as a suitable element for applicator array with field steering requirements. In this numerical

study, the appropriate number of applicators is determined through the distribution of the *SAR* in the various spherical targets and in the sensitive tissues.

3.5.3 Single element

Simple water filled waveguide with strip-line horn aperture as a single element applicator was chosen. We have designed waveguide applicator for superficial local hyperthermia treatment. In order to minimize the dimensions of the whole applicator, the waveguide is filled with distilled water. The waveguide was elected because of its straight radiation pattern (in case of dominant TE mode) with maximum energy in the center of aperture. And also with the ability to transfer maximum energy of very low energy losses and without irradiation to the surrounding area [44], [45] and [46]. Each single applicator is terminated by a strip-line horn aperture to increase the effective aperture and field homogeneity in front of the applicator.

The single element applicator layout with dimensions can be seen in the Fig. 3.1 (A) - side view, (B) - front view and (C) the top view). The applicator operates on the frequency 434 MHz. The material used for the waveguide applicator body is aluminium while the sidewalls of the strip-line horn are made with acrylic glass. The dimensions of the waveguide are designed for excitation of the dominant mode TE_{10} at working frequency 434 MHz. To match the applicator impedance to the coaxial cable and phantom, two impedance transformers at a distance of $\frac{\lambda_w}{4}$ and $\frac{\lambda_w}{8}$ (where λ_w is wavelength in waveguide) from the coaxial waveguide transition probe are placed. Thanks to that we are able to have applicator adaptability for all types of phantoms.

3.5.4 Role of water bolus

Between patient and hyperthermia applicators a water bolus filled by distilled water is placed. The temperature of the water bolus is controlled to the stable temperature. The water bolus temperature is playing substantial role in the adjusting hyperthermia treatment. The first task of the water bolus is to cool the patient's skin, through this avoiding hot spot formation. The second task is to use a water bolus as a coupling medium between applicator and phantom. The temperature of water bolus is in clinical practice between 20-40 °C [36]. But temperatures below 25 °C are not comfortable for patients. By the temperature of water bolus the penetration depth of treatment can be influenced [2]. With low temperature bolus we are able to cool down the patient skin efficiently and thus shift the temperature maximum

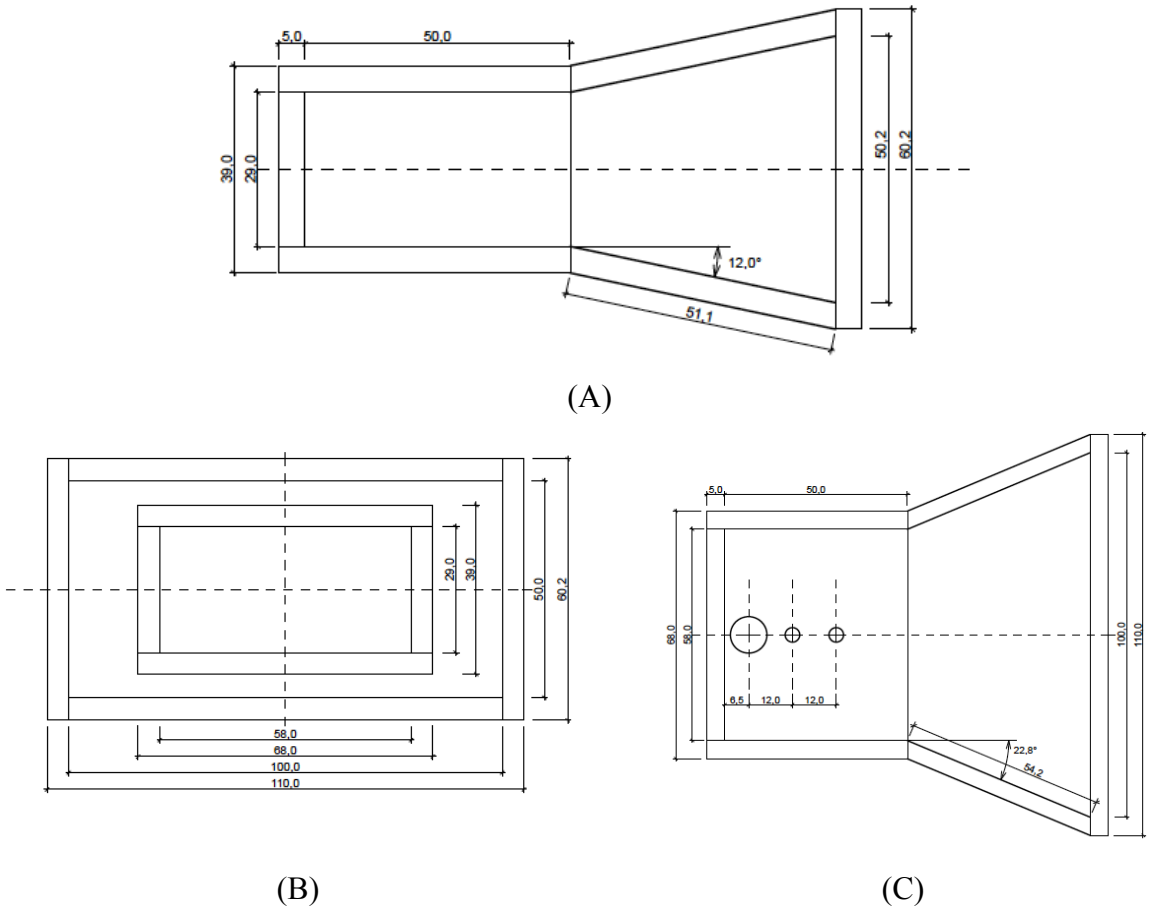

Fig. 3.1 Waveguide applicator with dimension symbols (A), applicator from the front (B) and from the top (C).

deeper [2]. When it is necessary to heat the deeper structures, it is possible to cool down the skin of patient and this enables us to use higher microwave power. Size and shape of the water bolus is affecting two important system parameters - namely the impedance matching and field homogeneity.

3.6 Study I- Benefits of optimization process on tumor coverage

In the Study I, we observed the influence of optimization (amplitude and phase settings of each applicator) on the *SAR* coverage of the target and sensitive tissues for different number of applicators. The optimization process is set to increase the absorbed energy in the target of the treatment and thus save the sensitive tissues. This study is used to choose the appropriate number of applicators with the highest efficiency in the relation to the targets in the head and neck region.

3.6.1 Numerical phantom for Study I and II

For the numerical proposal of the applicator system the simple phantom was proposed. The phantom has cylindrical shape with 120 mm in diameter (phantom can be seen in Fig. 3.2). The body of the phantom is formed by muscle tissue which is representing the neck body (orange color). Into the phantom trachea (air, blue color) and vertebra (green color) with spinal cord (white colour) were inserted. These tissues are representing the most distorting structures to the homogeneity of *SAR* in this region. The dielectric parameters of tissues are listed in the Table 3.2.

Table 3.2 Tissue properties used in simulation of simplified numerical model of neck [47].

Tissue	**Relative permittivity [-]**	**Specific conductivity $[\mathbf{S \cdot m^{-1}}]$**	**Density $[\mathbf{kg \cdot m^{-3}}]$**	**Thermal conductivity $[\mathbf{W \cdot m \cdot °C}]$**
Trachea	1	0	1000	0.03
Muscle	56.9	0.81	1090	0.49
Spinal cord	35.1	0.54	1075	0.51
Vertebra	13.1	0.94	1908	0.32

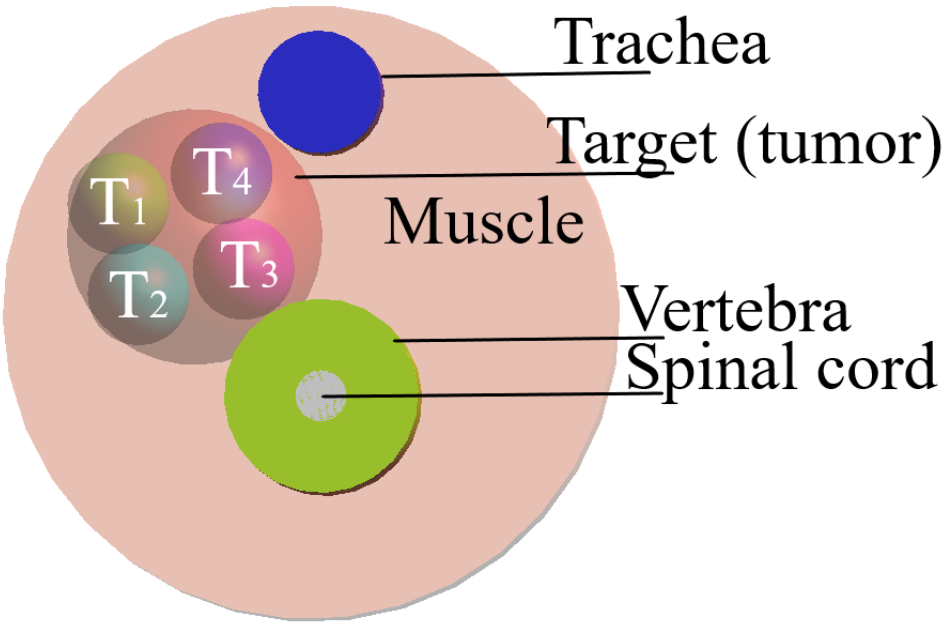

Fig. 3.2 Simplified numerical model of neck with average neck dimensions and with five selected targets for hyperthermia treatment.

3.6.2 Results and conclusion of Study I

In the following graphs (see Fig. 3.3) the iso-*SAR* volume histogram comparison of various number of applicators for the biggest target is presented. The difference between

non-optimized and optimized *SAR* distribution is increasing with higher number of applicators up to four applicators. For five or more applicators, the difference is slowly decreasing. In the Fig. 3.4 there are the iso-contours of *SAR*, which are located in the simulated numerical neck model. From Fig. 3.3 (A) it is obvious that the difference between optimized and non-optimized *SAR* distribution of two applicators is very small (1-2 % of target volume). If you look at SAR_{25} distributions in the Fig. 3.4 (B non-optimized) and (C optimized) you see that the differences are obviously visible. The SAR_{25} is much more focused on the target and the distributing is improving with higher number of applicators. As you can see in the Fig. 3.3, the ideal distribution targeting to the biggest sphere we got in the case of four applicators.

The optimization process allows us to improve the energy distribution and focus on the target. The difference between optimized and non-optimized energy distribution is increasing with the higher number of antennas. This means that with higher number of antennas the treatment planning is more convenient to get the required *SAR* coverage of the target. The differences in the target volume affected by SAR_{25} between optimized and non-

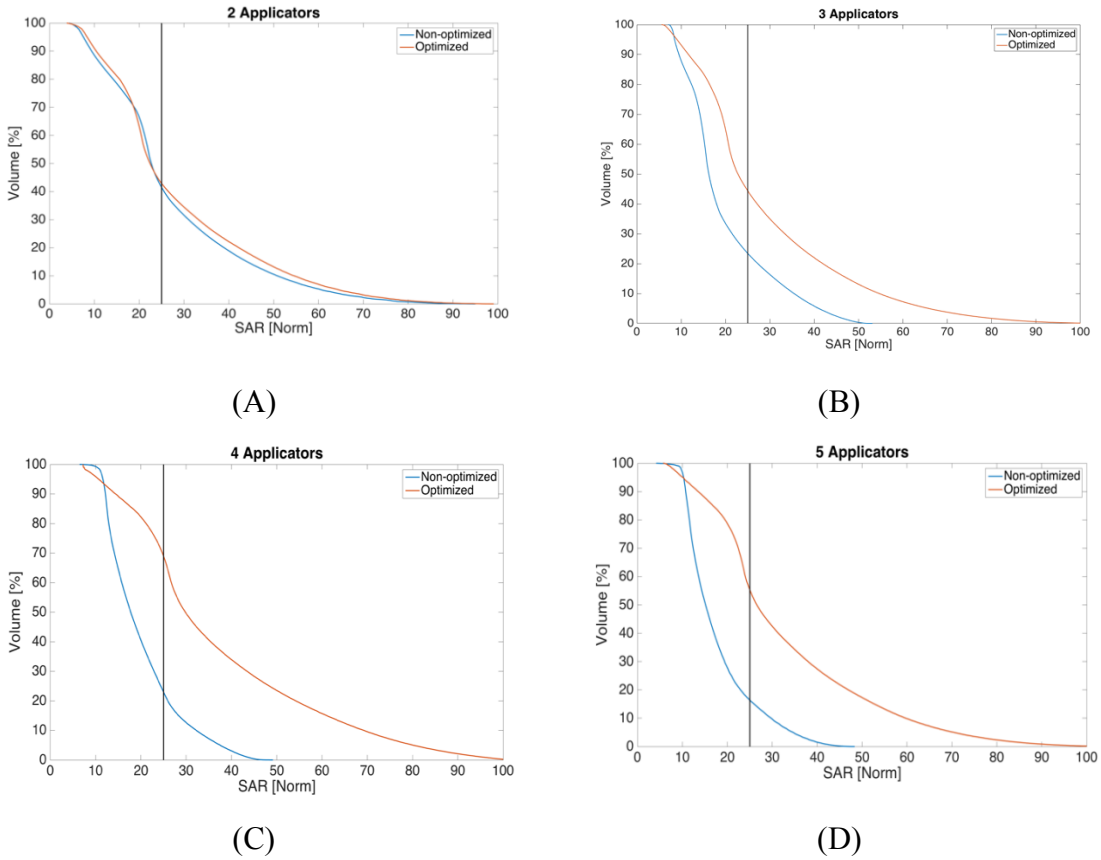

Fig. 3.3 The comparison of the *SAR* coverage of optimized and non-optimized *SAR* distribution for various number of applicators.

optimized are listed in the Table 3.3. The biggest difference was identified for four applicators. In this case the difference between optimized and non-optimized *SAR* distribution was 48 %.

Table 3.3 The overview of the difference between optimized and non-optimized SAR distribution in the Target by SAR_{25} contour.

Number of applicators	Non-optimized SAR_{25} [%]	Optimized SAR_{25} [%]
1	25	-
2	41	42
3	23	43
4	**23**	**71**
5	22	55

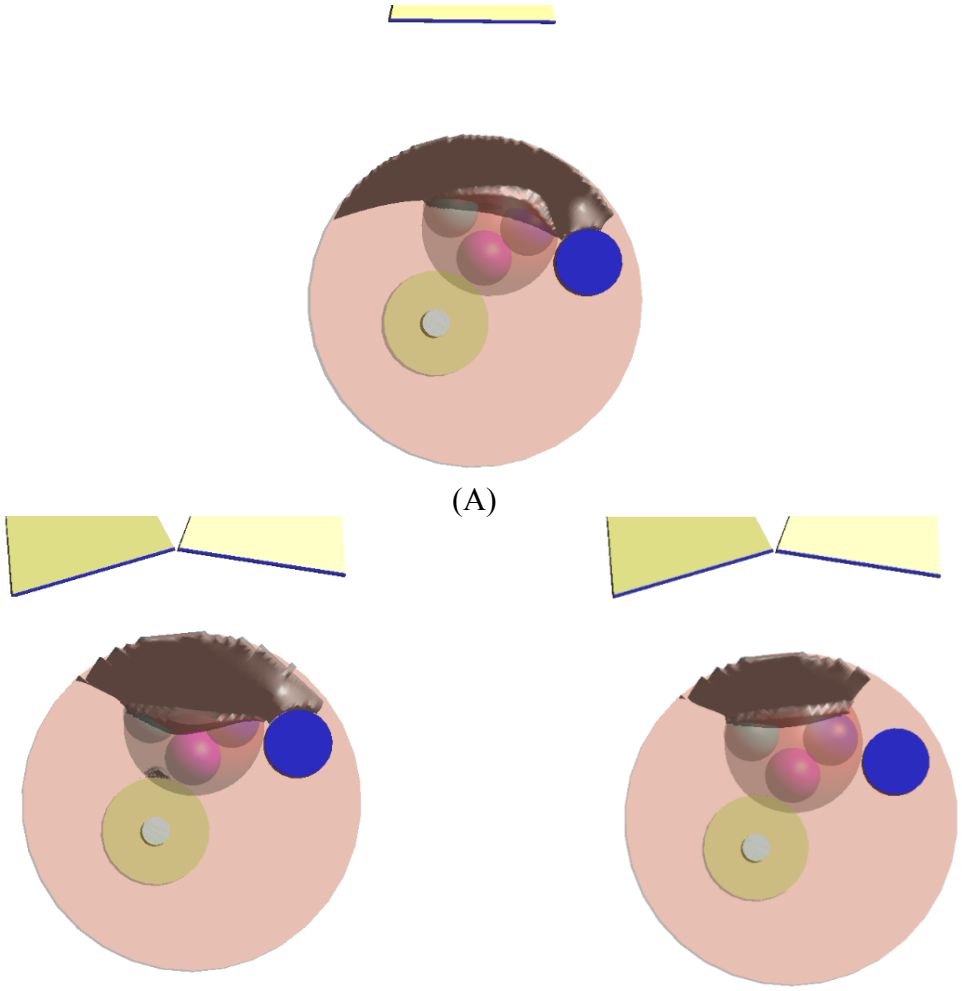

(A)

(B) (C)

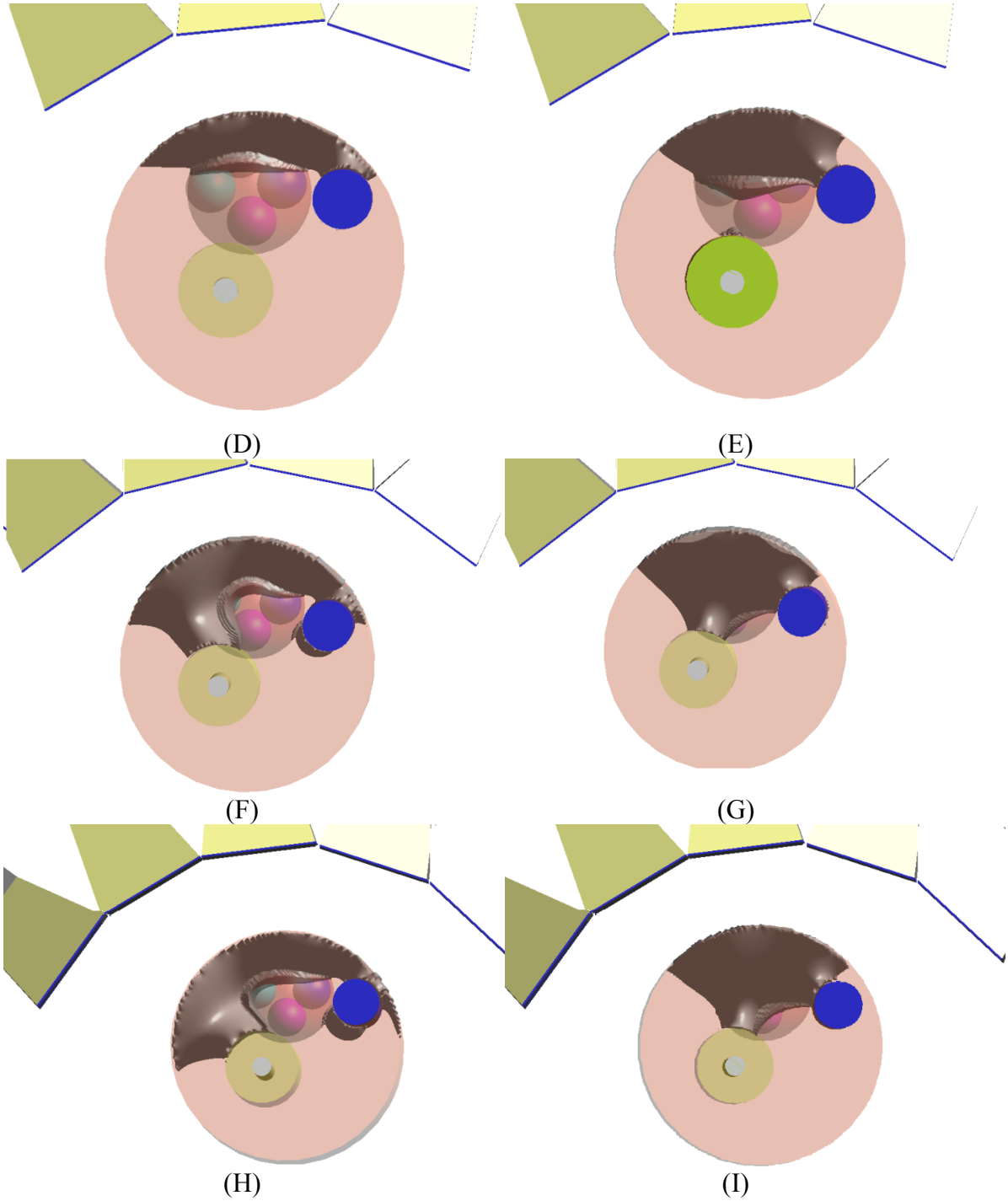

Fig. 3.4 The 3D distribution of SAR_{25} contour in the phantom for 1-5 applicators of non-optimized (A, B, D, F, H) and optimized field distribution (C, E, G, I).

In the following Fig. 3.4 the comparison of the 3D distribution (SAR_{25}) of non-optimized *SAR* (left column) and optimized (right column) in the testing phantom is shown. The grey contour is indicating the SAR_{25} value. These results are extensions supporting the graphs of the *SAR* coverage of the Target by the whole distribution in the phantom. From

these figures it is obvious that the optimization process is substantially improving the focusation of the power on the target in case of the number of applicators above 2.

3.7 Study II

For this study, the simple model of neck (see Fig. 3.2) with 5 various targets corresponding to the possible tumors in this area was also used (described in the previous section). The main goal of this study is to choose the appropriate number of applicators for the hyperthermia treatment in neck region with the highest effectivity and selectivity of the whole applicator system considering the different types of targets.

We performed the electromagnetic (EM) simulation of each applicator separately and after that we applied optimization process to the 5 different targets in the phantom for total 1-5 applicators using optimizer based on the Generalized Eigenvalue Approach.

3.7.1 Results of Study II

In the Fig. 3.5 there are resulting cumulative *SAR* volume coverage histograms gained from optimization process of each target (A-E). The black vertical line is indicating the SAR_{25} which is mostly used in hyperthermia (according to (3.4)). The Fig. 3.5 (A) shows results of the Target (the biggest sphere). The *SAR* coverage is increasing with number of applicators. We found that the highest SAR_{25} value was obtained for four applicators. With more applicators, the *SAR* coverage is decreasing, but also higher absorbed energy in spinal cord occurs.

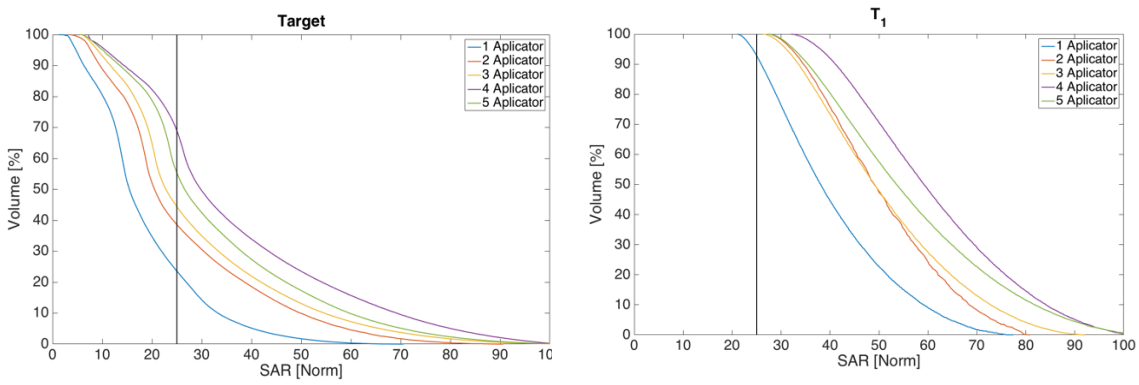

(A) (B)

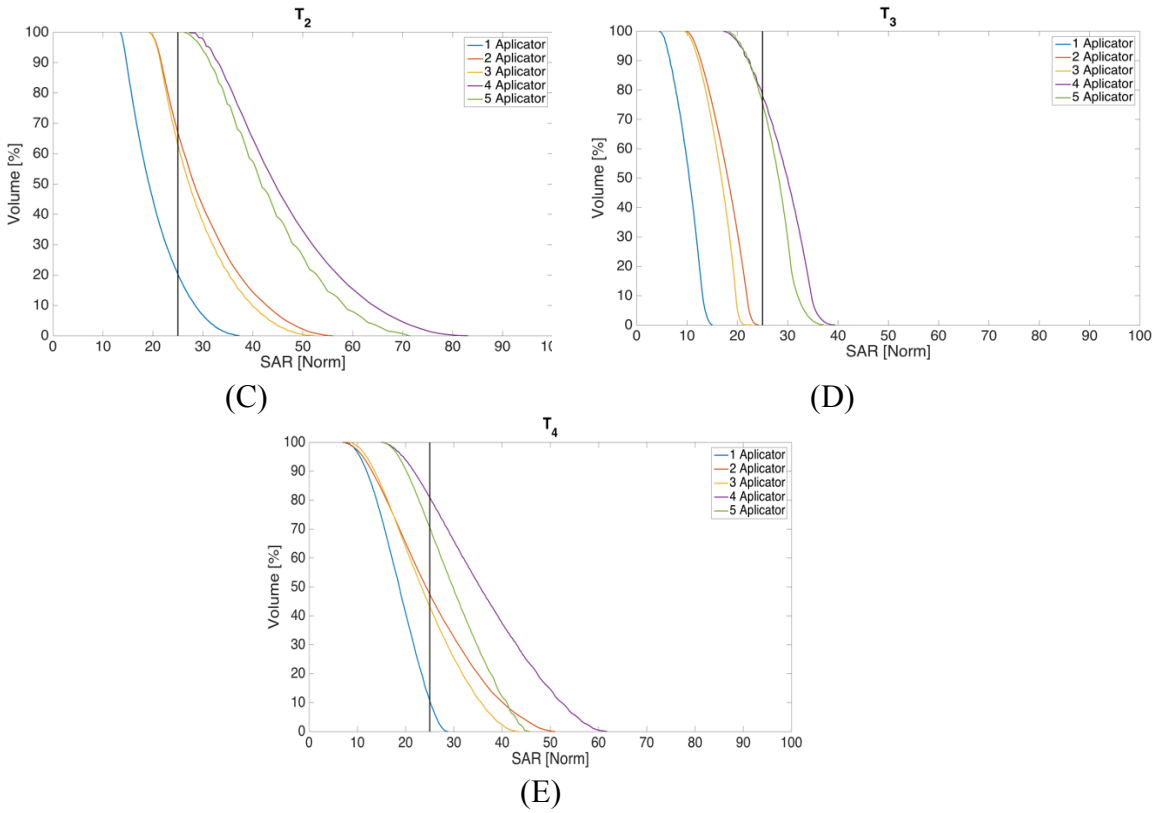

Fig. 3.5 The cumulative *SAR* histograms for all four targets (A-E) and the *SAR* coverage of different number of applicators.

3.8 Study III - optimization of position of microwave hyperthermia applicator system for deep placed tumors treatment in head and neck area

The purpose of this Study III is to optimize the new proposed hyperthermia applicator system intended for the tumor treatment in head and neck region containing four applicators. The two parameters (distance between applicators and the distance between applicators and phantom) were changing when the $|S_{11}|$ and *SAR* distribution to the selected target was observed.

3.8.1 Numerical phantoms used in Study III

For our numerical study of microwave applicator system two phantoms were used: a) homogenous neck phantom and b) 3D anatomical model Ella from Virtual Family 1.2 [22]. Dielectric and thermal phantom properties were taken from IT'IS foundation database [47]. The study workflow was firstly the optimization of the applicator system acting on the homogenous phantom and after that the verification of the best numerical arrangement of the 3D anatomical model.

a) Homogenous neck phantom

The homogenous neck phantom is of 100 mm diameter and is representing average neck dimensions. In the phantom, the sphere (35 mm in diameter) inserted 15 mm under phantom surface represents a target. Homogenous phantom was used for optimization procedure to increase the absorbed energy in circular target imitating tumor. The phantom can be seen in Fig. 3.6 (A). Around the phantom the similar water bolus, used in previous studies was placed.

b) 3D anatomical model

As a second numerical model a 3D anatomical phantom of name of Ella from Virtual Family 1.2 was utilized [22]. Into the phantom, an artificial tumors of diameter 35 mm and 25 mm were inserted. The 3D numerical model with water bolus and array of waveguides can be seen in Fig. 3.6 (B).

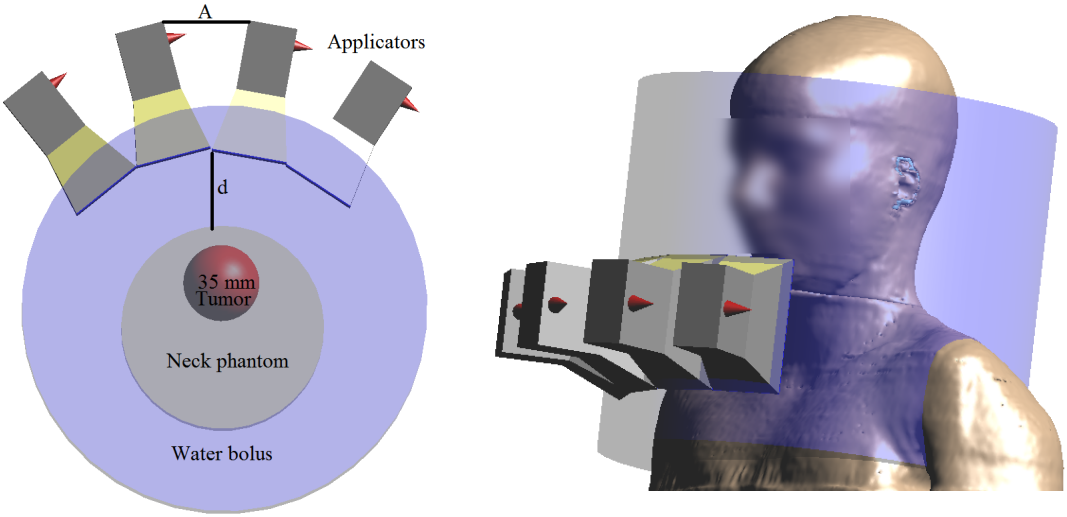

(A) (B)

Fig. 3.6 Homogenous phantom with inserted cylindrical tumor (A) and 3D anatomical phantom (B).

The testing procedure was proposed to find the best solution with the highest treatment effectiveness by changing following parameters.

- Polarization of applicators
- Distance between applicator system and muscle phantom (parameter d) Fig. 3.6

We also tested changes in the distance between applicators (parameter *A* from Fig. 3.6 (A)). When the distance between applicators increased the gap between them was bigger, we observed a massive leaking field between applicators.

3.8.2 Results of Study III

The results from numerical simulation are presented and discussed in this section. We investigate some different applicator arrangements to find the best solution of large deeper-seated tumors.

a) Applicators polarization

We tested two applicators polarization against the phantom position: 1) perpendicular and 2) longitudinal polarization. In the next Fig. 3.7 the distribution of RMS |***E***| field in two cross sections is displayed. For our purposes the field homogeneity in front of applicators is essential for proper function. In Fig. 3.7 (A) and (C) the results for perpendicular polarization are presented and in (B) and (D) RMS |***E***| distribution for longitudinal polarization is plotted. From field distribution it is obvious that the field homogeneity is much more homogenous for perpendicular polarization. Looking at the Fig. 3.7 (C) there is a visible hotspot (marked by white ellipse) on the opposite side of patient's neck. This can be caused by so called surface waves propagating around the patient which are described in [48]. Against these problems, the water bolus is used as appropriate protection. According to our observation the risk of hot spots creation is increasing with the higher number of applicators.

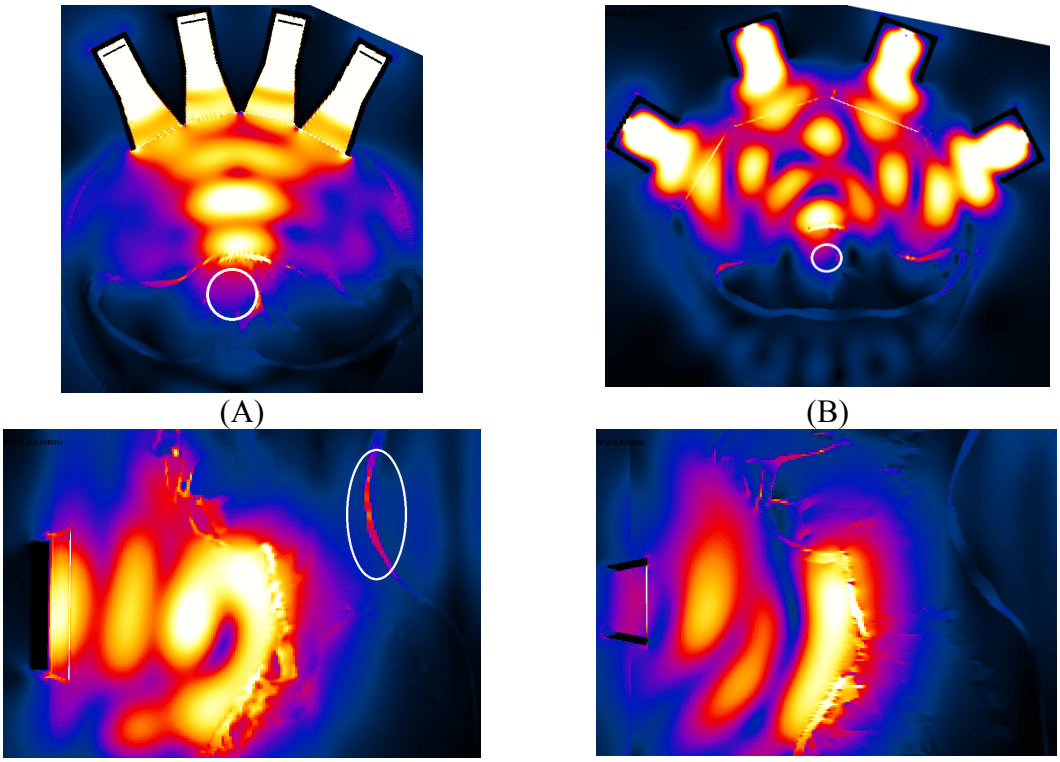

Fig. 3.7 RMS |***E***| distribution in cross section of the 3D anatomical model: perpendicular polarization (A) and (C), longitudinal polarization (B) and (D).

b) Distance between applicator system and muscle phantom (parameter *d*)

In the second part of the Study III of our numerical experiment the distance between antennas and phantom was changed to determine the reflection coefficient and *SAR* distribution in the target (SAR_{25}). We performed simulations for four different distances (step 10 mm) between applicator system and phantom. For this purpose, the homogenous phantom was used. In the Fig. 3.8 (A) the sensitivity of distance change on reflection

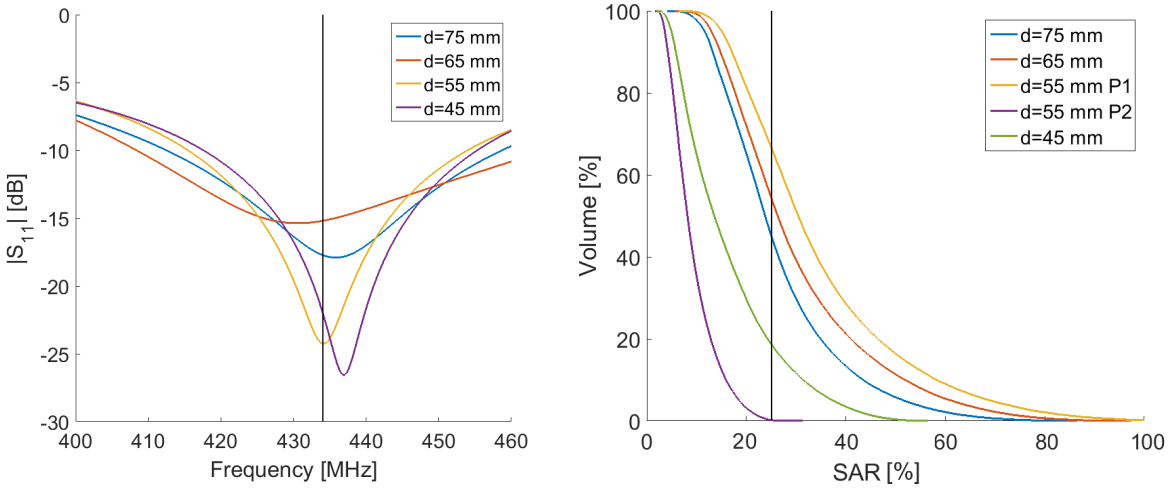

(A) (B)

Fig. 3.8 Reflection coefficient sensitivity on distance (A) and the SAR tumor coverage (B).

coefficient is presented. The working frequency is marked by black line. The best result was achieved when the distance was set to 55 mm (orange line). In that case, the reflectivity coefficient was approximately -24 dB. In the second Fig. 3.8 (B) the *SAR* coverage of the target in the homogenous phantom is shown. The black vertical line is presenting 25 % value of SAR coverage (SAR_{25}). The best result of SAR_{25} coverage was achieved for the distance 55 mm (P1 = perpendicular polarization).

We also tested the longitudinal polarization; in this case, the worst SAR_{25} coverage was achieved (P2 = longitudinal polarization). The values for SAR_{25} and T_{41} for all distances are listed in Table 3.4.

Table 3.4 Overview of SAR_{25} and T_{41} for all test-cases

Distance [mm]	SAR_{25} [%]	T_{41} [%]
75	45.9	71
65	57.2	81
55 (P1)	**71.3**	**94**
55 (P2)	2.7	6
45	18.5	39

3.8.3 Conclusion of Study III

The system was redesigned to gain the improved focusing of *SAR* and temperature distribution in large and deep-seated tumors. Two parameters were changing (applicators polarization, applicators distance between other applicators and numerical model) in order to observe their influence on reflection coefficient, *SAR* and temperature distribution in the treated area. Firstly, the perpendicular polarization related to our numerical phantom was chosen because of obviously more homogenous E-field distribution in front of applicators. This improves the better and predictable system behaviour of higher energy focusation possibility due to the SAR optimization. The second parameter was determined to find the ideal distance between applicators and phantom from the focusing point of view. As the best solution, the distance 55 mm was chosen with of SAR_{25} (71.3 %) and T_{41} (94 %) tumor coverage while the reflection coefficient being – 24 dB, which is fully sufficient for clinical use. This is representing a 22 % increase of the SAR_{25} parameter compared to the original proposal for superficial tumors.

3.9 Study IV - Applicator robustness

The main purpose of the Study IV is the robustness testing of the applicator system. In clinical practice, each patient has different neck dimension and allocated appropriate temperature of water bolus depending on type of treatment. These differences are changing the environment when the applicator is working. We would like to test the sensitivity of the applicator system on the change of the two following parameters in this study.

- Change of water bolus temperature
- Influence of neck dimensions

3.9.1 Influence of water bolus temperature

The influence of water bolus temperature on reflection coefficient for the distance 55 mm between applicators and phantom was numerically tested. We studied the change of reflection coefficient regarding to the temperature (15 - 40 °C) of water bolus used in real clinical praxis. The complex permittivity of water is temperature dependent. The relative permittivity of water was changed according to the Ellison temperature model [92] of complex permittivity which is usable at our frequency.

In the Fig. 3.9, the variations and sensitivity of the reflection coefficient on the water temperature are shown. The reflection curves are decreasing with the higher water bolus

temperature nearly linearly. The resonance was changed by +/- 5 MHz in the used temperature range. It can be declared that the influence of water bolus temperature is low on reflection coefficient which confirms usability of this system for the temperature range which is used in clinical practice.

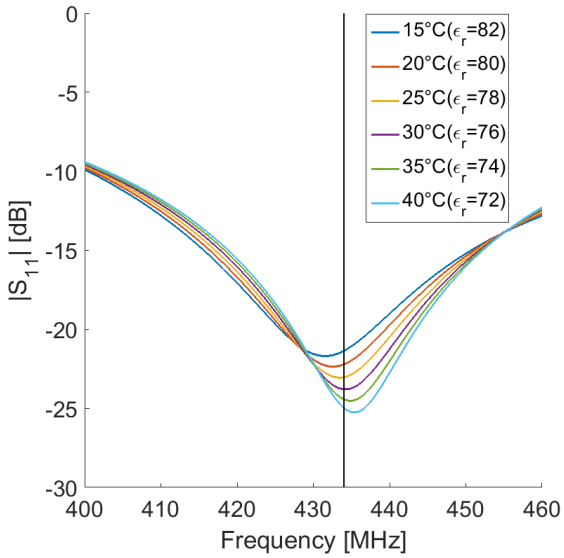

Fig. 3.9 Reflection coefficient for each simulated temperature of the water bolus.

3.9.2 Influence of neck dimensions on $|S_{11}|$ parameter and *SAR* coverage

The aim of the second part of Study IV was to study the influence of the neck dimensions on the reflection coefficient and the coverage of the tumor by *SAR*. The neck dimensions are depended on the body constitution. The neck diameter of the numerical model was studied in the dimension range from 110 – 150 mm when 125 mm is considered as the average one. In the Fig. 3.10 the results of the simulations are presented. The Fig. 3.10 (A) shows the amplitude of the $|S_{11}|$ parameter of the applicator system regarding to the neck diameter, which is in front of the applicators. The impedance matching of the applicator is not dramatically changing with the temperature change. The resonance frequency is slightly changing. In the Fig. 3.10 (B) there is the *SAR* histogram of the target coverage. The differences are in the range of 8 % of volume.

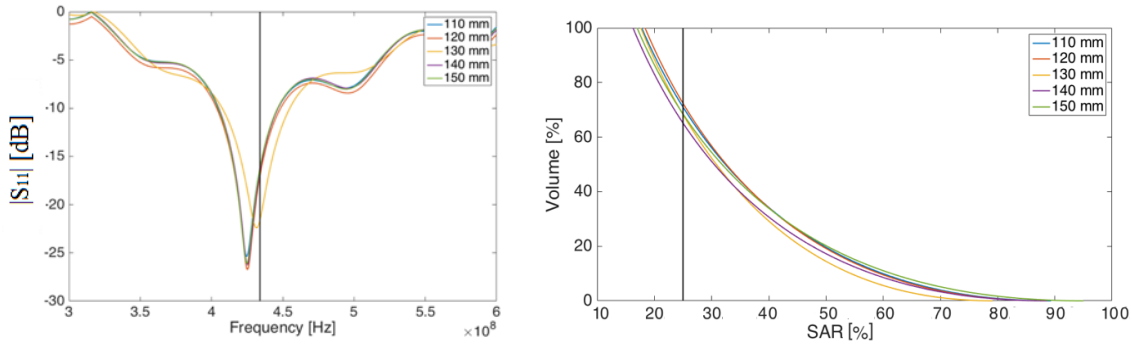

(A) (B)

Fig. 3.10 The results of $|S_{11}|$ (A) and *SAR* coverage (B) for various neck diameters.

3.9.3 Results of Study IV- Numerical verification performed on 3D anatomical model

The proposed applicator system (perpendicular polarization related to the phantom, distance 55 mm from the phantom, water bolus temperature 30 °C) was tested on the 3D anatomical model. In the Fig. 3.11 (A), (B) the results of optimized SAR distribution to achieve the highest impact in the spherical tumor (the tumor position is marked by black circle) are presented. The parameter of SAR_{25} coverage was achieved by a value of 76 %. From optimized *SAR* distribution the temperature was calculated. In the Fig. 3.11 (C) and (D), the temperature iso-contour of 41 °C (parameter T_{41} = 93 %).

3.9.4 Conclusion of Study IV

The main purpose of the Study IV was to optimize the proposed hyperthermia applicator system for focused heating of large and deeply placed tumors in head and neck region. For this purpose, two numerical phantoms with large cylindrical tumors were used. The influence of water bolus temperature on reflection coefficient was also studied. The resonance change dependence on temperature was nearly linear for temperatures between 15-40 °C with the frequency shift +/- 5 MHz. The hyperthermia system was successful for the treatment of large and deep-seated tumors in neck region.

3.10 Study V – Influence of metal implants

Metal implants like wires, titan screws or stents are often considered as contraindication for microwave hyperthermia. Metal implants reacting with the electromagnetic field can cause some phenomena that are affecting and impairing microwave hyperthermia treatment. The presence of metallic implants in the treated area may cause two types of complications.

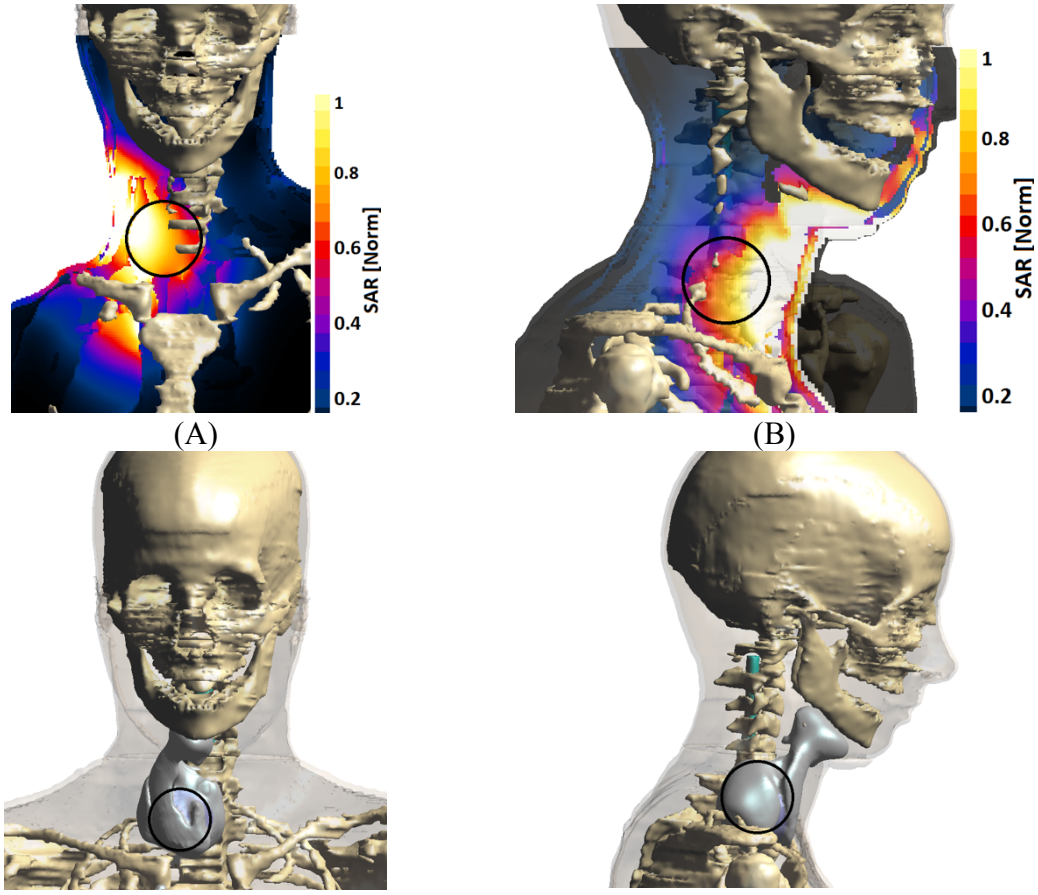

Fig. 3.11 Optimized *SAR* distribution (A), (B) and temperature iso-surface contour of T_{41} (C), (D) with marked tumor position.

1) High temperature increases in the surrounding region of the metal implant

The microwaves propagate through the human tissue where the metal implant is placed, the high frequency energy causes that in the metal implant the voltage is induced and through the metal the current is flowing. Due to the current which is flowing in the metal implant the temperature is rapidly increasing. Due to the good thermal conductivity of metal the temperature simply spread to the tissue and can cause hotspots.

2) Influencing the *SAR* distribution in the treated area

The metal implants affect the expected electromagnetic field distribution. A way to reduce this type of interaction between implants and electromagnetic field is the applicator setting in the way that the vector of electric field intensity is turned perpendicularly to metal implant [2]. This condition is difficult to meet, because in biological tissue the vector of electrical field rotates due to many reflections and transitions between different tissues.

The main goal of the Study V is to determine potential behaviour of a given type of metal implants in high frequency electromagnetic field. The second point is how much the implant can heat the tissue around it. Other goal is how it affects the distribution of electromagnetic field in treatment targets and sensitive tissues like brain and spinal cord in head and neck region.

3.10.1 Numerical phantom for Study V

For simulation purposes of the Study V, the modified human model (part of the SEMCAD X models database) was used. Specifically, the Ella model from Virtual Family 1.2 was utilized [22]. All dielectric parameters were taken from IT'IS foundation material database [47]. Around neck or head we placed the applicator system in a position to meet the practical use conditions.

1) Stent in artery

A stent in the carotid artery is used in case of artery stenosis (constriction). Stent will ensure continuous supply of brain blood and reduce the risk of brain stroke. Stents are made from stainless steel. In the Fig. 3.12 (A) there is numerical model with stent in carotid artery. The stent is 30 mm in length and 3 mm in diameter.

2) Stent in oesophagus

This type of stent is used in case of constriction in oesophagus. This constriction could be cause by tumor or injury. In the Fig. 3.12 (B) one can see position of stent in numerical model. The stent is located in place where oesophagus passes behind the thyroid gland and has 20 mm in diameter and 50 mm in length.

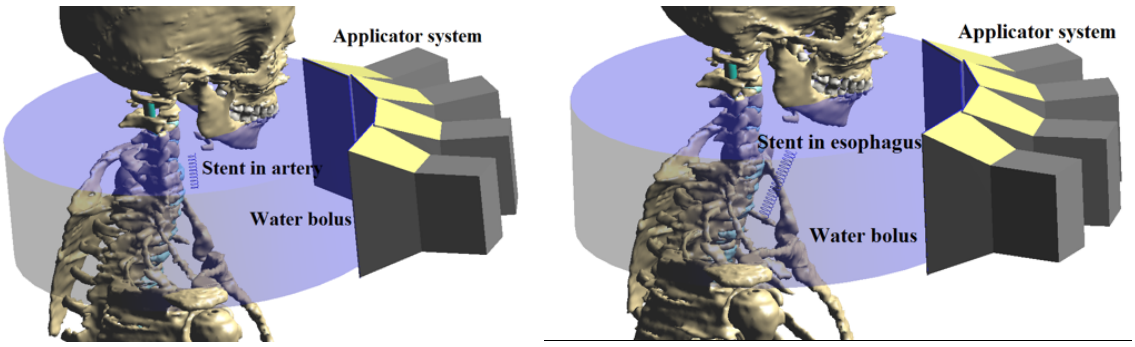

(A) (B)

Fig. 3.12 Used numerical phantom (A) stent in artery and (B) stent in oesophagus.

3) Screws and plate in neck vertebras

Plates with screws are used in case of injuries (fractures) of the cervical vertebras. The screws are drilled through vertebral body and fully fixed. For fixation of neck vertebras the titan plate on the opposite part of vertebras is attached. In our numerical model the screws are drilled through 2nd and 3rd cervical vertebrae (totally 4 screws). Screws are 40 mm long and have 4 mm in diameter (average size for adult human). The titan plate is fastened from the rear of the cervical vertebras. The plate is of the square shape with dimensions 35 x 35 mm, see Fig. 3.13 (A).

4) Cochlear implant

The cochlear implant is a part of device, which helps hearing-impaired people. In our numerical model we modelled wire with electrodes in middle ear only. The numerical model with cochlear implant is shown in the Fig. 3.13 (B).

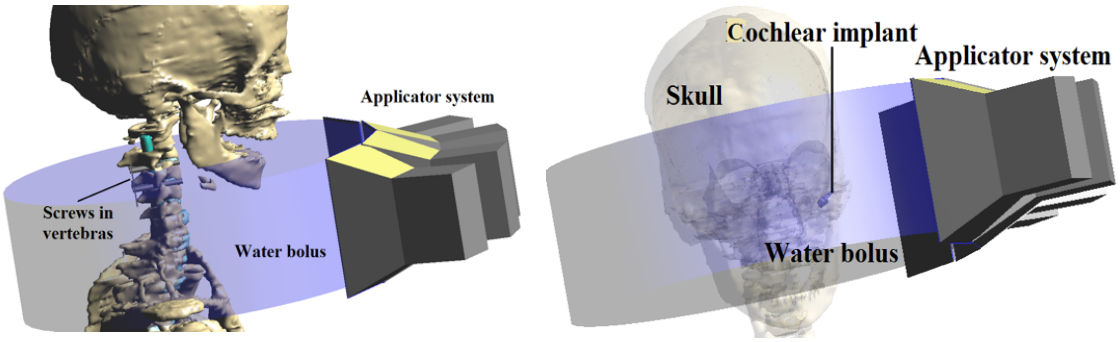

(A) (B)

Fig. 3.13 Used numerical phantom (A) screws in vertebras and (B) part of cochlear implant.

3.10.2 Results of Study V

In the Fig. 3.14 and Fig. 3.15 the results of *SAR* distribution to the human numerical model Ella in the presence of various metal implants are plotted. All *SAR* values shown in the figures are normalized.

1) Stent in carotid artery

Results for stent in carotid artery are in the Fig. 3.14. The green rectangle is designated area, where the metal stent is placed. It is worth noticing that the maximum value of *SAR* values in the figure is located around the metal stent in carotid artery. Incurred hotspots are locally separated. This is caused by the relatively large distance between turns of stent.

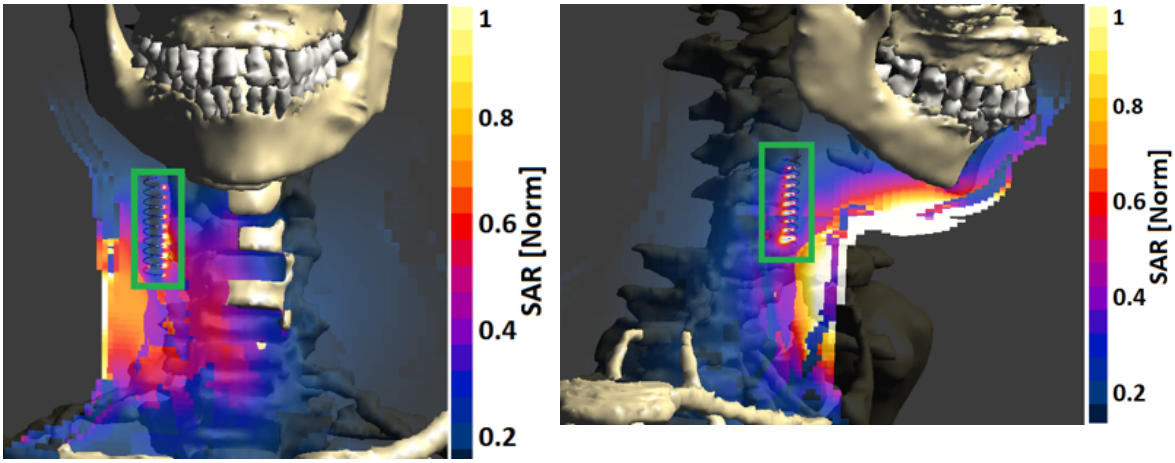

(A) (B)

Fig. 3.14 *SAR* distribution in numerical phantom with stent in artery (A) longitudinal and (B) transversal cross section.

2) Stent in oesophagus

Stent in oesophagus behaves similarly as stents in carotid artery. In the Fig. 3.15 the results from simulation are shown (green rectangle indicates stent position in the cross section). Hot spots are located around the stent turns. The hot spots are fused together. This is due to less distance between turns.

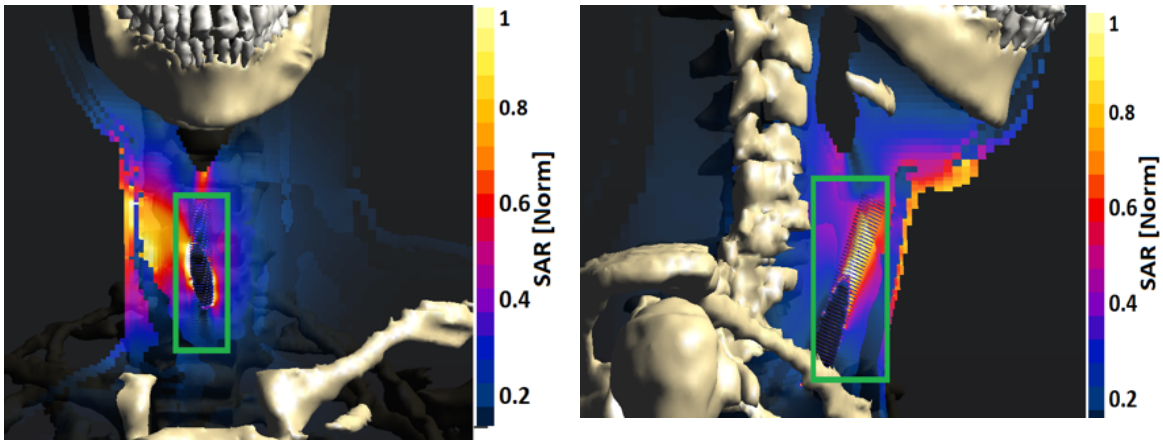

(A) (B)

Fig. 3.15 *SAR* distribution in numerical phantom with stent in oesophagus (A) longitudinal and (B) transversal cross section.

3) Screws in neck vertebras

In the next Fig. 3.16 the results in the case of the screws and plate in the cervical spine are shown. In the Fig. 3.16 (A) there is a cross section where the screws begin. The unwanted hotspots have highest values in the cross section. In the Fig. 3.16 (B) there is longitudinal cross section, where in the green box is showing the hot spot formation on the titanium plate.

Hot spots around screws in cervical vertebras are locally increasing temperature in spinal cord.

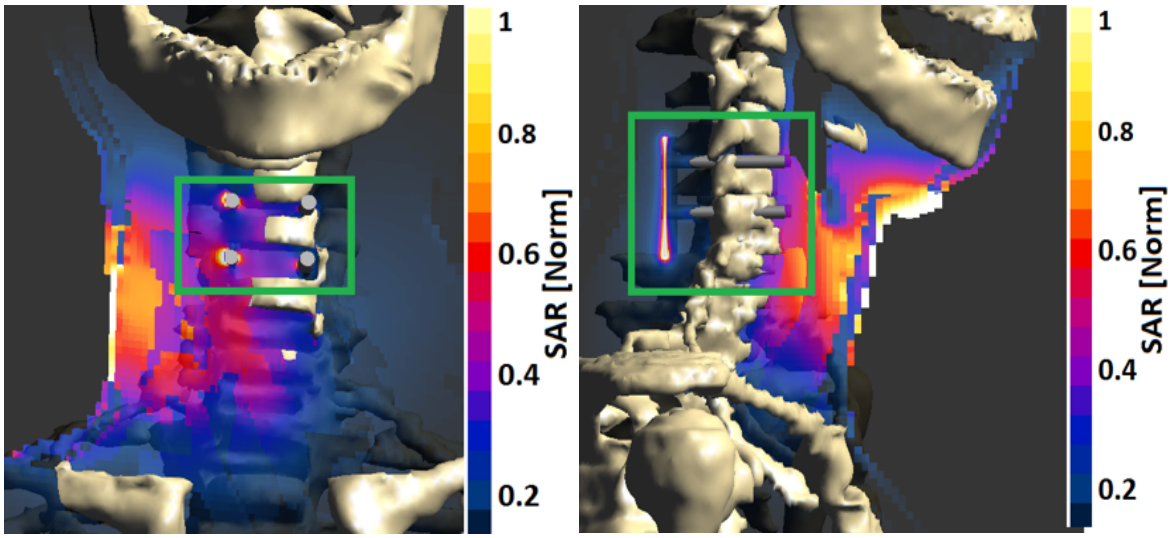

(A) (B)

Fig. 3.16 *SAR* distribution in numerical phantom with screws in cervical vertebras (A) longitudinal and (B) transversal cross section.

4) Cochlear implant

Another examined metal implant is cochlear implant. The implant consists of two parts. The first part is a conductor, which provide signal from the middle ear. On this wire there is no critical or significant SAR value. This is because the conductor is perpendicular to the electric field intensity vector. The second part of used cochlear implant is a conductor with electrodes, which is headed by a spiral in the middle ear. According to our numerical simulations the results are shown in the Fig. 3.17. There is a very significant hotspot formation just in this part of implant.

3.10.3 Conclusion of Study V

Metal implants behave similarly like an antenna. When we exposed metal implant to high frequency electromagnetic field the heating due to current flows was caused. If patient with metal implants underwent hyperthermia treatment of head and neck region by our

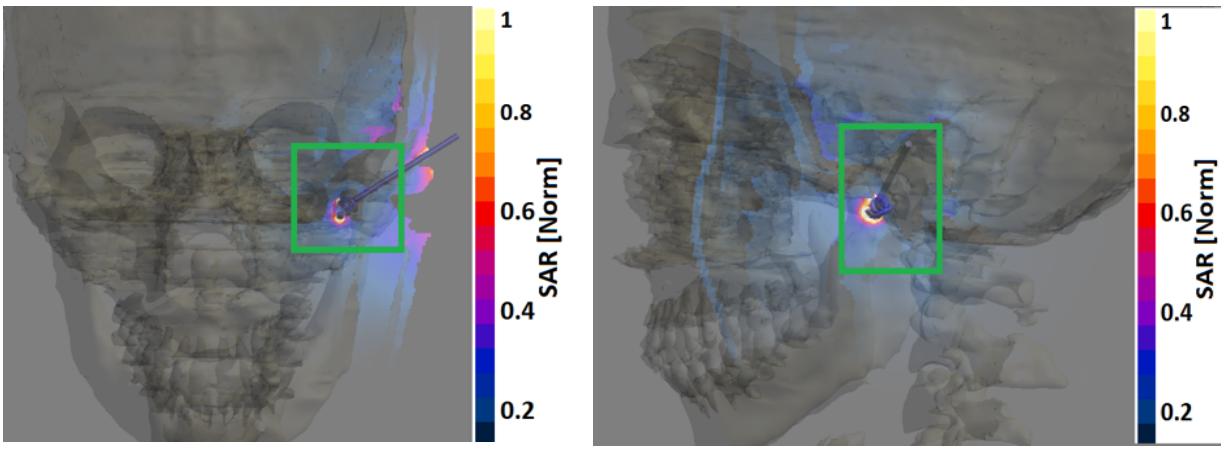

(A) (B)

Fig. 3.17 *SAR* distribution in numerical phantom with cochlear implant (A) longitudinal and (B) transversal cross section.

hyperthermia applicator system, there would be a large risk of hotspots near to implants. We formulate this conclusion for all tested implants. Some implants (cochlear implant or screws in the cervical spine) can significantly endanger patient health and irreparably damage the organ in the implant nearby. The maximum temperature in case of the implant presence are presented in Table 3.5.

The only possibility how to reduce the risk of unwanted hotspot is to ensure that the intensity of electric field is perpendicular to the metal implants. It is not so easy, because the electrical fields in biological tissue are extremely complicated.

Table 3.5 Maximum temperature in the numerical phantom in with/without metal implant

Type of implant	NO implant maximum temperature	Maximum temperature with implant
Stent in carotid artery	45 °C	64 °C
Stent in oesophagus	46 °C	59 °C
Screws in neck vertebras	44 °C	54 °C
Cochlear implant	45 °C	82 °C

3.11 Study VI - numerical study of clinical usability of proposed applicator

In this chapter we would like to study the clinical usability of proposed applicator system for head and neck in clinical practice.

3.11.1 Phantoms used in Study VI

For the design and testing of an applicator system, three numerical phantoms were used. Within these phantoms, the ability of electromagnetic field focusing into various treatment

targets and consequently temperature distribution was studied. In the Table 3.6, the summarizing information of targets volume is shown. To meet input parameters read Table 3.7.

a) Homogenous phantom

The circular homogenous phantom is composed of 2 different parts (muscle and tumor). Dimensions of heterogeneous phantom are 160 mm in diameter and 250 mm in height. In phantom an artificial cylindrical tumor (20 mm in diameter) is placed 10 mm under the surface. The applicator setup is based on results of the previous studies. In the Fig. 3.18 (A) there is the cross section of the system with homogenous phantom and the Fig. 3.18 (B) the distribution of E-field in water bolus and phantom with no optimization is shown.

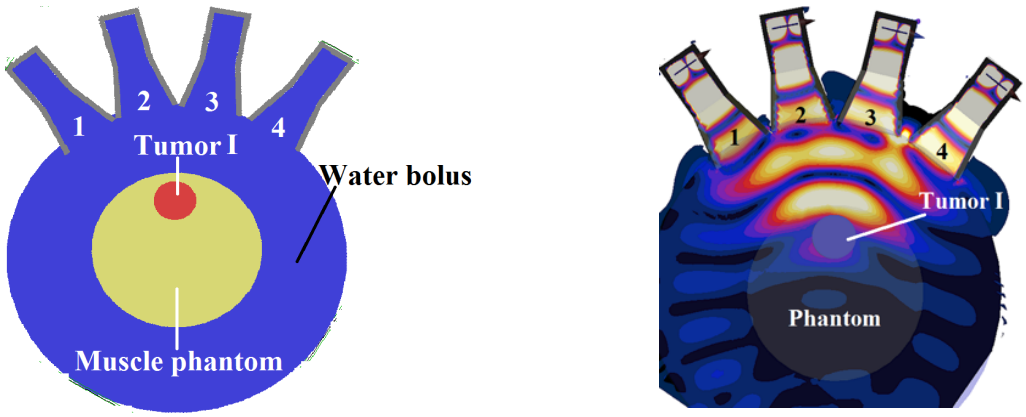

(A) (B)

Fig. 3.18 Homogenous phantom cross-section with applicator array (A) and real modulus of E-field (B).

b) Human model Ella

We used "human model part" of the SEMCAD X models database [22]. For our purposes, the modified human model with name Ella from Virtual Family 1.2 was utilized. Around the neck we placed proposed applicator system with water bolus. Using this numerical model we choose three different targets:

- Thyroid gland
- Tongue
- Tumor II (18 mm under skin)

Each target has a specific shape and position (see Fig. 3.19 (A)). The detail of the array localization is obvious from Fig. 3.19 (B).

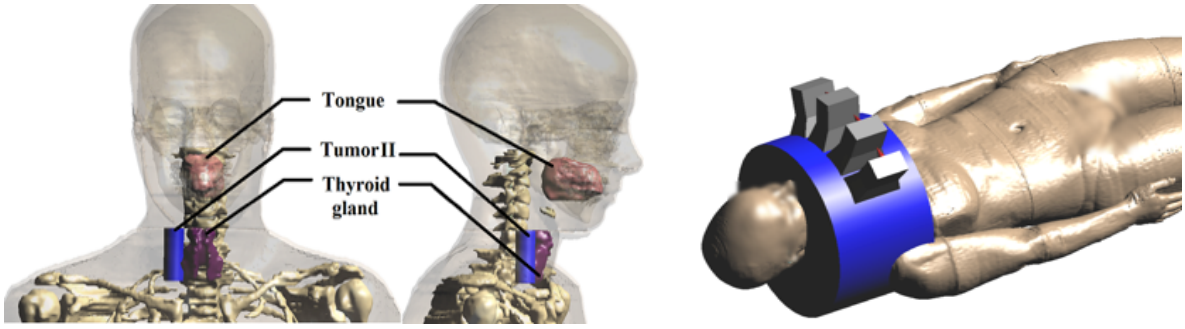

(A) (B)

Fig. 3.19 Numerical Human model Ella: (A) targets and (B) applicators position.

c) Real patient model

The function of our proposed array of applicators we verified using the model of a real patient that was adopted from [47]. The volume and size of tumor is so large that it cannot be appropriately covered by a single aperture only [50]. Our proposed applicator system is more convenient for the utilization in this case. The 3D numerical patient model was reconstructed from CT scans by semi-automatic segmentation toolbox ”iSeq” integrated in SEMCAD X. In the Fig. 3.20 (A), the resulting numerical model is shown. Fig. 3.20 (B) shows the placement applicator system around the patient’s neck. Against applicator positions in Fig. 3.20 (B) all applicators are rotated by 40 degrees to show positioning options of heating system. All dielectric and thermal properties of numerical phantoms and parts of waveguide applicator for frequency 434 MHz are listed in Table 3.7.

(A) (B)

Fig. 3.20 Numerical model of real patient with tumor (A) and applicators configuration (B).

Table 3.6 Targets volume summary

Target		Volume [cm^3]
1	Tumor I	12.5
2	Tumor II	16.4
3	Thyroid gland	10.6
4	Tongue	60.6
5	Tumor III	246

Table 3.7 Dielectric and thermal properties used in simulations for frequency 434 MHz [47].

Material	Relative permittivity ε_r [-]	Conductivity σ [S/m]	Specific Heat Capacity [J/kg/K]	Thermal Conductivity [W/m/K]	Heat Generation Rate [W/kg]
Artery	61	1.58	3617	0.51	-
Bone	13.1	0.09	1312	0.32	0.15
Water bolus	81	0	-	0.56	-
Fat	11.6	0.08	2348	0.21	0.51
Muscle	56.9	0.79	3421	0.49	0.96
Skin	40.9	0.89	3390	0.37	1.65
Tumor	59.5	0.89	2654	0.27	1.53
Trachea	43.9	0.8	3568	0.48	0.54
Thyroid gland	61.3	0.97	3421	0.49	87.1
Esophagus	64.8	1.23	3500	0.52	2.94
Vertebrae	13.1	0.09	1312	0.32	0.15
Spinal cord	32.2	0.59	3630	0.51	2.48
Larynx	45.1	0.59	3568	0.48	0.54
Interv. disc	45.1	0.59	3560	0.49	0.54
Vein	61	1.59	3617	0.52	-
Cerebrospinal fluid	70.6	2.25	4095	0.57	-
Connective tissue	47.1	0.56	2372	0.39	0.58
Teeth	13.1	0.09	1255	0.59	-
Nasal cavity	45.71	0.88	3150	0.34	-
Tongue	5.74	0.78	3568	0.49	1.21

3.11.2 Results of Study VI

In Fig. 3.21 and Fig. 3.22, the results gained from numerical simulations are presented. Using these results we investigate applicator system ability to focus the microwave energy to the treated target. This energy is manifested by temperature increasing. In Fig. 3.21, the phantom *SAR* distribution is shown in the first and second columns. The third and fourth columns show us the T_{41} iso-volume contour coverage. In all cases the output power of each applicator was set in order not to exceed the 45 °C temperature maximum in the whole phantom. Fig. 3.21 (A) demonstrates tongue, (B) tumor II, (C) thyroid gland and (D) tumor III, all as for the treated area. For easier comparison, all *SAR* values shown in figures are normalized to total input power 1 W. In the Fig. 3.22 there is a *SAR*-Volume histogram of targets coverage. This figure is obtained from optimized *SAR* simulations and is used to determine the value of SAR_{25}

volume cover. The dashed vertical line indicates the value of 25 % of residual *SAR*. The light blue curve corresponds to *SAR* distribution in the spinal cord (temperature sensitive tissue).

In Table 3.9, target coverage is shown. The best cover results were achieved through Tumor I (SAR_{25} 85 % and T_{41} 95 %), Tumor II (SAR_{25} 80 % and T_{41} 90 %) and thyroid gland (SAR_{25} 87 % and T_{41} 92 %). On the contrary we did not achieve satisfactory *SAR* and temperature tongue cover was SAR_{25} = 21 % and T_{41} = 51 %. The applicator system is effective also for the larger tumor III (SAR_{25} 54 % and T_{41} 80 %). Because the tumor is located on the surface it is possible to use a higher power and cooler water bolus for good T_{41} coverage. In Table 3.8 the applicators settings for each target are listed. For comparison,

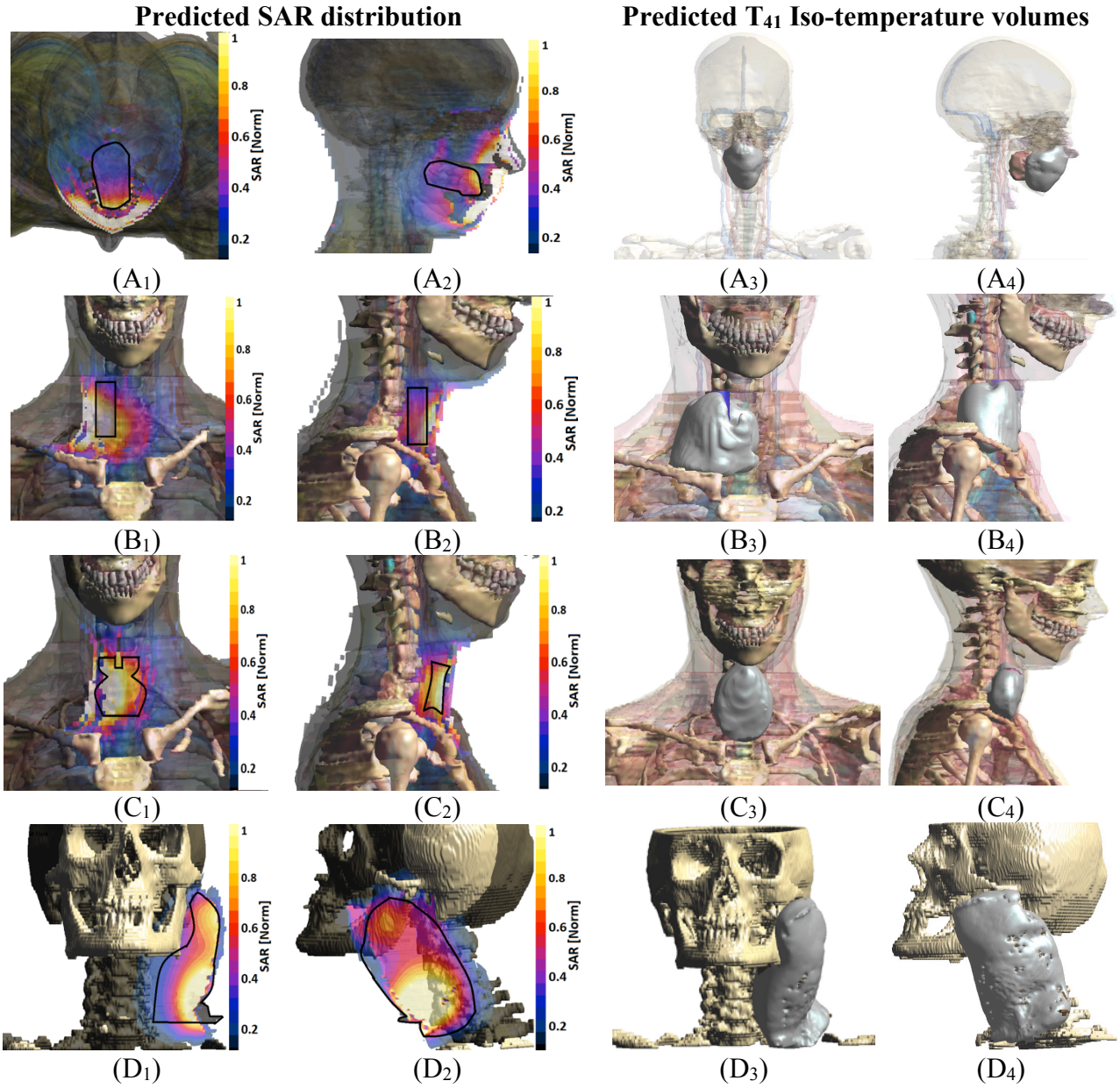

Fig. 3.21 Optimized *SAR* distribution in transversal (index 1), longitudinal cross sections (index 2) and temperature iso-surface T_{41} (index 3 and 4); tongue (A), tumor (A), thyroid gland (C) and real tumor (D).

we added to Table 3.9 SAR_{25} in the non-optimized case. One can see that the values are significantly lower. That means that the optimization increases the power concentration in the treated area.

Table 3.8 Phase (P, degrees) and relative amplitude (A,-) setting for each applicator for all targets

	Target							
Nr. App	**Tumor I**		**Tumor II**		**Thyroid gland**		**Tumor III**	
	A	P	A	P	A	P	A	P
1	0.39	0	0.87	0	1	0	0.41	0
2	1	-56.3	0.93	-38.3	0.83	64.9	1	-69.2
3	0.82	-70.7	1	-0.6	0.88	8.47	0.99	-59.3
4	0.55	-6.5	0.87	-8.7	0.98	42.4	0.64	-67.8

Table 3.9 SAR_{25} and T_{41} iso-contour target volume coverage

Target	***SAR*$_{25}$ [%]**	***T*$_{41}$ [%]**	**No optimized SAR$_{25}$ [%]**
Tumor I	85	95	70
Tumor II	80	90	58
Thyroid gland	87	92	75
Tongue	21	51	6
Tumor III	54	80	36

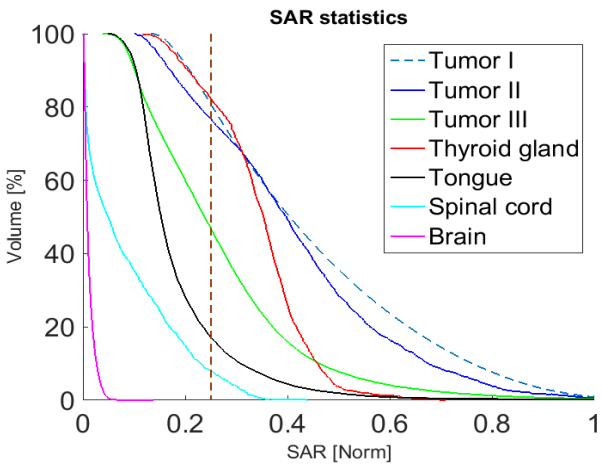

Fig. 3.22 Cumulative optimized *SAR* histogram.

3.11.3 Agar phantom for verification measurement (experiments)

For measuring purposes, a cylindrical homogeneous (160 mm in diameter) phantom with an inserted cylindrical tumor (20 mm in diameter) was made. Phantom ingredients and

their quantities are listed in the following Table 3.10. A completed phantom can be seen in Fig. 3.23.

For determination of complex permittivity of a real agar phantom the method based on reflection coefficient measurement by coaxial probe was used [51]. This method is applicable in a frequency range from 30 MHz to 1 GHz. The results of measurement are listed in Table 3.11.

Table 3.10 Ingredients quantity of healthy and tumorous tissue phantom [94].

Substance	**Healthy tissue [%]**	**Tumorous tissue [%]**
Deionized water	95	66
Agar	4	3
NaCl	0.35	0.5
Food color	0.65	0.5
Ethanol	-	30

Table 3.11 Measured dielectric parameters of heterogeneous phantom for 434 MHz.

Type of tissue	**Relative permittivity ε_r [-]**	**Conductivity σ [S/m]**
Muscle phantom	60.79	0.58
Tumor phantom	52.26	1.01

3.11.4 Laboratory prototype

For the laboratory prototype production we used a special plastic container with required dimensions. The applicators at desired positions were placed at the container wall. The container and applicators were filled by deionized water. The homogenous phantom is placed into the container (see Fig. 3.23 (A) and (B)). For the correct phase and amplitude settings of applicators, the pre-calculated lengths of RF coaxial cables of type RG58 were used (see Table 3.12). Relative permittivity of dielectric material of this type of cable is 2.26 for 434 MHz.

The wavelength of coaxial cable determines the phase shift. The phase shift 2π corresponds to λ_{cable} that is $\sqrt{\varepsilon_{rc}}$ times lower than the vacuum wavelength eq. (3.7).

$$\lambda_{cable} = \frac{c_0}{f \cdot \sqrt{\varepsilon_{rc}}} = \frac{299792458}{434.10^6 \cdot \sqrt{2.26}} = 0.4598 \text{ m} \qquad (3.7)$$

where c_0 is speed of light in vacuum, f is working frequency, ε_{rc} is relative permittivity of coaxial cable. Calculated wavelength in coaxial cable (λ_{cable}) is 45.98 cm.

Table 3.12 Applicator amplitude and phase settings for measurement

Applicator number	Amplitude [-]	Phase [degrees]	Cable Extension [cm]
1	0.39	0	9.03
2	1	-56.3	1.84
3	0.82	-70.7	0
4	0.55	-6.5	8.20

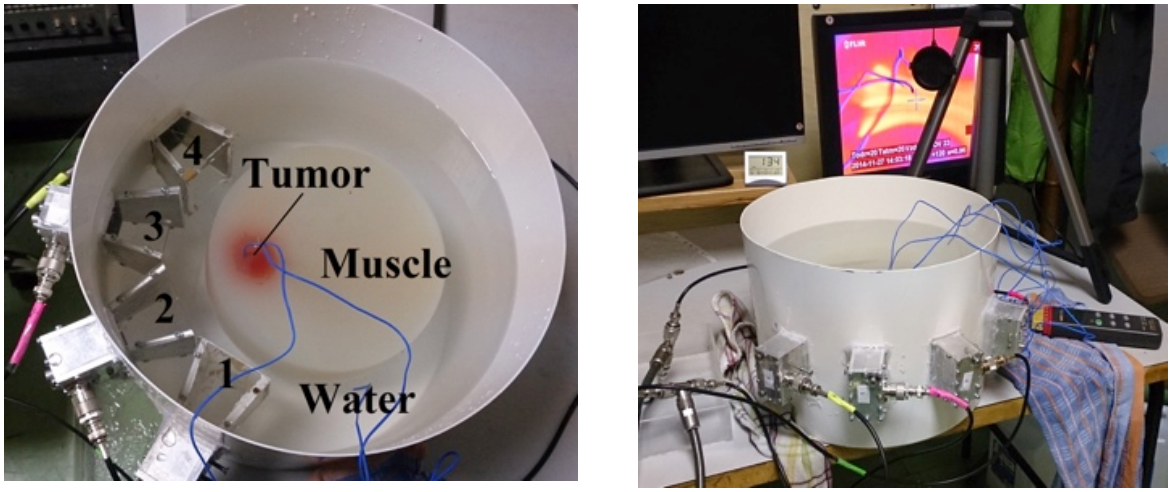

(A) (B)

Fig. 3.23 Photo of the laboratory prototype, top view (A) and measurement setup (B).

a) Experiment 1: Reflection coefficient measurement

In the experiment 1 we evaluated impedance matching of each applicator separately and subsequently of the whole system. The analysis was made by vector analyzer of the Agilent E5062A type in the frequency band from 300 to 600 MHz. In the Fig. 3.24 there are results from this measurement (blue dashed curve) compared to results from numerical simulation (green curve). These curves represent return loss of whole system when all applicators were turned on. The main differences in resonances in curve of reflection coefficient are caused by deviation of phantom dielectric parameters. The matching of the whole system is under -10 dB for 434 MHz and this is satisfactory.

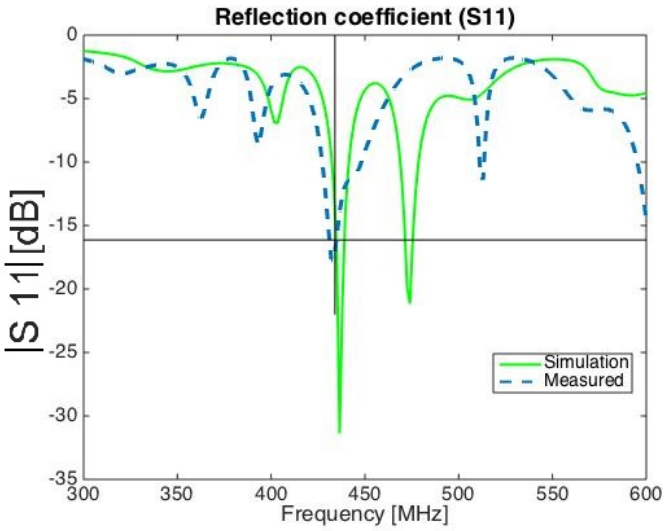

Fig. 3.24 Simulated and measured return loss.

b) Experiment 2: Temperature distribution in homogenous phantom

In this experiment the distribution of absorbed power through temperature in the homogeneous phantom was measured. The main goal of power measurement is to verify energy focusing and heating ability of whole applicator system.

In the Fig. 3.25 the measurement setup with a microwave generator and applicator system is shown. The temperature of the phantom was 22 degrees and the temperature of water bolus (deionized water) was 21 degrees. Waveguide applicators were powered by the generator "UHF-POWER-GENERATOR PG 70.150.2" (it has two separated synchronized power output channels) at frequency 434 MHz and of total power of 150 W for 8 minutes. Applicators 1 and 4 were each excited by 25 W of power (output B), applicators 2 and 3 each with power of 50 W (output A). In the Fig. 3.26 the longitudinal cross section of numerical temperature simulation through homogenous phantom is shown. The simulation settings corresponds to conditions during measurement. Phantom thermograms (Fig. 3.27) show temperature distribution in homogenous phantoms. Energy focus is in the place where the tumor is located (black frame). Thermograms of the phantom were taken by IR camera of the type Flir P25.

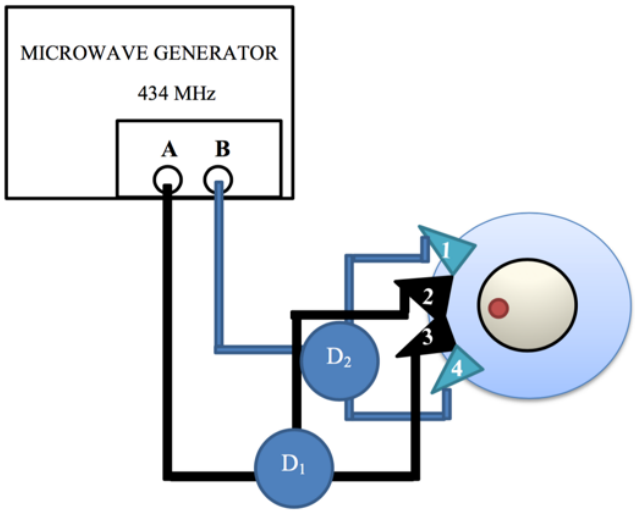

Fig. 3.25 Measurement setup with two power dividers (D_1 and D_2).

3.11.5 Results: Model verification

For verification of results obtained from numerical simulation, we use temperature distribution in a homogenous phantom (simulation results Fig. 3.26). Utilization of parameter SAR_{25} is inaccurate in this case, because the time of exposure was longer (8 minutes). For this occasion the parameter T_{41} was chosen. In the clinical use there is an effort to increase the temperature of tumorous tissue from 37 °C to maximum 45 °C (the temperature difference is 8 °C). In our capabilities it was not possible to have a thermally tempered phantom at 37 °C but only at 22 °C. To keep the same conditions, our maximum temperature in the phantom was 30 °C. A temperature of 26 °C corresponds to 41°C used in simulations. In numerical simulation, 95 % of the whole tumor volume is covered by temperature 26 °C in this case. In the thermogram Fig. 3.27 (B) we calculated the temperature as 26 °C for the volume cover of 88 %. The measurement deviation from the numerical simulation is 7 %.

Generally speaking, temperature increased by 7 - 8 degrees inside the tumor phantom during 8 minutes of heating. This temperature increase is more than sufficient for high quality hyperthermia. Outside the tumor phantom there was a gentle increase in temperature (not greater than 3 degrees).

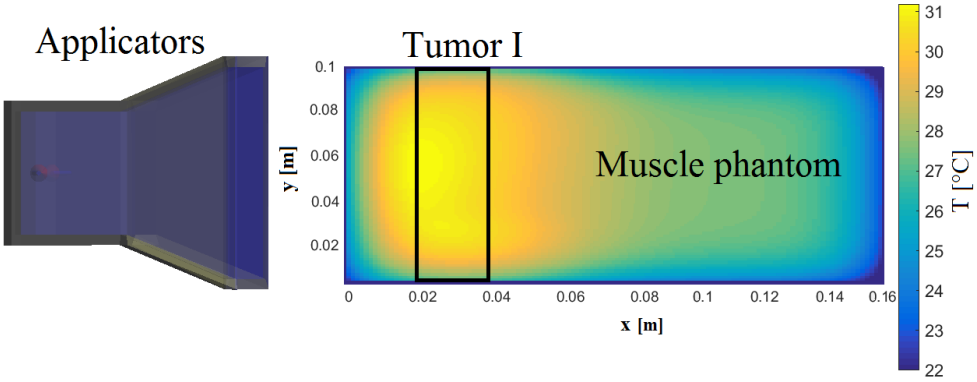

Fig. 3.26 Numerical simulation of temperature distributionin homogenous phantom (cross section).

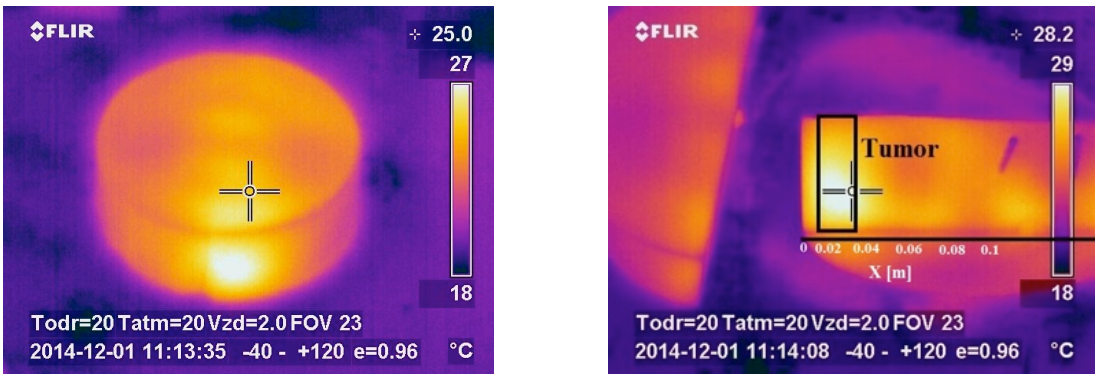

(A) (B)

Fig. 3.27 Thermograms after power deposition, front view (A) and cross section (B).

3.11.6 Conclusion of Study VI

In this study we designed, evaluated and analyzed (numerically and experimentally) a new applicator system intended for focused head and neck hyperthermia therapy. Firstly, according to our previous research, we proposed four waveguide applicator system working on frequency 434 MHz. For evaluation of predicted *SAR* and temperature distribution we defined and used two volume parameters (SAR_{25} and T_{41}). Performance of the new applicator system can be also improved by the treatment planning software based on the Genetic algorithm through the distribution of *SAR* and temperature in the target region. The system is designed with the respect to higher sensitivity of E-field pattern to phases and amplitudes of each applicator feeding. Our simulations proved that the SAR_{25} is approximately by 20 % higher in a treatment target due to optimization. We also observed lower risk of hotspots formation. These benefits permit energy focusing and selectively the tumor heating with the respect to healthy and sensitive tissues.

To compare our system with other methods we made a quantitative comparison with the system of Paulides et al.. In mentioned article [52] the circular system was tested on a numerical 3D human model. The analysis was performed numerically (using 3D model with lympho-node and small tumor) and also by measurement. The targets are relatively similar with our Tumor II (especially in volume and position of the target). Optimized results in [52] show that the lympho-node and tumor SAR_{25} coverage is approximately 85 %. With our presented system we reached the 80 % SAR_{25} coverage for Tumor II. From this comparison it is clear that our system has similar results as other systems.

The originality of our approach is based on the fact that our applicator system uses a limited number of applicators only. This solution, of course, reduces complexity of the whole system, cost of components and it is easier to utilize it in therapy (with lower risk of unwanted hotspots).

A disadvantage of this system, which we recognize, is fixed attachment to patient's body. This is, of course, reducing the patient's comfort. Next problem is the higher energy absorption on the body surface. The main solution helping us to improve temperature distribution and decreasing absorption on patient surface depends on the water bolus temperature. By the water bolus temperature decreasing we were able to supply greater energy to the target without hotspot creating on the body surface. Respecting the penetration depth and the reflection coefficient the ideal water bolus temperature is between 20 – 30 °C.

For experimental results verification the laboratory prototype was constructed. The reflection coefficient of four waveguide applicators and temperature distribution was measured.

4 Chapter: Non-invasive Detection of Temperature Change using UWB Signal

This chapter is based on following published paper:

- O. Fiser, M. Helbig, J. Sachs, S. Ley, I. Merunka and J. Vrba, "Microwave Non-invasive Temperature Monitoring using UWB Radar for Cancer Treatment by Hyperthermia", 2017, review in journal Progress in Electromagnetic Research

4.1 Thermometry in microwave hyperthermia

The premise of safety and successful hyperthermia treatment is the careful treatment planning (using the 3D patient model) and controlled temperature distribution during treatment in the heated area. In cases of hyperthermia treatment, a continuous temperature monitoring is essentially important for patient safety and quality control of whole therapy process. The continuous temperature monitoring represents feedback in achieving and maintaining the required temperature increase in the treated and surrounding areas, within the correct therapeutic range. The temperature information is necessary to be obtained from both the tumor and the surrounding healthy tissues. The thermometry in microwave hyperthermia can be divided into invasive and noninvasive techniques.

4.1.1 Invasive thermometry

The most widely used method of continuous temperature measurement in thermotherapy is still the implementation of invasive probes (e.g. thermocouples or optical catheters) in tumors. Further information can be found in [53]. This method is inexpensive and fast, but it provides information about the temperature from a few singular points only. For more comprehensive information of temperature distribution a high number of catheters are required. But this procedure causes pain and general patient discomfort. The presence of metallic probes (like thermocouples or thermistors used in ALBA system used e.g. at Institute of Radiation Oncology of Bulovka hospital) in the treated area may cause two types of complications [2]. The first complication is that high frequency energy heats the metal and this can result into local temperature extremes and due to good thermal conductivity of the metal the temperature simply spread to the tissue. The second complication is that metal affects the expected electromagnetic field distribution in the tissue. A way to reduce this type of interaction between implants and electromagnetic field is the applicator setting so that the vector of electric field intensity is turned perpendicularly to the metal implant [2]. It is difficult to meet this condition, because in a biological tissue, the vector of electrical field is rotating due to many reflections and transitions between trough types of tissues (hyperthermia applicators are mostly heated in their near field zone). Complications studied with this type of temperature sensors are listed in [55] and [56].

4.1.2 Non-invasive thermometry

In last decade, there is an effort to perform the thermometry as much as noninvasively possible. As more appropriate alternative is the non-invasive temperature monitoring, among which we can consider:

1) Magnetic resonance imaging (MRI)
2) Microwave radiometry
3) Ultrasound based techniques
4) Microwave differential tomography

An overview of possible methods for temperature monitoring for hepatic radiofrequency (RF) ablation brings article [57]. Lars Frich defined the ideal requirements for non-invasive thermometry during the ablation (temperature accuracy: < 1-2 °C, spatial resolution: < 1-2 mm while low cost of the technology being a bonus). These requirements of non-invasive thermometry can also be assigned to the whole thermotherapy treatments. The MRI temperature change detection method is based on measurement of temperature dependent parameters (e.g. shift in proton resonance, diffusion coefficient shift, spin-lattice relaxation time) which are used mainly for MRI imaging [58]. From changes in these signals, the value of temperature change can be determined. Unfortunately, this method is (in comparison with other methods) expensive and requires specific compatible equipment. If the MRI is used for microwave hyperthermia temperature treatment monitoring, the applicators must deal with very strong magnetic fields. Therefore, the whole applicator system must be MRI compatible. This means that applicator must not cause any artifacts in the reconstructed image. The principle of temperature measurement by MRI is listed in [59]. Combination of hyperthermia system with MRI system is an innovation offered by e.g. Pyrexar Company (previously BSD) by system BSD 2000 3D MRI. This system comes with compatible applicator Sigma eye.

The microwave radiometry is based on the principle of the Planck's radiation law, for instance on measurement of noise power radiated from the measured tissue [60]-[62]. The measurement of power on given frequency corresponding to the depth from the temperature is obtained. Radiometers are used in microwave hyperthermia to monitor temperature in frequency range from 27 MHz (approximately 5.5 cm under patient's surface) – 8GHz (approximately 0.3 cm under surface) [60]. In [61] and [62], there are examples of radiometer proposals and applications for temperature measurement.

The third method is ultrasonic (US) temperature measurement based on change of US wave velocity in heated area, and scattering variation of US wave [63], which can be utilized for temperature estimation. The principle of ultrasound temperature change evaluation in hyperthermia treatment is described in [63] and [64].

In literature, we can find relatively new technique based on microwave differential tomography. The microwave tomography is based on the reconstruction of the complex permittivity distribution. Then reconstruction of the temperature profile is possible. The integration of the three-point steering system for the non-invasive temperature monitoring of the high intensity focused ultrasound (HIFU) being based on this method is described in [65] and [66]. The system is composed of the monopole antenna circular array working on the frequency 0.9 and 1.1 GHz. Temperature resolution 0.2 - 0.5 °C (depending on type of the reconstruction algorithm) was achieved. In [67] the system validation of non-invasive temperature observation in small animal (small pigs) was performed. The other real-time microwave imaging system for thermal therapy based on the microwave differential tomography is described in [68] and is based on similar principle.

The methods based on the microwave radar were proposed by Miyakawa et al. (in [69] and [70]). The tomographic method is used for the non-invasive detection of the temperature changes in the human body. The transmitting antenna is emitting a radar chirp signal (1-2 GHz) and the signal is received on the opposite side of the human body. Conventional CT reconstruction algorithms are used for the evaluation and reconstruction of the temperature changes. In [71] the numerical method for a reconstruction of the temperature profile in Time-Domain is described by Bolomey et al.. The temperature profile is estimated through the reconstruction of the conductivity change in case the relative permittivity is equal to one. In the group of microwave temperature imaging can be included also temperature change determination using microwave ultra-wideband (UWB) radar.

The advantage of the UWB radar method for the thermometry against other methods is the assumption that method is less numerically expensive, easy to implement and cost effective. Main part of our research was to study and analyze possibilities of non-invasive thermometry using UWB radar and show the potentiality of this technique in microwave hyperthermia. According to our theoretical assumptions, this radar-based method can be appropriate method for the thermometry.

4.2 Radar in medicine

Microwave radar imaging (together with microwave tomography) belongs to the group of microwave imaging techniques. Microwave imaging is applied to various fields such as industry, army (Ground Penetrating Radar, GPR), civil engineering and for medical or safety purposes (detecting of buried objects, nondestructive material testing) [72]. An increasing interest in the field of medical imaging was developed during last decades. Currently, microwave imaging is a very efficient imaging method, which deserves further development. The basic principle of microwave imaging is that microwaves illuminate the studied object and the reflected and scattered field is recorded by the receiving antennas [72]. The propagating wave in the object of interest is highly scattered and diffracted in various directions. This can lead to unpredictable issues such as formation of evanescent waves [73].

Microwave radar is mainly used in medicine as a method for diagnostics purposes. The transmitting antenna emits short electromagnetic pulse to the medium under test (MUT). When the wave hits into some inhomogeneity (contrast/difference in complex permittivity), three phenomena can occur. Part of the signal is reflected back to the transmitting antenna, part of the signal is scattered into the surrounding area and the rest of the signal energy passes through the second substance where it is received by a receiving one or several antennas. The signal processing method (when we reconstruct the position of contrast in permittivity) is called Synthetic Aperture Radar (*SAR*). In the *SAR* approach, only the information about signal phase shift is used [73]. The most interesting approach of the *SAR* method is the Confocal Microwave Imaging (CMI). The CMI approach is ideal for breast cancer detection and for possible temperature change detection, for example in [74] and [75]. In this method we emit ultra-wideband (UWB) pulse to the tested substance. Only one antenna is in transmitting mode and other antennas are in receiving mode during this time [73]. We obtain reflected signal in the time domain on the receiving antennas. From this signal we can use the time of pulse arrival and its amplitude. Based on this information, and if we know the wave propagation velocity, we can identify the position of the inhomogeneity (scatterer). By illuminating an object from many different directions, we can reconstruct the positions and shapes of volumes of the same permittivity. The resolution of this method is dependent on the used frequency, subsequently on the frequency band of the transmitted pulse and on the wavelength in the tissue in which the wave is propagating.

For image reconstruction from gained signals following algorithms can be used:

- Delay and Sum (DAS) [73]
- Delay-Multiply and Sum (DMAS) [76]
- Improved Delay and Sum (IDAS) [77]
- Robust Capon Beamforming (RCB) [78]
- Multistatic Adaptive Microwave Imaging (MAMI) [79]

The advantage of the radar method is its speed in reconstruction. It is because this method is non-iterative one and the calculations of the scatterer positions are not very difficult from the numerical point of view. The disadvantage of this method is that we get no information about values of dielectric parameters and the quality of reconstruction decreases with lower contrast between displayed substances.

4.2.1 Breast cancer detection

The most common utilization of microwave imaging in medicine is breast tumor detection and subsequently breast imaging. Currently for breast cancer screening, ionizing X-Ray mammography is used. The problem of this method is that is not able to detect 5-15 % of tumors especially in young women. We can classify microwave imaging as a very promising method in breast cancer detection [80]. The microwave breast cancer detection is based on the principle that malignant tissue has a higher permittivity and conductivity than benign or healthy tissue [81]. But in some latest publications (e.g. [82]), where the breast tissues (malignant and healthy) are studied by spectroscopy shows that the contrast between malignant and healthy tissue is not sufficiently detectable from hardware point of view [83]. This problem can be overcome by using nanoparticles, which are injected to the patient's body and are collected in the tumor [83]. This will artificially increase the contrast between permittivity and improve detection of tumors. Advantage of breast tissue in microwave imaging point of view is that breast is composed largely from fat. Fat has a very low conductivity even at higher frequencies. From this point it follows low attenuation impact on propagating wave.

The one of the world leader in microwave breast cancer detection is University of Bristol. The team of Dr. Klemm has developed second generation of multistatic UWB radar-based microwave system containing 60-element hemispherical array working in frequency range 4-10 GHz. In [84] and [85] some experimental laboratory and clinical results are presented.

Very interesting approach was used by team of TU Ilmenau (Germany) for early stage breast cancer detection. The team around Dr. Sachs and Dr. Helbig utilized their M-sequence radar (described in [86]) originally intended for mine finding for breast cancer detection. They used 8 small bow tie antennas with bandwidth 9 GHz in MIMO setup. The system composition is described in [87].

The team from the National University of Ireland Galway around Dr. O'Halloran developed rotating UWB radar for tumor detection using Confocal Microwave imaging (CMI). In [88] the novel rotating system is presented and defining problems arising from the use of rotating system. The team also works on hybrid artifact removal from gained signals and reconstructed images by combination of two artifact removal methods (Entropy-based Time Windowing algorithm and Wiener Filter algorithm) [89].

The method of microwave tomography is using a system developed by Prof. Paul Meaney and his group from Dartmouth University (USA). They were first who developed a clinical prototype for breast cancer detection. The system estimates values and distribution of dielectric parameters in breast. The system utilizes 16 UWB monopole antennas (frequency range 0.5 – 3 GHz) in circular array configuration [90]. This group is already starting with redesigning this system to system for bone imaging.

4.3 Physical principles of differential temperature change detection using UWB signal

The detection principle of temperature changes in the heated area using a UWB radar technology is based on measurement of backscattered signal differences due to the change of the complex permittivity caused by temperature change. The amount of change in complex permittivity can be assigned to the water content in medium under test (MUT) [91]. For example, there is an Ellison model of complex permittivity temperature dependence of pure deionized water [92]. A lot of extensive studies of measured and modelled dielectric parameters of different tissue can be found in literature but it was measured at constant laboratory temperature. Temperature dependent changes in tissue dielectric parameters were measured, modeled and discussed e.g. in Lazebnik's study [91] using pork livers. As far as we know there are no other studies (related to tissues) concerning frequency band of our interest (1-6 GHz).

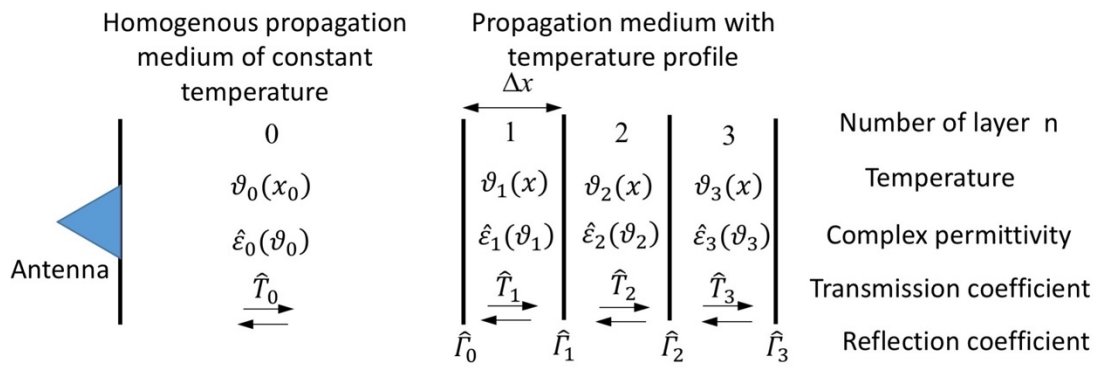

Fig. 4.1 Layered model of locally heated medium under test (MUT).

The layered model of locally heated medium under test (MUT) is shown in the Fig. 4.1. We consider it as a sandwich structure when the thickness of each layer is very small (infinitely). Each slice is homogenous of specific complex permittivity (temperature). We derived equation of the relationship between phasor of received and transmitted signal intensity respecting continual reflection along the phantom. The temperature changes in time and volume as well as complex permittivity $\hat{\varepsilon}$ (and thus wave impedance $\hat{Z}$, where ˆ symbolizes complex number), see Fig. 4.1. Let's suppose signal is reflected by one borderline at distance *x:*

$$\hat{I}_R = \hat{I}_T \, \mathrm{e}^{-2\hat{\gamma}x} \hat{\Gamma}(x) \qquad (4.1)$$

where $\hat{I}_R$ is the received signal intensity,

$\hat{I}_T$ is the transmitted signal intensity,

x is distance from antennas to the point of reflection,

$\hat{\Gamma}$ is the reflection coefficient and $\hat{\gamma}$ is the propagation constant representing propagation speed and losses.

The propagation constant $\hat{\gamma}$ is expressed as:

$$\hat{\gamma} = \frac{2\pi f}{c_0} \sqrt{\frac{\hat{\varepsilon}}{\varepsilon_0}} \qquad (4.2)$$

where c_0 is speed of light in vacuum.

If the temperature in the medium is changing with distance *x* continuously, then the continuous borderlines reflecting the signal rise. The "continuous" reflection can be principally expressed by the integration of eq. (4.1):

$$\hat{I}_R = \hat{I}_T \int_0^L e^{-2\int_0^x \hat{\gamma}_0(f)dx} \hat{\Gamma}(x)dx \tag{4.3}$$

where L is the total length of the phantom.

This equation is based on assumptions that the propagation constant $\hat{\gamma}$ is equal to $\hat{\gamma}_0$ (constant along x) from the attenuation point of view (not from the reflection coefficient viewpoint). The reflection coefficient is very small and thus we can consider the unity transmission coefficient. Reflection coefficient $\hat{\Gamma}$ of a layer boundary (μ is supposed to be constant and equal to μ_0):

$$\hat{\Gamma} = \frac{\hat{Z}_{n+1} - \hat{Z}_n}{\hat{Z}_{n+1} + \hat{Z}_n} = \frac{\sqrt{\hat{\varepsilon}_n} - \sqrt{\hat{\varepsilon}_{n+1}}}{\sqrt{\hat{\varepsilon}_n} + \sqrt{\hat{\varepsilon}_{n+1}}} = \frac{\hat{\gamma}_n - \hat{\gamma}_{n+1}}{\hat{\gamma}_n + \hat{\gamma}_{n+1}} \approx -\frac{\Delta\hat{\gamma}_n}{2\hat{\gamma}_n} \tag{4.4}$$

considering $\Delta\hat{\gamma}_n = \hat{\gamma}_{n+1} - \hat{\gamma}_n$ and $|\Delta\hat{\gamma}_n| \ll 2\hat{\gamma}_n$. Substituting it to the eq. (4.3) one can obtain:

$$\hat{I}_R = -\hat{I}_T \int_0^L \mathrm{e}^{-2\int_0^x \hat{\gamma}_0(f)dx} \frac{\Delta\hat{\gamma}_n}{2\hat{\gamma}_n} dx \tag{4.5}$$

where $\hat{\gamma}_0$ is the propagation constant of medium at initial temperature, f is frequency. We assume a weak spatial variation of the propagation constant. We can write then $\hat{\gamma}_n \approx \hat{\gamma}_0$. For small Δx ->0 it is valid:

$$\Delta\hat{\gamma}_n = \gamma' \Delta x \tag{4.6}$$

Derivation of the propagation constant γ'owing to distance x depends on temperature. And this temperature is dependent on distance x from antenna to the point of investigation. It can be expressed as:

$$\gamma'(x, f, \vartheta) = \frac{d\hat{\gamma}(f)}{d\vartheta}\frac{d\vartheta(x)}{dx} = \hat{\alpha}_\gamma(f)\vartheta'(x) \tag{4.7}$$

where $\hat{\alpha}_\gamma(f)$ is the temperature coefficient of the propagation constant and $\vartheta'(x)$ is representing the temperature change which we are interested in. Finally, we can obtain:

$$\hat{I}_R \approx -\hat{I}_T \frac{\hat{\alpha}(f)\Delta x}{2\hat{\gamma}_0(f)} \int_0^L \mathrm{e}^{-2\int_0^x \hat{\gamma}_0(f)dx} \vartheta'(x)dx \tag{4.8}$$

From eq. (4.8), we can observe that the reflection coefficient of the propagation medium at a given frequency depends on the temperature gradient. Hence, by measuring the reflection coefficient over a large bandwidth, an appropriate inversion of eq. (4.8) may be used to reconstruct the temperature gradient.

For the case of a radar measurement, the received signal in time domain follows eq. (4.7) as:

$$y(\tau) = h_r(t) * i_R(t) * h_t(t) * a(t) \quad (4.9)$$

Here, * represents convolution, h_r and h_t are the impulse responses of the antennas in the receive and transmit mode, $a\ (t)$ is the stimulus signal and t is the propagation time. The impulse response of the propagation medium is assigned as $i_R(t)$, which is nothing but the inverse Fourier transform of eq. (4.8). Note, however, that our simple plane wave model does not respect spherical wave propagation and the permeability μ of the propagation medium is supposed to be constant.

In what follows, we are mainly interested in the observation of the temporal temperature variation due to heating. For that purpose, we start the measurement at temperature equilibrium leading to the receiving signal $y_0(t)$ which is taken as reference. This signal is subtracted from the signal measured during heating. Since antenna impulse responses and sounding signal does not depend on the temperature, their actual time shape is out of interest.

4.4 Temperature dependence of used phantoms

For our analytical, numerical and feasibility studies two types of phantom were used:

1) Oil-gelatin phantoms

For the temperature experiments the mimicking oil-gelatin phantoms according to Lazebnik et al. [23] were used. These phantoms are mainly intended for microwave imaging purposes. Their dielectric parameters can be changed by the varying of the oil-content in the mixture. We considered suitable phantom of different oil-gelatin content in respect to the melting temperature. We figured out that the melting temperature decreases for phantoms of a higher oil content. The only applicable phantom for our purposes was the phantom without any oil content whose melting temperature was 35 °C, which seems to be sufficient for our purpose. Dielectric parameters of the used phantom are corresponding to the tumorous tissue (ε_r = 68 and σ = 2 S·m^{-1} for 3 GHz [93]). For the oil-gelatin phantom the temperature dependence of complex permittivity was not estimated or measured.

2) Agar phantom

For numerical studies and feasibility measurements a natural gelatin (agar) phantom (which is the testing standard for the microwave hyperthermia applicators at frequencies of 434, 915 and 2450 MHz) was used. Parameters of gelatin phantom were measured and described in [94]. The advantage of this type of phantom is its thermal stability up to the temperature 80 °C. This phantom is representing tissues with high water content and the expected change of complex permittivity with temperature will be higher than in phantoms

representing tissues with lower water content. To estimate the agar phantom temperature dependency of complex permittivity we proposed and realized following procedure. Firstly, we measured the frequency dependence of the complex permittivity of an agar phantom at 20 °C using available probe "Dielectric Assessment Kit" (DAK-12) from the Speag company working in the frequency band 10 MHz – 3 GHz (measured at the Faculty of Biomedical Engineering, CTU Prague, Czech Republic). We fitted the measured data into a "two pole" Cole-Cole model according to the Cole-Cole expression eq. (4.10) using the MATLAB non-linear regression tool to extend the frequency band:

$$\varepsilon'(\omega) - \mathrm{j}\varepsilon''(\omega) = \varepsilon_\infty + \sum_{\mathrm{k}=1}^{\mathrm{N}} \frac{\Delta\varepsilon_k}{1 + (\mathrm{j}\omega\tau_\mathrm{k})^{(1-\zeta_k)}} + \frac{\sigma_i}{\mathrm{j}\omega\varepsilon_0} \qquad (4.10)$$

where ε' is real part of complex permittivity, ε'' is imaginary part of complex permittivity, N is the order of the Cole-Cole model (in our case N=2), ε_∞ is the permittivity at infinite frequency, $\Delta\varepsilon_k$ is the dispersion magnitude described as $\Delta\varepsilon_k=\varepsilon_s-\varepsilon_\infty$ (ε_s is the static permittivity), τ_k is the relaxation time constant, ζ_k is the pole broadening parameter fixed permanently to 0.1 and σ_i is the static ionic conductivity. The complex permittivity dependence on temperature was determined using the Ellison model of complex permittivity of pure water (gelatine phantom consists of 96 % of water) [92]. Therefore, we assume that the temperature and frequency dependence of agar phantom and water is proportional for both ε_r and σ case. To estimate the temperature dependence of dielectric parameters we proposed following approximate eq. (4.11) and (4.12):

$$\varepsilon_r(\mathrm{agar}, f, \vartheta) \approx \varepsilon_r(\mathrm{agar}, f, \vartheta_0) \cdot \frac{\varepsilon_r(\mathrm{water}, f, \vartheta)}{\varepsilon_r(\mathrm{water}, f, \vartheta_0)} \qquad (4.11)$$

where f is frequency, ϑ_0 is the temperature at the time of measurement (20 °C) and ϑ is the temperature for which we want to calculate the parameter estimation. The same idea we applied to the specific conductivity too.

$$\sigma(\mathrm{agar}, f, \vartheta) \approx \sigma(\mathrm{agar}, f, \vartheta_0) \cdot \frac{\sigma(\mathrm{water}, f, \vartheta)}{\sigma(\mathrm{water}, f, \vartheta_0)} \qquad (4.12)$$

In Fig. 4.2 the estimated course of the relative permittivity (A) and the specific conductivity (B) depending on frequency and temperature in the temperature range 20-45 °C are shown. The blue curve is the modelled course from measurement while other curves are estimated by suggested temperature dependence (derived from eq. (4.11) and (4.12)). The relative permittivity change is approximately 2 % per 5 °C. Values of specific

conductivity are changing approximately by 14 % per 5 °C (for temperature range 20-30 °C).

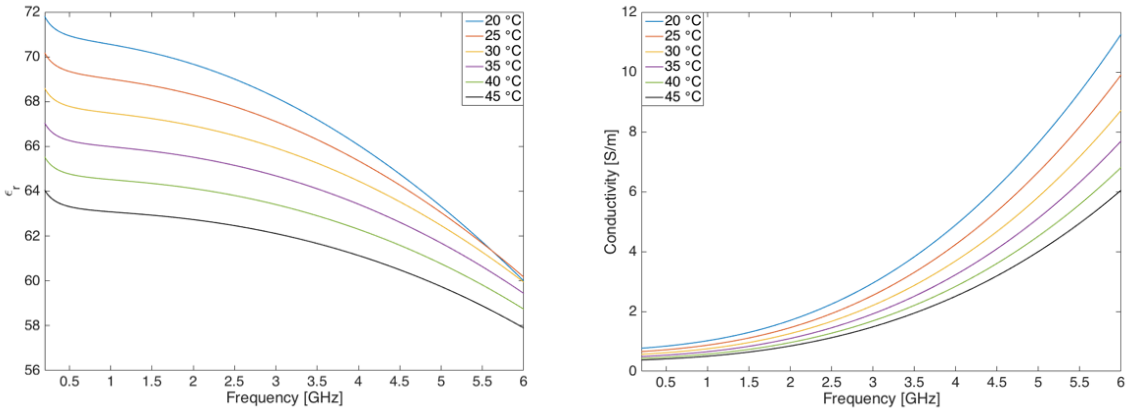

(A) (B)

Fig. 4.2 Estimation of temperature dependency of real part relative permittivity (A) and imaginary part of relative permittivity (B) of agar phantom using equation (4.11) or (4.12).

4.4.1 Measurement of temperature dependency of complex permittivity (of water and agar phantom) and its estimation verification

The main purpose of this chapter is to verify our estimated data (presented in the Fig. 4.2) of the temperature dependency of complex permittivity in the frequency band of our interest (1-6 GHz) which were used in simulations. For the measurement purposes the Agilent 85070E Dielectric Probe Kit containing the coaxial probe was used. This type of Dielectric Probe Kit is intended for the frequency band 200 MHz – 50 GHz. The coaxial probe was connected to the UWB M-sequence sensor system working in the frequency band from 200 MHz – 7.5 GHz. For the data conversion from the measured data to the complex permittivity the ultraANALYSER software developed at TU Ilmenau (Germany) was used.

Firstly, we measured data of the complex permittivity temperature dependency of distilled water from 16 – 32 °C. This relatively narrow temperature band was chosen to reduce the inaccuracies of measurement. According to our experience the measurement of temperature dependency is complicated and the uncertainties are mainly caused by temperature gradient between probe and MUT. We registered two following problems:

1) The measurement calibration was done at different temperatures, the probe is heated because of the temperature gradient (between MUT and probe temperature). This is causing probe prolonging (due to steel expansion) and thus the measuring plane is shifted.

2) In case of measured heated solid materials, the probe is also partially cooling down the MUT in which the temperature gradient is created (in case of liquids this problem is not causing uncertainties due to the liquids flow and mixing).

The Fig. 4.3 (A) and (B) are showing the measurement setup containing water bath with circulating heated water of required temperature. In case of measuring solid phantoms two samples are inserted to the water bath (Fig. 4.3 (A)). The first phantom sample is the control sample with two inserted temperature probes (one in the center and second on the edge). To obtain homogenous temperature distribution in the phantom the measurement was carried out when the difference between temperatures gained from probes was below 0.2 °C. To maintain the properties the agar phantom was inserted in plastic bag (visible in the Fig. 4.3 (B)). All measurements were done after at least two hours of heating up the measurement system to minimalize the drift effects.

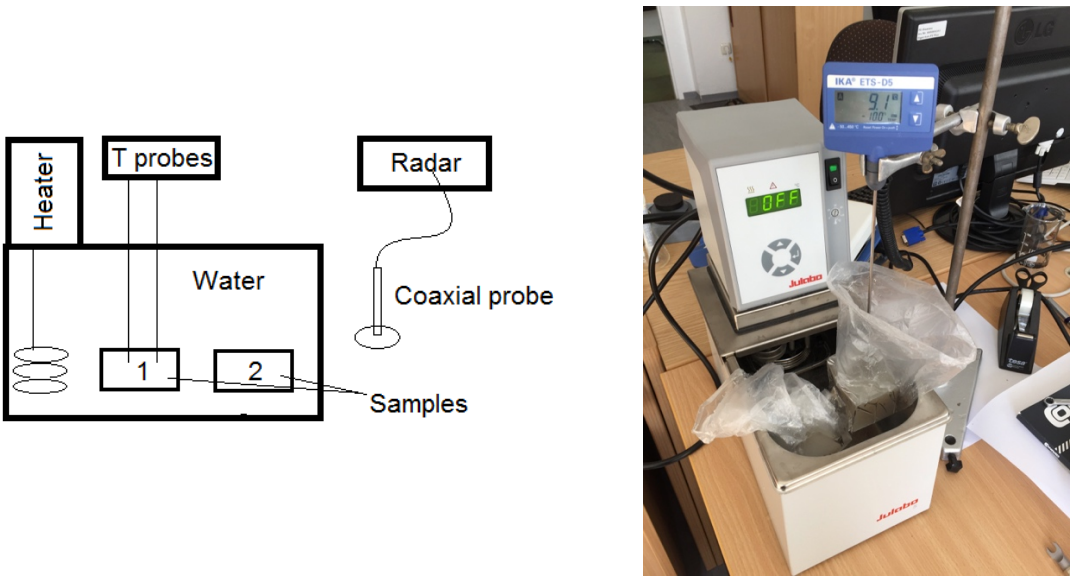

(A) (B)

Fig. 4.3 Measurement setup for temperature dependency measurement of complex permittivity of agar phantom (A) and photo of actual measurement (B).

Firstly, we did the comparison of the Ellison model from the literature and our measurement of distilled water. We heated up the distilled water and after obtaining required temperature we proceed 5 measurements in the row for statistical purposes. In the two following graphs the results (mean values gained from 5 independent measurements) from measurement of complex permittivity temperature dependency of distilled water in the frequency band 1-7 GHz and in temperature range from 16 °C to 32 °C are presented. In the Fig. 4.4 data between used model from Ellison [92] (dashed line) and our measured data in required frequency band are compared. The RMSE (in percentage) of the relative

permittivity and specific conductivity is below 1 %. This can be caused by the difference and deviation of parameters of measured distilled water. The correlation between model and measured curves was very high (over 98 percent) in both (relative permittivity and specific conductivity) cases.

The second validation experiment was done using the agar phantom. We used the measurement setup as you can see in the Fig. 4.3 (A) and (B). Because the homogenous heating of whole phantom is very time lengthy we measured the complex permittivity only for two temperatures (23.8 and 32.8 °C). The heating up procedure between the temperature each temperature state took over 30 minutes. Although the measurement system was heated up (over two hours) there were also slight drift effects influencing the measurement. To minimalize these effects before each measurement the distilled water of constant temperature was performed and the deviation was subtracted from the result of the agar phantom. In the Fig. 4.5 results of the agar phantom are presented. The RMSE [%] of the relative permittivity between measured data and model was approximately 1.5 %. This error could be caused by the uncertainty in the phantom preparation or by the measurement procedure. Fortunately, the differences between the curves of each temperature (estimated (23.8 °C) vs. estimated (32.8 °C), measured (23.8 °C) vs. measured (32.8 °C)) are very similar. This allows us to use the estimations of dependence of relative permittivity and conductivity on temperature. The correlation coefficient is around 98 %. This validation is limited in number of measured temperatures but still can serve as a model confirmation which was presented in the previous section. This complex permittivity model is used in the following numerical models.

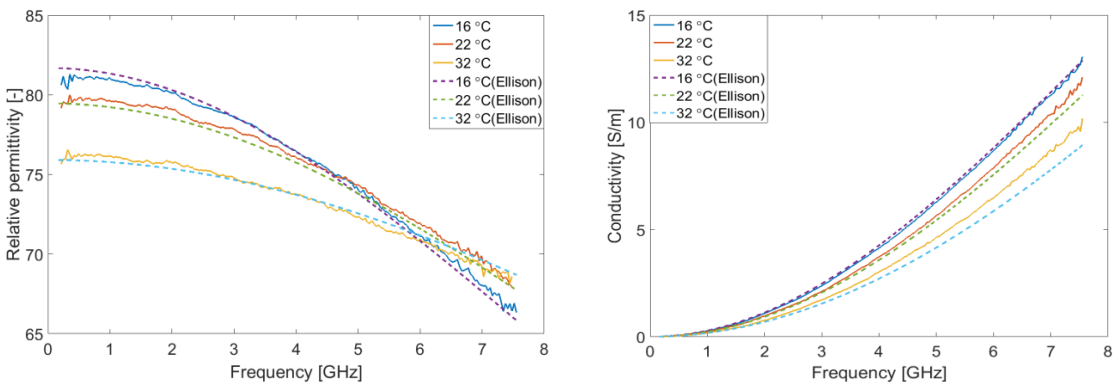

(A) (B)

Fig. 4.4 Comparison of measured temperature and frequency dependency of distilled water with the model from Ellison, (A) relative permittivity and (B) specific conductivity.

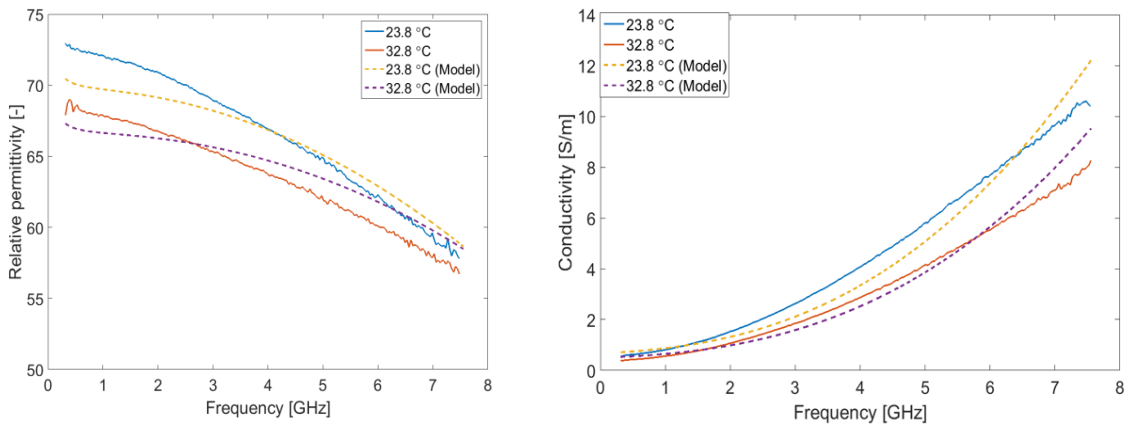

(A) (B)

Fig. 4.5 Comparison of estimated and measured temperature dependency of relative permittivity (A) and specific conductivity (B) of the agar phantom.

4.5Numerical solution in 1D

We derived a simplified Mason graph of layered medium based on the structure in the Fig. 4.6. This model has one dimension and was implemented to the MATLAB software to help us to understand the relation between reflected signal and change in temperature.

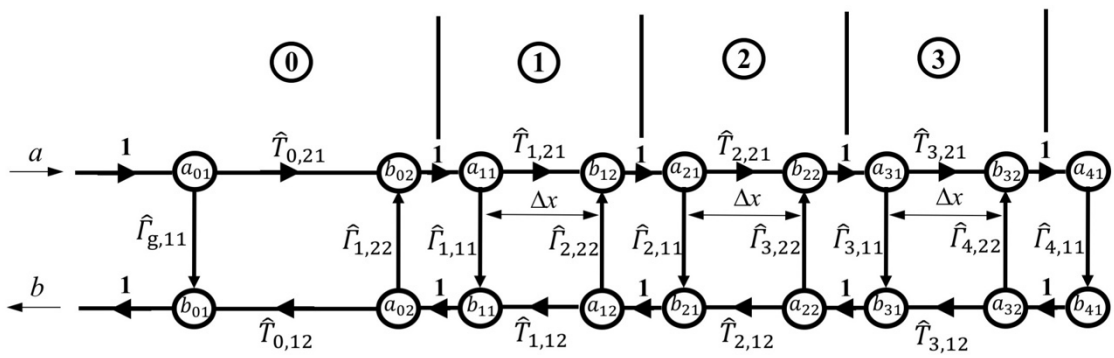

Fig. 4.6 Mason graph of the locally heated MUT with three layers (sandwich structure) corresponding to Fig. 4.1.

The response of the structure of *N*-layers is calculated in frequency domain according to the following formula. Once the response is calculated, the Inverse Fast Fourier Transform (IFFT) is used for transformation the response to the time domain. From the Mason graph (Fig. 4.6) we present, for instance, an equation that respects the reflection and one reflection of the reflected signal. The relation is expressed in eq. (4.13) for 3 layers according to the Fig. 4.6.

$$b = a(\hat{T}_{0,21}\hat{T}_{0,12}\,\hat{\Gamma}_{1,11} + \hat{T}_{0,21}\hat{T}_{0,12}\,\hat{T}_{1,21}\hat{T}_{1,12}\hat{\Gamma}_{2,11} + k_1 + \hat{T}_{0,21}\hat{T}_{0,12}\,\hat{T}_{1,21}\hat{T}_{1,12}\hat{T}_{2,21}\hat{T}_{2,12}\hat{\Gamma}_{3,11} + k_2 + \cdots) \quad (4.13)$$

where b is the response of the structure, a is the transmitting signal and $k_{1,2}$ are double reflections coefficients which can be expressed after the following formulas:

$$k_1 = \hat{T}_{0,21}\hat{T}_{0,12}\hat{T}_{1,21}^2\hat{T}_{1,12}^2\hat{\Gamma}_{1,11}^2\hat{\Gamma}_{1,22} \quad (4.14)$$

$$k_2 = \hat{T}_{0,21}\hat{T}_{0,12}\hat{T}_{1,21}\hat{T}_{1,12}\hat{T}_{2,21}^2\hat{T}_{2,21}^2\hat{\Gamma}_{3,22}^2\hat{\Gamma}_{2,22} \quad (4.15)$$

According to the results of our study, the twice reflected signal in case of real temperature distribution is approximately 2500 times lower than once reflected signal. Therefore it can be neglected in the simulations. This simplification can be used only in case, when the reflection coefficients are quite small.

4.5.1 Numerical 1D studies

For our simulation study of the signal behavior, a simple model of 1D structure with only two layers (of different temperature of one transition) was modelled. The frequency band was set from 1 to 6 GHz of amplitude of 1(for each frequency). The two following cases were studied:

1) 1D1. Calculation of the reflection dependent on the changing distance between antenna and the impedance jump (from 1-7 cm). The temperature gradient between layers was set to 1 °C (temperature of 1st layer was 37 °C and 2nd layer temperature was set to 38 °C). The simulation setup is presented in the following Fig. 4.7.

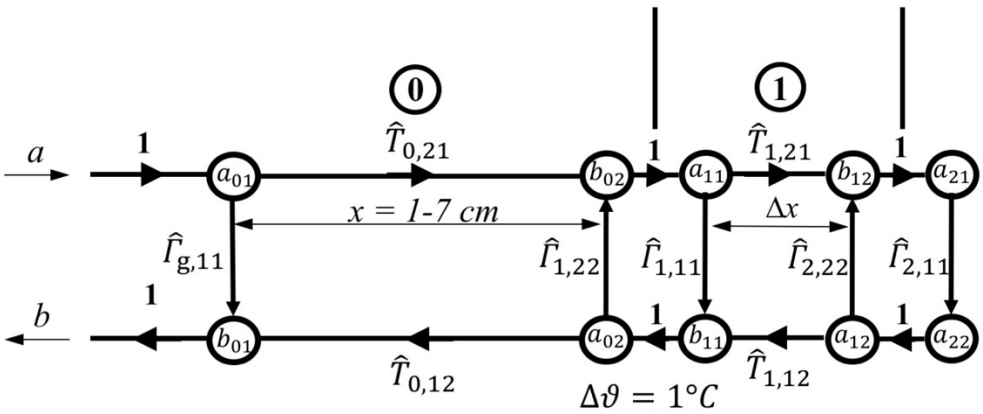

Fig. 4.7 The simulation setup for the frequency response of the 1 °C difference between layers in case of changing of distance between antenna and the second layer.

2) 1D2. The aim of the second study was to determine the expected relation between the reflected signal intensity and the temperature change. For this study, two layers were modelled. The temperature difference between first and second layer was changing from 0.05 – 0.3 °C of the step 0.05 °C. The distance between antenna and the beginning of the second layer was permanently set to 4 cm (see Fig. 4.8).

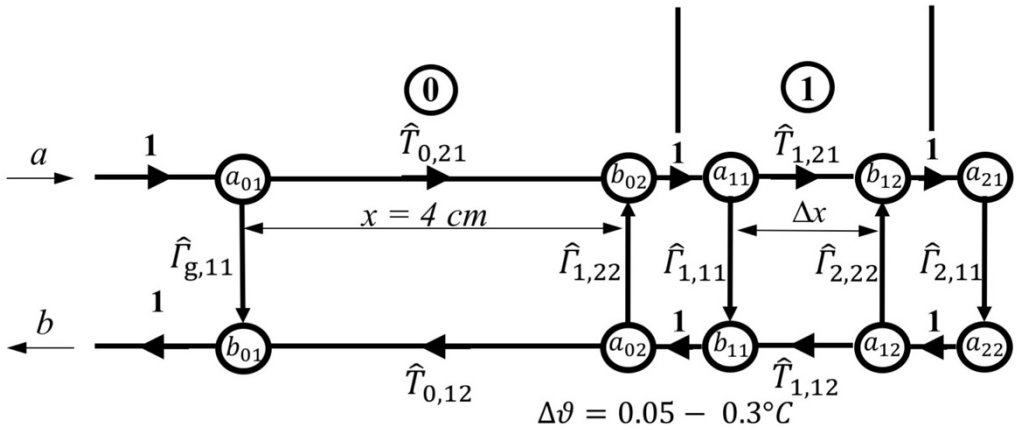

Fig. 4.8 The simulation setup for signal response of different temperature contrasts with constant distance between antenna and the second layer.

4.5.2 Results of numerical 1D study (1D1)

In the Fig. 4.9 ((A) and (B)) shows the results of the 1D numerical study of the signal amplitude dependency on the distance between antennas and the heated part (which is represented by the second layer). According to the theoretical assumptions the higher frequencies are more attenuated than the lower frequencies. Please note that the signal wave propagated the distance two times (i.e. for the distance 7 cm the propagated wave together 14 cm totally). With the increasing distance between antennas and the second layer the frequency bandwidth usable for our purposes is obviously decreasing as expected. For the distance 1 cm the whole bandwidth (1-6 GHz) is applicable while the amplitude difference between 1 GHz and 6 GHz was only -2 dB. When the distance was set to 7 cm, the difference between the lowest frequency and the highest one was much greater (-16 dB). We decided to set the -3 dB decrease of 1 GHz signal level as a usable frequency bandwidth for each distance. In the Table 4.1 the frequency bands for each distance gained from the Fig. 4.9 (B) are listed.

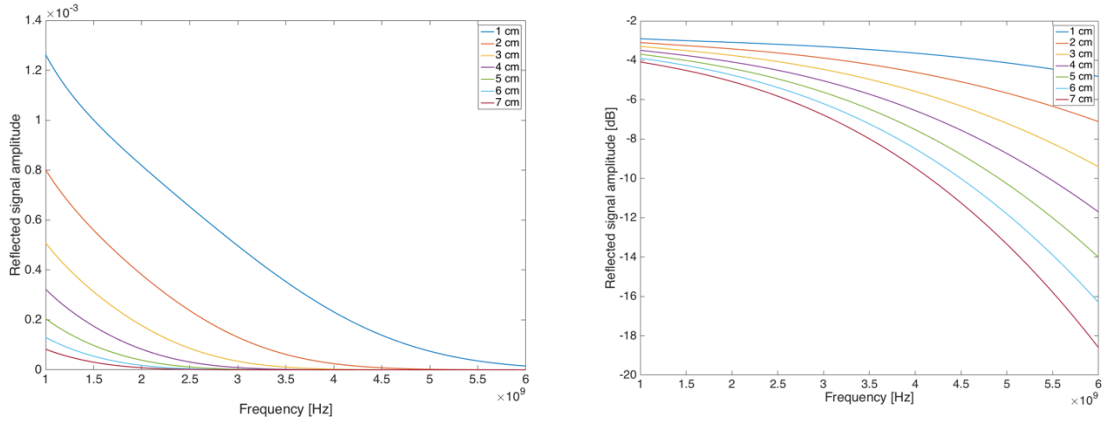

(A) (B)

Fig. 4.9 Results of reflected signal amplitude dependency on the distance from antennas in case of fixed temperature difference of 1 °C. (A) in linear scale and (B) in logarithmic scale.

Table 4.1 Overview of the usable bandwidth for the variable distances between source and second layer (contrast in temperature).

Distance [cm]	**1**	**2**	**3**	**4**	**5**	**6**	**7**
Att. 1 GHz [dB]	- 2.8	- 3.1	- 3.3	- 3.5	- 3.7	- 3.9	- 4.1
Max. frequency (-3dB) [GHz]	6	5.26	4.51	4	3.65	3.35	3.18

4.5.3 Results of numerical study (1D2)

The results of the second study are presented in the Fig. 4.10 (A) – in linear scale and (B) – in logarithmic scale. The graph is showing the reflected signal amplitude from the distance of 4 cm from antenna. In that point the temperature difference between two layers was changing. The dependency between reflected signal intensity and temperature difference is plotted in the Fig. 4.10. It is visible that the reflected signal intensity is changing linearly with the temperature jump for each frequency. In our following measurement studies the linear behavior of the reflected signal dependent on temperature change was expected.

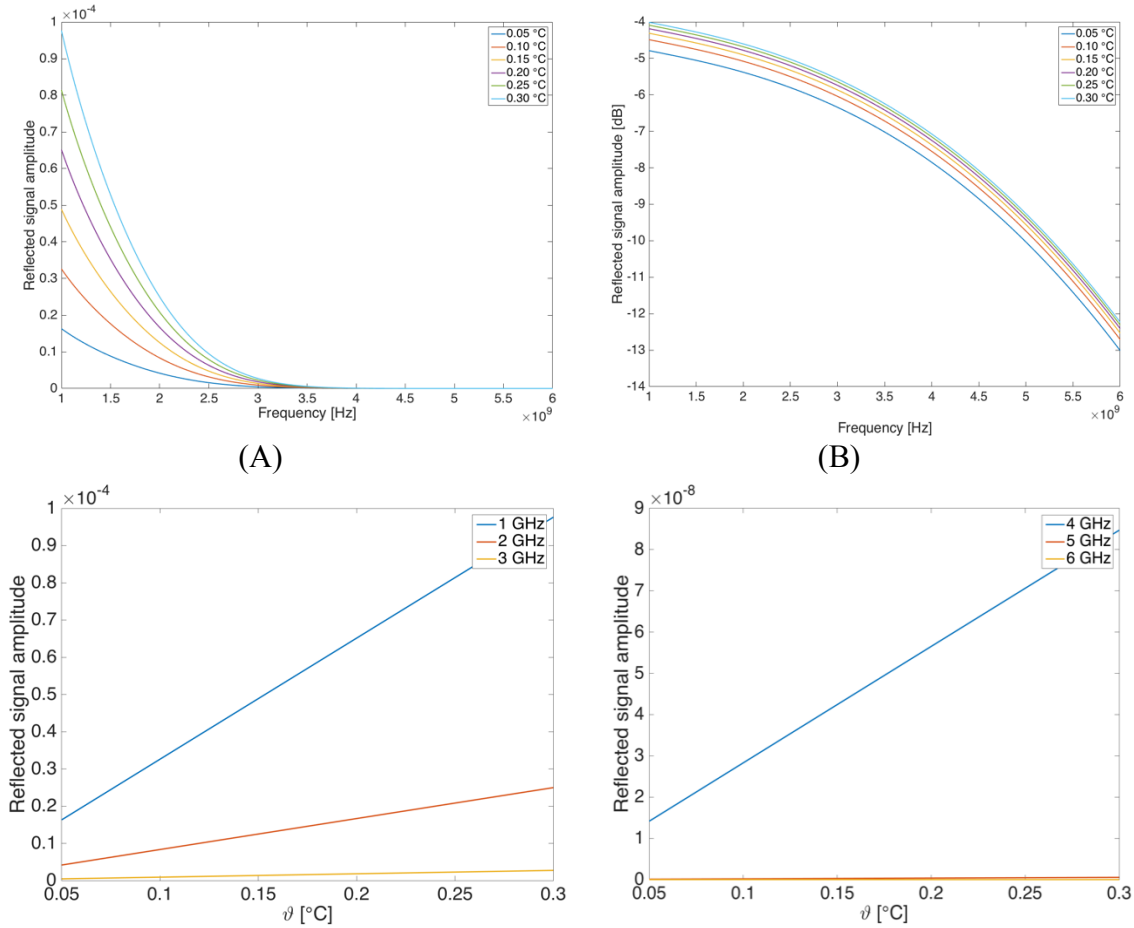

Fig. 4.10 Reflected signal amplitude dependency on the temperature difference between layers for whole frequency spectrum (A), (B) and for selected frequencies with linear behavior (C) and (D).

5 Chapter: Feasibility Study of Temperature Change Detection using UWB Radar System

This chapter is based on following published papers:

- O. Fiser, M. Helbig, S. Ley, J. Sachs, and J. Vrba, “Feasibility study of temperature change detection in phantom using M-sequence radar”, in 2016 10th European Conference on Antennas and Propagation (EuCAP), 2016, pp. 1–4.
- O. Fiser, M. Helbig, J. Sachs, S. Ley, I. Merunka and J. Vrba, “Microwave Non-invasive Temperature Monitoring using UWB Radar for Cancer Treatment by Hyperthermia“, 2017, review in journal Progress in Electromagnetic Research.

5.1 Introduction

This part of the doctoral thesis is mainly considered as an extended feasibility study. In this chapter, we would like to describe the experiments which were carried out to study the signal behavior in dependence on the local temperature change in the MUT.

5.2 Radar device

Our measurements were based on M-sequence radar technology developed at the Technische Universität Ilmenau in Germany. The energy of the pseudo-noise stimulus is distributed equally over time, while the stimulus signal is very time stable and robust, with low jitter and drift. This enables emission of relatively low signal magnitudes and it makes the device suitable for medical purposes. The time response was computed through a cross-correlation between the stimulus signal and the measured signal from medium under test (MUT). 80 % of signal power is located in the region from the direct current (DC) and half clock [95]. The used M-sequence technology we used is further described in [95].

5.3 Signal processing

To analyse the received signals and to obtain the response caused by local temperature increase or decrease, we had to deal with specific strong effects affecting the signal of our interest. These interrupting effects must be carefully removed from the signals (without influencing the signal of interest). For these reasons, we performed the following steps:

1) clutter suppression
2) drift elimination
3) losses correction

These procedures are described in [96] and [97] in detail. For simplicity we did not anticipate the frequency-dependent tissue losses. Differential signal $y_d\ (t,\tau)$ (difference caused by heating effects) is expressed from next equation:

$$y_d\ (t,\tau) = y_H(t,\tau) - \bar{y}_0(t) \qquad (5.1)$$

where t is the propagation time, τ is the observation time, $y_d\ (t,\tau)$ is the signal difference caused by heating effects, $y_H\ (t,\tau)$ is signal at a certain time of heating, $\bar{y}_0\ (t)$ is the mean signal value computed from gained signals before heating (template). In all our further described measurements, the mean signal value was determined when the phantom was stabilized at temperature of 20 °C.

5.3.1 Drift and clutter

The first phenomena influencing signal are drift effects caused by small temperature changes of radar and of active antennas. This phenomenon is noticeable in case of long time measurements (our case). For effective drift correction (gain and time) we used a procedure proposed in [97].

Furthermore, the signal is overlapped by antenna crosstalk and the main reflections from heating system (background). Under the condition that the clutter (e.g. antenna crosstalk and other undesired reflection) is constant through the whole measurement and the signal in which we are interested in is differential, the clutter removal can be realized by a simple background subtraction.

5.3.2 Attenuation correction

The electromagnetic wave is attenuated due to the relatively high phantom conductivity ($\sigma_{phantom}$ = 2.2 [S·m^{-1}] for the frequency of 3 GHz). In case when we know the permittivity and conductivity of the phantom, we can estimate the correction of the signal amplitude depending on time of arrival. Thanks to this correction of signal amplitude, we are able to compare reflection intensities independently of the depth inside the phantom. Magnitude of electromagnetic wave intensity decreasing due to attenuation in loss material is described by following eq. (5.2):

$$\widehat{\boldsymbol{E}}(x) = \widehat{\boldsymbol{E}}_{\boldsymbol{0}} e^{-\alpha(x)\cdot x} \qquad (5.2)$$

where $\widehat{\boldsymbol{E}}$ is intensity of electric field [V·m^{-1}], $\boldsymbol{E_0}$ is the maximum intensity of electrical field at the surface (beginning of the loss material), x is distance from antenna [m] and α is an specific attenuation coefficient [m^{-1}] expressed by eq. (5.3).

$$\alpha = \omega \sqrt{\frac{\mu\varepsilon}{2}\left[\sqrt{1+\left(\frac{\varepsilon''}{\varepsilon'}\right)^2} - 1\right]} \qquad (5.3)$$

where ω is an angular frequency [rad·s^{-1}], μ is the permeability [H·m^{-1}], ε is the permittivity [F·m^{-1}], ε' (ε'') is real (imaginary) part of complex permittivity of phantom.

5.4 Feasibility experiments

The main goal of proposed experiments is to investigate the influence of temperature changes in the phantom on the radar signal. These reflection variations are caused by very small permittivity changes visible in the Fig. 4.2. We proposed and performed differential

measurements with and without heating to detect the changes in signal caused by temperature increase or decrease. From the knowledge of phantom dielectric parameters in the applied frequency band, we were able to estimate the average wave velocity in phantom and assign the reflections in signal corresponding to the distance from antennas.

5.4.1 Antennas

For our measurements, we have considered among three types of antenna to find an appropriate one for the temperate change detection measurement.

1) Double ridged horn antennas filled with phantom material
2) Double horn antenna filled with ceramic material
3) Active bowtie antenna

The tested antennas can be seen in the Fig. 5.1 with their impulse responses from the phantom with local heating possibility. For our measurements, the active bow-tie dipole antennas (bowtie shape) were used because of its shortest impulse response and small dimensions (13 mm x 4 mm). For other two UWB antennas the length of their crosstalk was so long that it also affected the response from the place, where the temperature was changed.

We used two active bow-tie antennas (one transmitting antenna T_x and one receiving antenna R_x) at a distance of 2 cm in quasi mono-static radar mode. For reduction of radar signal influence by surrounding effects as vibrations, unwanted antenna movements, changes of antenna contact quality the antennas were fixed in a polystyrene holder. The proper antenna contact to the phantom is very important for the signal quality. For this type of antenna, the magnitude and shape of impulse response is depending on pressure between antenna and phantom. For evaluation of a repeatable and stable pressure, the shape and time duration of the cross talk was used.

5.4.2 Experiment I: Resistor

For our preliminary experiments to identify signal variations caused by temperature changes an electrical resistor of impedance 100 Ω was used. The resistor is heated by current passing through it. To find out the differential signal caused by temperature change, the ON/OFF modulation was applied. The measured temperature on the resistor body is summarized in the Table 5.1. In the Fig. 5.2 is the schematic measurement setup including two antennas and resistor, which is 3.5 cm under phantom surface.

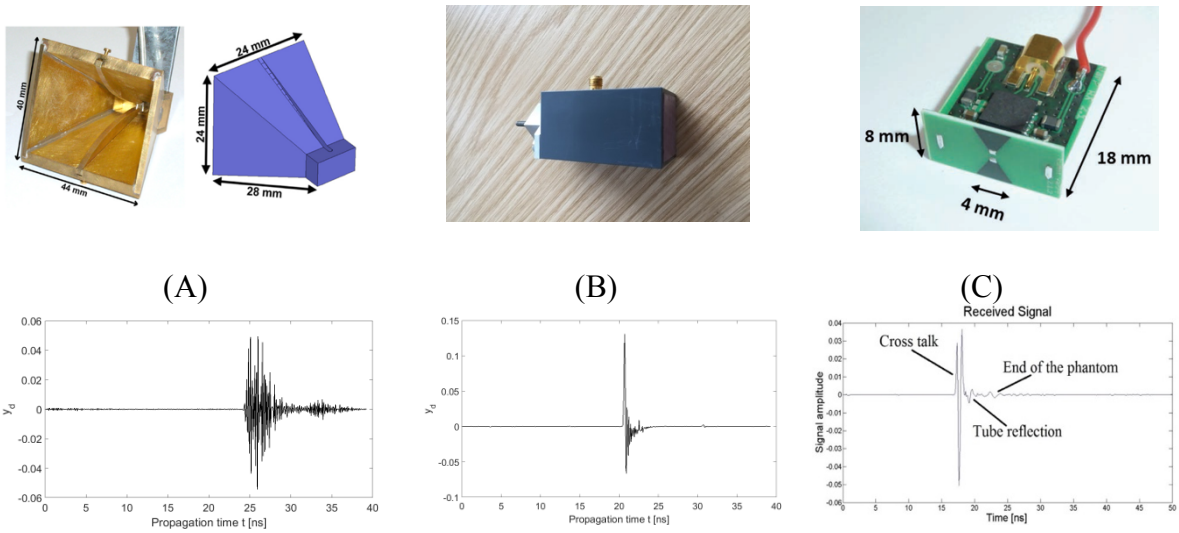

Fig. 5.1 Three tested antennas (A) double ridged horn antenna filled with phantom material, (B) double ridged horn antenna filled with ceramic material and (C) active bowtie antenna with their impulse responses (below each antenna).

Table 5.1 100 Ω Resistor body temperature-voltage dependence (measured).

Number	Voltage [V]	Temperature [°C]
1	2	27.8
2	2.5	29.4
3	3	32.2
4	3.5	35.1

The reflection was measured from a point at a distance of 3 cm under antennas (black line above the resistor in the Fig. 5.2). This reflection time response of 420 seconds duration is plotted in Fig. 5.3. In the time interval 0-100 seconds we turned on the heating (3.5 volts), in the time interval 100-300 seconds the heating was turned off and from time above 300 seconds to the end the heating was turned on again. The reflection behavior in the radar signal is corresponding to the resistor heating activities. Also in interval 150-300 seconds the cooling down effect is present and visible.

5.4.3 Experiment II: Water heating system

In our second experiment we used a water heating system consisting of a thin tube with water circulation which is connected to a water pump (Julabo heating circulator type F12-ED). During the experiment the water inside the tube was heated from the initial

phantoms temperature (20 °C) to 33 °C with the step being one degree. The heating tube was placed 3.5 cm under the phantom surface.

In the signal (see Fig. 5.4), the antenna cross talk, heating tube reflection and backside reflection of the phantom can be clearly distinguished. This distance corresponds to a penetration depth of superficial hyperthermia (for frequency 434 MHz [99]). Into the phantom two temperature sensors were implemented (T_1 and T_2). The heating tube, antennas and temperature sensors positions can be seen in the Fig. 5.5 (A). The measurement duration was approximately 520 seconds. During this time period we gained over 2800 impulse responses. The photo of the measurement setup with phantom, heating tube and polystyrene holder is shown in the Fig. 5.5 (B). In the Fig. 5.6, the measured and pre-processed radargrams with marked heating tube position and heating start point are shown. The heating process starts after 100 seconds. It is important to note that according to the average wave velocity in phantom ($3.6 \cdot 10^7$ [$m \cdot s^{-1}$]) one sampling interval in radargram is equivalent to a distance 3.6 mm approximately.

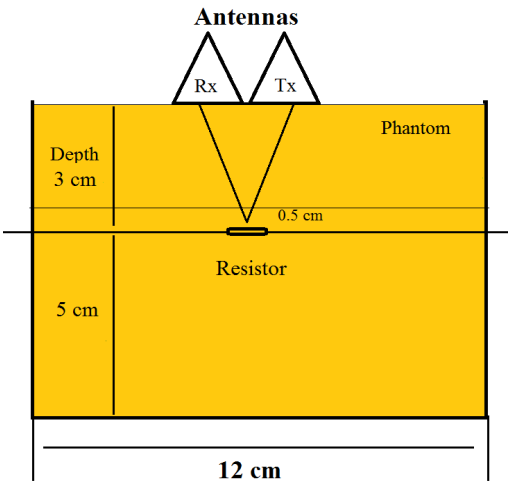

Fig. 5.2 Schematic measurement setup for preliminary detection experiment with resistor.

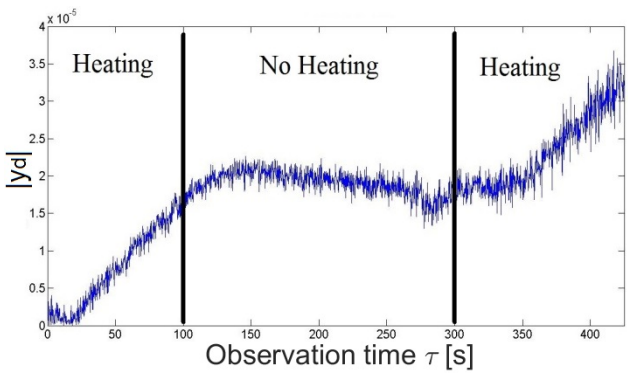

Fig. 5.3 Reflection change at a distance 0.5 cm from the resistor.

The first radargram illustrates the whole measurement after clutter and drift removal (Fig. 5.6). The second radargram in the Fig. 5.6 is extended by attenuation equalization as discussed in chapter 5.3.2. The settling time of the heater to achieve constant temperature at 33 °C was about 90 seconds.

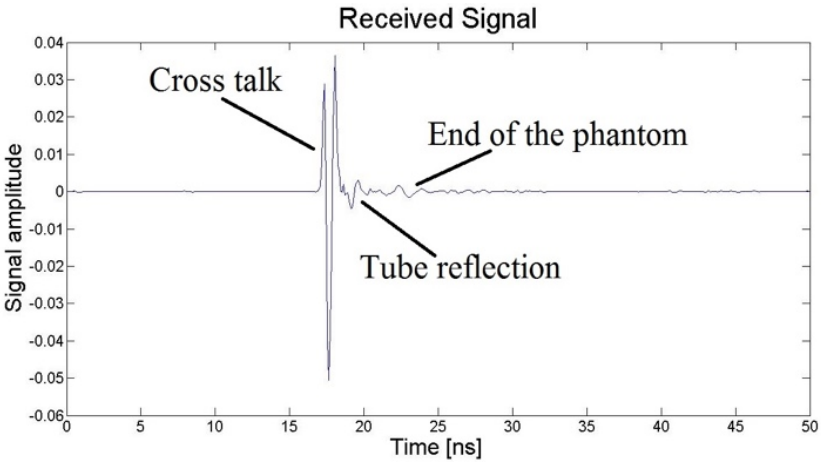

Fig. 5.4 Measured impulse response of the phantom.

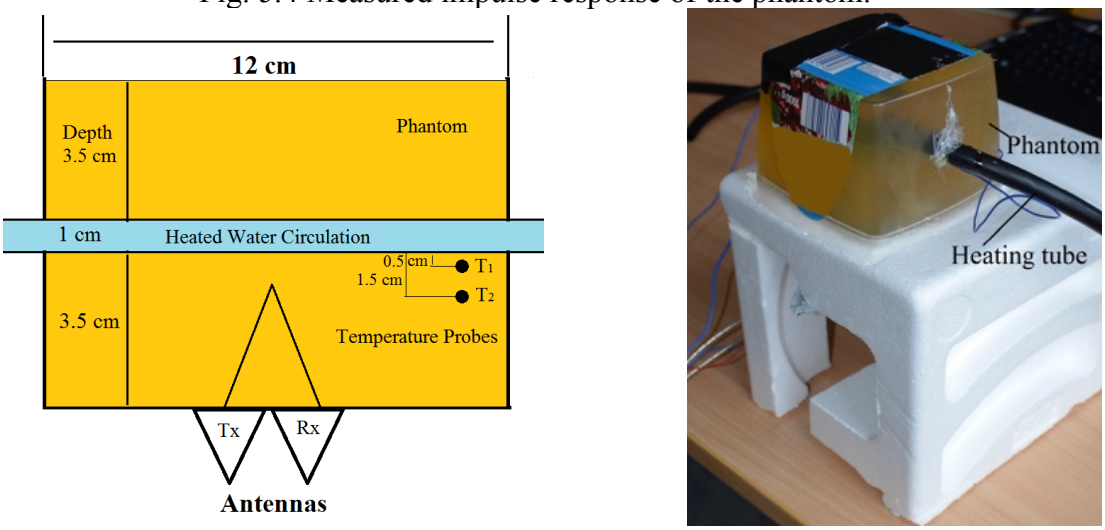

(A) (B)

Fig. 5.5 (A) Schematic measurement setup for temperature experiment with heating tube, (B) photo of phantom with the heating tube.

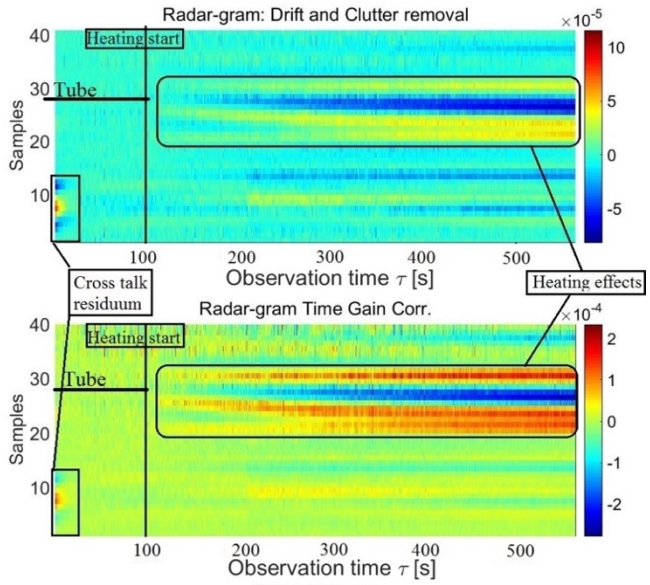

Fig. 5.6 Background subtracted radargrams with drift and clutter removal (top) and with additional attenuation correction (bottom).

In the Fig. 5.7 (A_1 and B_1) the time responses of differential signal y_d from the position of temperature probes T_1 and T_2 (corresponding to the propagation time t during observation time τ) are shown. The graphs below (A_2 and B_2) are corresponding to measured temperature during the heating at points T_1 (0.5 cm from heating tube) and T_2 (1.5 cm from heating tube). The correlation between A_1 and A_2 is 0.92 and between B_1 and B_2 is 0.87, which is corresponding to the strong dependence between reflection and temperature.

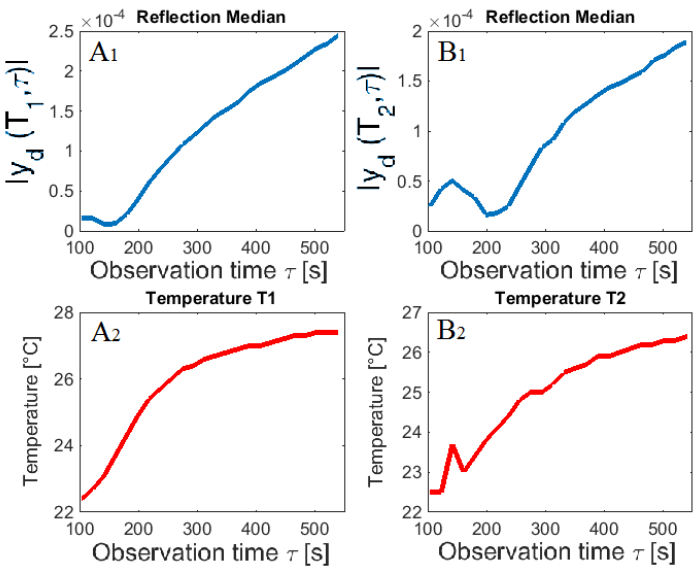

Fig. 5.7 Measured signal difference corresponding to T_1 (A_1) and T_2 (B_1) position, A_2 and B_2 are measured temperatures from T_1 and T_2 probes in case of heating.

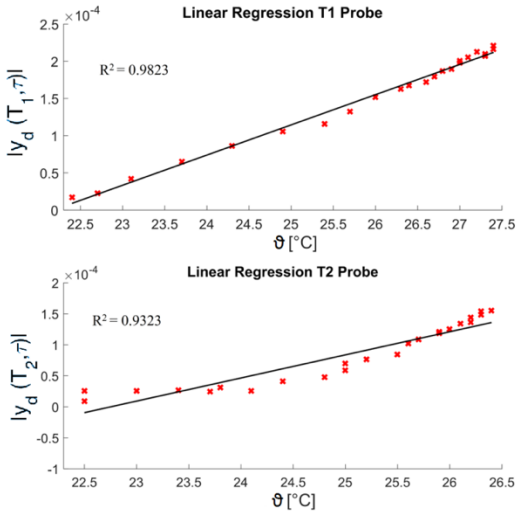

Fig. 5.8 Scatterplots of measured difference in reflection (T_1 top and T_2 bottom) as a function on actual temperature.

Scatterplots in Fig. 5.8 show the reflection depending on temperature in the T_1 and T_2 positions with very high correlation above 90 %. Gained points are fitted by a linear regression.

The results of our initial experiments show that it is possible to detect small changes in the reflected signal caused by temperature variations. We performed two experiments using two different types of heating. The phantom was locally heated up at depth of approximately 3.5 cm (this value is corresponding to the depth of heating for superficial hyperthermia). We performed our first experiments only with one specific phantom (tumorous tissue phantom). For further investigations, we focused to measure with an agar phantom because of its higher temperature stability at temperatures around 45 °C.

5.5 Experiment III: Hot static water

The measurement setup of the third experiment was very similar to the previous one, when we directly attached two “electrically small” (13 x 4 mm) active differentially fed (realized by differential amplifier) dipole antennas (in quasi mono-static radar mode), permanently fixed to the agar phantom in which the heating tube was inserted.

The heating tube is made from polymethylpentene material (TPX). According to our experiences this material has better adhesion to the phantom than glass even in the case of higher temperatures of liquids inside the heating tube. It does not create air gaps. Measurement setup layout can be seen in Fig. 5.9. We changed the heating method which we used in our previous experiments in [96] (resistor and heating pump). Static water

application as a heater allows us to avoid some random effects (random noise) caused by vibrations. We expected the same change in the complex permittivity of water and agar with temperature. The next advantage of this heating method is that it enables heating and subsequently cooling of the phantom in a relatively short time without external intervention.

We prepared three phantoms (according to Fig. 5.9) with different distances (3-5 cm) between antennas and heating tube. Into each phantom three temperature probes (PT 100) were placed at distances of 0.5, 1 and 1.5 cm from the heating tube. In Table 5.2 there is an overview of temperature probe distances from antennas and heating tube. The probes are placed on the other side of heating tube to avoid unwanted responses from metal probes to the electromagnetic wave. We assumed the same heating spreading in all directions from heating tube and consequently the measured temperature is totally correlated with the temperature on the other side of heating tube. We poured hot water into the tube (starting temperature was 87 °C). Due to the thermal conductivity of the phantom, the heat was equally spread to the surrounding area. For these measurements we used an M-sequence radar system with one transmitting output (T_x) and two receiving inputs (R_x). Fig. 5.12 (A) illustrates radar response in case when the temperature was stable in all parts of the phantom (agar, testing-tubes and water).

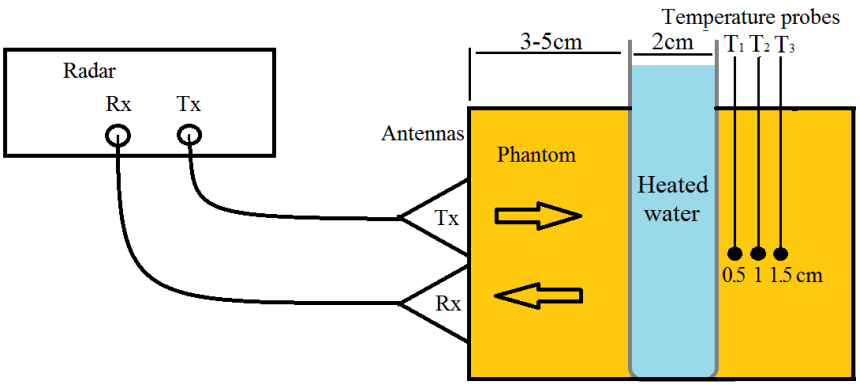

Fig. 5.9 Measurement setup for the third experiment.

5.5.1 Numerical simulation (using proposed 1D model)

Firstly, we analyzed this experiment with included heating tube numerically. We modeled this experiment using our 1D numerical solution described in section 4.5. The model is composed of 20 layers that put together the complete distance between antennas and heating tube when the distance was 4 cm (according to the experiment setup shown in the Fig. 5.9). In the Fig. 5.10 are temperature distribution each layer through the whole observation time.

The first layer (x_0) is representing the homogenous medium of constant temperature (in this case the length of the first layer is 2.5 cm). The initial temperature (as in the experiment) of the phantom (υ_0) was set to 20 °C. The remaining distance (1.5 cm) was divided into 17 layers of constant thickness of 0.088 cm. The 19th layer is representing the heating tube and the last 20th layer is set as anechoic layer. The temperature of layer 2nd, 7th and 13th is corresponding to the real temperature measured through temperature probes T_1, T_2 and T_3. Temperature of the remaining layers is equally calculated between layers with measured temperature. In the Fig. 5.10 (A) is the temperature distribution including temperature of heating tube and the whole setup is terminated by the anechoic layer. The hot water was poured at the temperature 87 °C. In the diagram the temperature is updated each 100 second. In the diagram (B) of the same figure there is, for clarity, temperature distribution only in the phantom (without heating tube). To each layer the complex permittivity according to the temperature change was attributed, which was calculated after the estimation from eq. (4.11) and (4.12) (graphically in the Fig. 4.2). The change in the complex permittivity of water was calculated according to the Ellison model [92].

For this numerical experiment, the Gaussian pulse (bandwidth 1-6 GHz) was used. Each 100th second, the simulation was performed and the results were put in the radargram. From the simulated signals the background was subtracted and the attenuation was corrected. The resulted diagram can be seen in the Fig. 5.11 (A).

Table 5.2 Distances of temperature probes from antennas and heating tube

T probe	$D_{antennas}$ [cm]	$D_{heating\ tube}$ [cm]
T_1	3.5	0.5
T_2	3	1
T_3	2.5	1.5

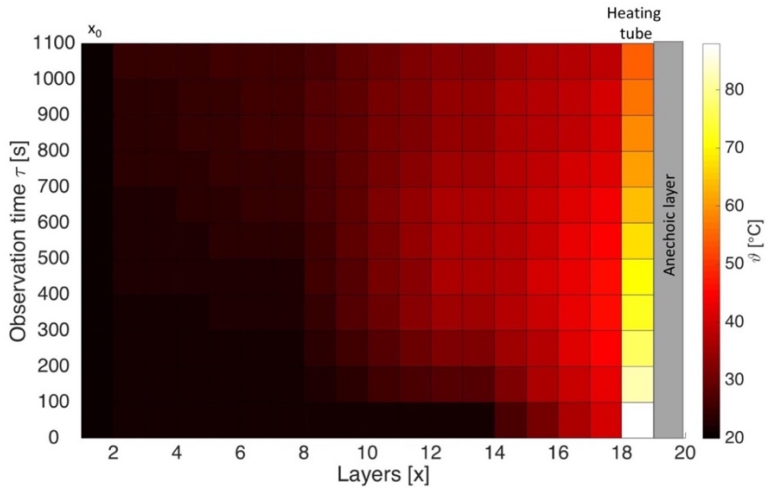

(A)

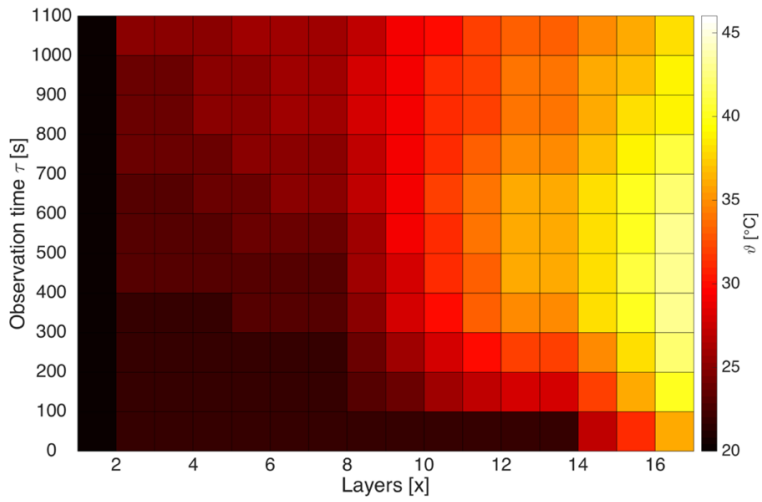

(B)

Fig. 5.10 Temperature distribution in the phantom with heating tube (A) and in the phantom only (B).

5.5.2 Results from the numerical model: Verification by measurement

In the Fig. 5.11 (A) is the resulting radargram from 1D numerical simulation. In the radagram there are reflected signals from the layered medium corresponding to the real measurement. In the Fig. 5.11 (B) the radargram from the measurement is shown. The main responses (in propagation time 1-3.5 [ns]) are shifted by 0.1 [ns], which is acceptable. The difference in the measured radargram are obviously visible resonances outside the area of investigation and the measured radargram is smoother because of higher number of measurements performed per second than in numerical simulation.

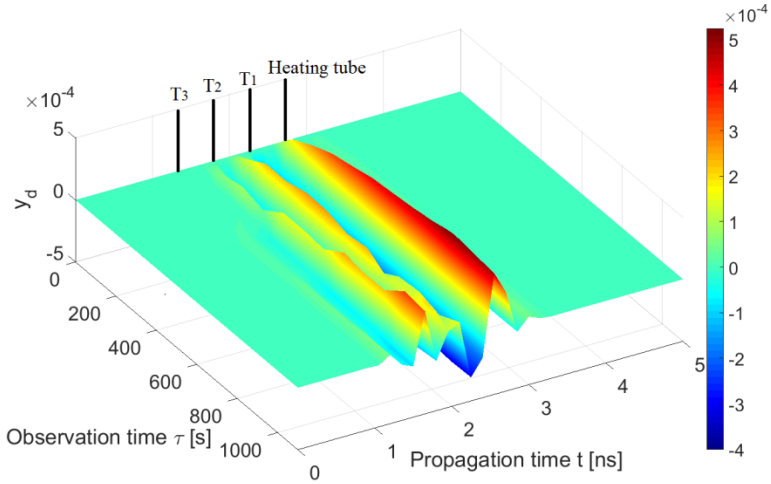

(A)

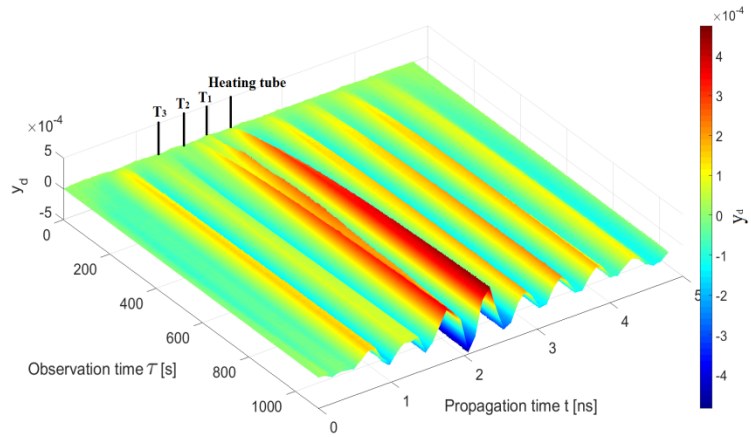

(B)

Fig. 5.11 Simulated radargram (A) and measured radargram (B).

Note of simplifications between the real measurement and numerical simulation. The presented simulations are simplified according to the real measurements. There are two main simplifications:

1) The model is only 1D. The model does not include the radiation spreading into other directions.
2) The antenna properties are also not implemented to the model.

5.5.3 Experiment III results

Fig. 5.12 (B) shows the resulting radargram. The radargram is prepared respecting drift reduction, attenuation in phantom and clutter subtraction as described in section 5.3. Due to the knowledge of the dielectric properties of used phantom, we were able to calculate the

distance from the signal time line, and thus find responses corresponding to the temperature probes positions. Results presented in this section are for the 4 cm distance between the heating tube and the antennas.

Fig. 5.13 displays absolute value of reflection variations in certain depth from the antennas in case of heating (A_1, B_1, C_1 from measurement and A_2, B_2, C_2 from numerical simulation). We chose the positions according to the temperature probes location. The blue curve is representing the mean value of response ($|y_d|$) in time period 10 seconds. The green curves are representing 95 % confidence interval (+/- 2 *std*) of reflection variations. The red curve is the measured temperature at a given position gained from temperature probes (T_1, T_2 and T_3). The temperature curve and measured reflection change have nearly identical shapes as from measurement and from numerical simulation. Fig. 5.14 represents the scatter plot of the reflection-temperature dependence for three different distances from antennas. One can see that the reflection is proportional to the temperature and this dependence can be approximated linearly very well while Pearson's correlation coefficient R is 0.992. With this approximation it is possible to estimate temperature change from the reflection change. From Fig. 5.14 (A) and (B) we estimate linear change dependence of relative permittivity on increasing temperature. This approximation should be applied also for different temperature ranges. In the scatter plot in Fig. 5.14 (B) the radar responses of three independent measurements are typified while correlation being R = 0.967. The slope is specific for each material.

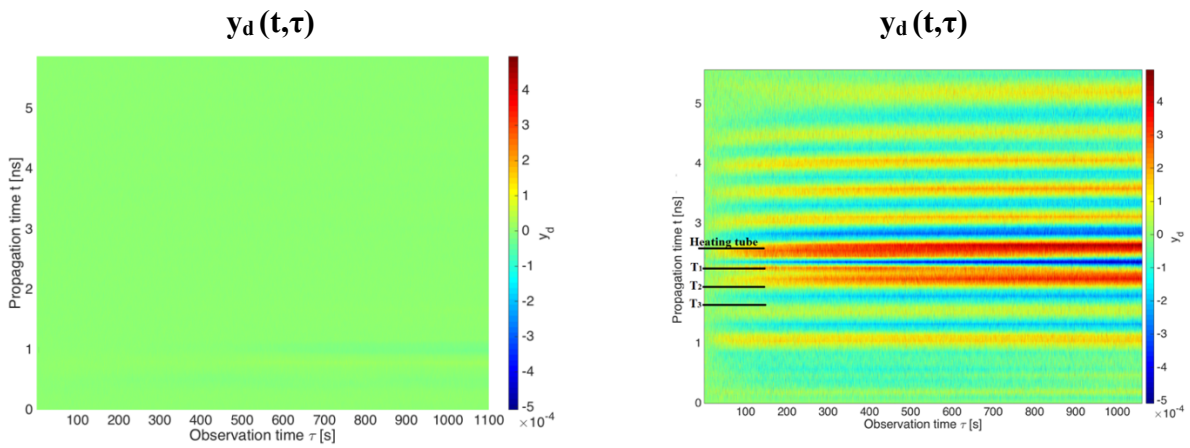

(A) (B)

Fig. 5.12 Radargrams for temperature stabilized phantom (A) and heated phantom (B) after clutter removal, drift and losses elimination (the heating tube was 4 cm from antennas). In (B) the estimated positions of heating tube and temperature sensors (T_1, T_2, T_3) are marked.

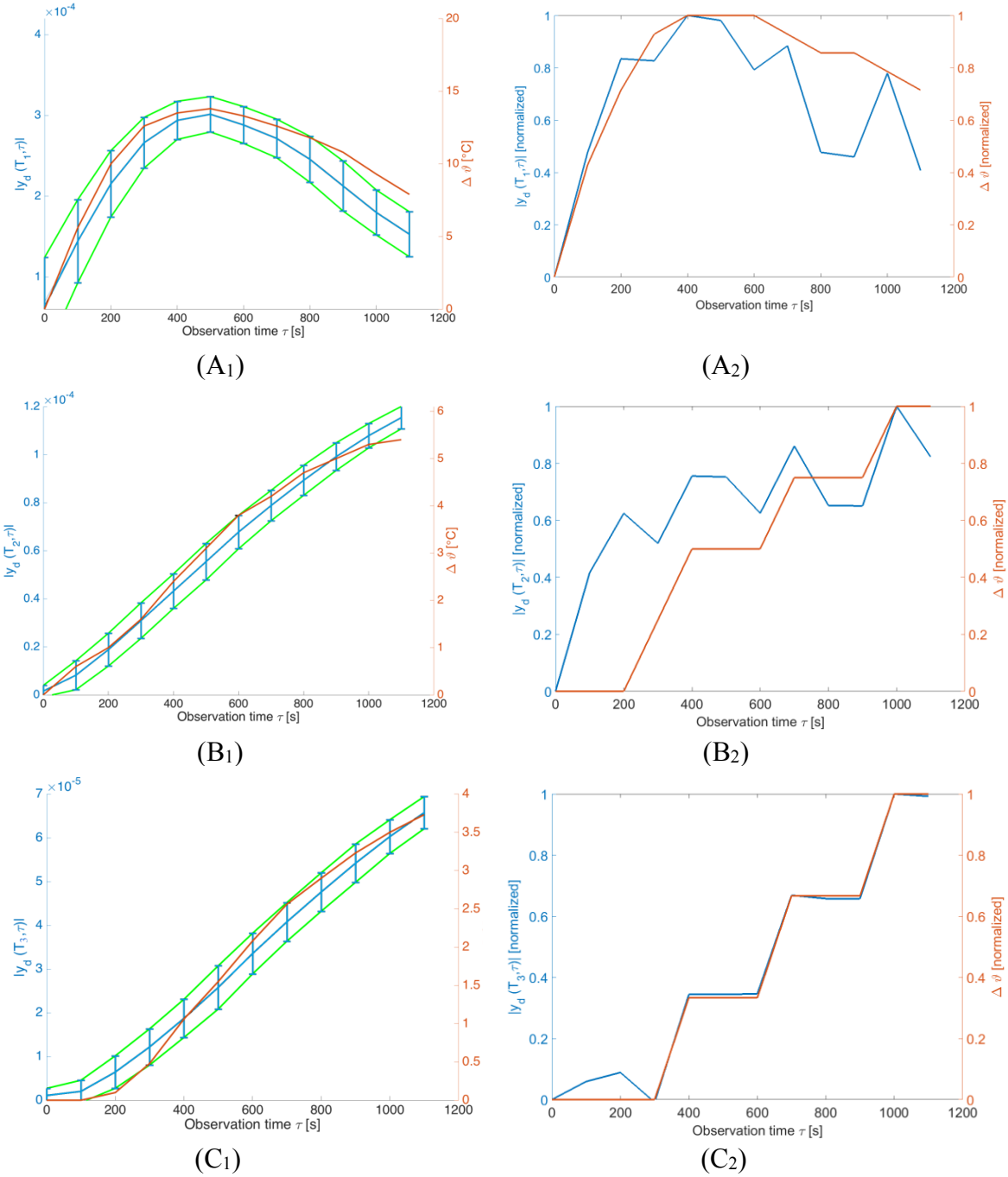

Fig. 5.13 Radar response in position T_1 (A$_1$), T_2 (B$_1$) and T_3 (C$_1$) with simulated courses (A$_2$), (B$_2$) and (C$_2$).

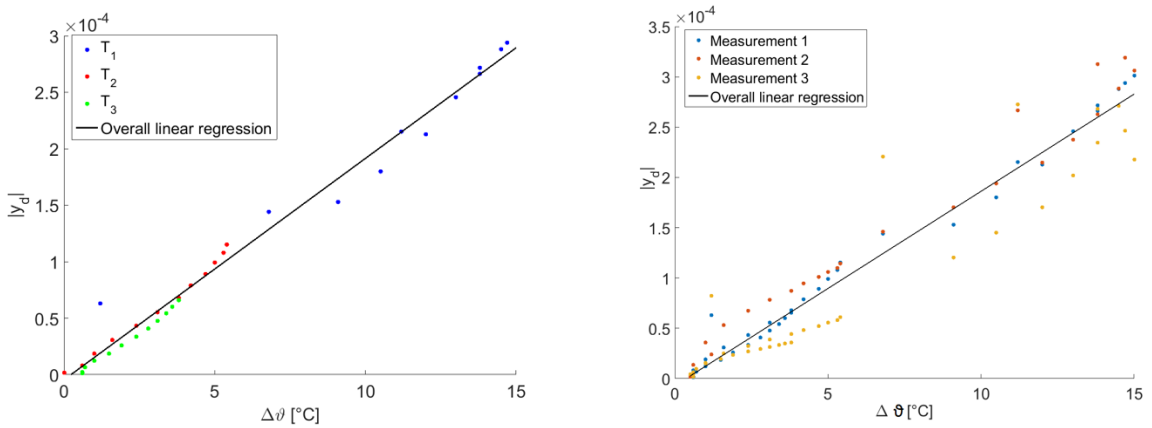

Fig. 5.14 The temperature change dependence of UWB radar reflectivity with linear regression curve of one measurement (A) and three independent measurements (B). Heating tube distance from antennas: Measurement 1 $x = 4$ cm, Measurement 2 $x = 3$ cm, Measurement 3 $x = 5$ cm.

a) Estimation of method resolution

The temperature resolution of presented method of non-invasive difference temperature measurement is the next important parameter. It is dependent on UWB signal bandwidth, signal to noise ratio (*SNR*), attenuation in phantom and type of tissue. The resolution is worsened with increasing distance from antennas. This is caused by a higher attenuation correction which leads to higher noise. The average temperature resolution of the applied method is determined after the following estimation:

$$\Delta\vartheta_{res}(t,\tau) = \vartheta\{\overline{y_d}(t,\tau) + 2\cdot std(t,\tau)\} - \vartheta\{\overline{y_d}(t,\tau)\} \qquad (5.4)$$

where $\Delta\,\vartheta_{res}$ (t, τ) is the temperature resolution of the method, ϑ is temperature, $\overline{y_d}(t,\tau)$ is the mean reflectivity in time interval t (more measurements performed) and $std(t,\tau)$ is the standard deviation of this reflectivity ensemble in time t (level of significance 5 %). The standard deviation is affected by Gaussian noise of the whole system and by repeatability of the measurement. The resolution was estimated for all three positions separately, because the standard deviation was different. The dependence of temperature difference on intensity y_d used in eq. (5.1) can be expressed by regression formula.

$$|\,y_d(t,\tau)| = 1.9\cdot 10^{-5}\cdot\Delta\vartheta - 0.7\cdot 10^{-5} \qquad (5.5)$$

where $\Delta\vartheta$ is temperature difference. The offset in the eq. (5.5) is caused by the dispersion and uncertainty of the measurement.

Calculated method resolutions $\Delta\vartheta_{res}$ and measured standard deviations are listed in Table 5.3.

Table 5.3 Estimation of temperature resolution and standard deviation of used Method

Position	T_1	T_2	T_3
$\Delta\vartheta_{res}$ [°C]	1.3	0.77	0.41
$2std$ [-]	$1.17 \cdot 10^{-4}$	$6.55 \cdot 10^{-5}$	$3.45 \cdot 10^{-5}$

5.6 Experiment IV: Differential temperature imaging using MIMO system

The goal of this experiment was to show the potential of temperature difference distribution in two or three dimensions. For this experiment we have used the UWB MIMO M-sequence radar connected to a hemispherical antenna array in a multi-static mode, containing 24 active antennas arranged in a breast shape (see Fig. 5.15 (A)). This experimental system was developed at the Technische Universität Ilmenau (Germany).

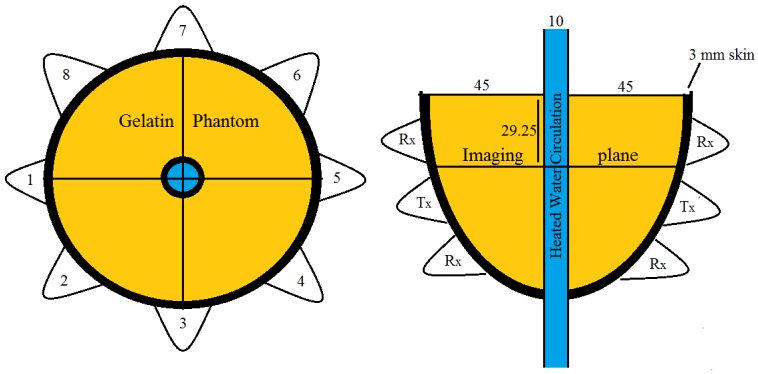

(A)

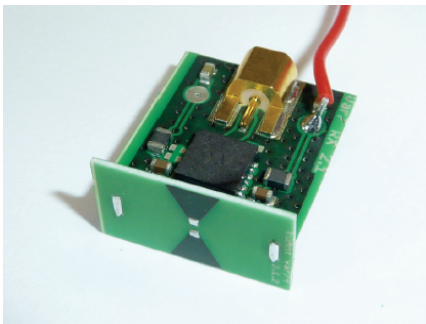

(B)

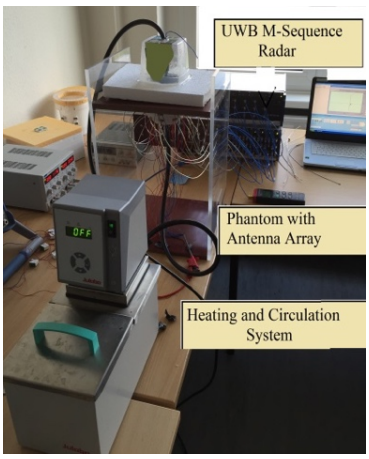

(C)

Fig. 5.15 Breast phantom with antennas placement (A), active dipole antenna 8x4 mm used for imaging (B) and MIMO measurement setup.

5.6.1 Special breast shape phantom

For experiments using the MIMO system, we developed a curved breast phantom with the heating possibility (based on tissue mimicking oil-gelatine phantoms) according to [98].

The phantom was composed of 3 mm thick skin (made from silicon with carbon powder) and was filled by gelatine phantom material (ε_r' = 68 and σ = 2 S/m for 3 GHz) [98]. Used phantom filling contained only gelatine and this phantom is dielectrically imitating the tumorous tissue. We used it because of higher melting temperature than phantoms with higher oil content. In the center of the phantom a thin tube was placed. The tube was connected to the water pump of internal heating. During the experiment the continuously heated water was circulated through the phantom. Phantom with antenna array layout and measurement setup are shown in the Fig. 5.15 (A) and (C).

5.6.2 2D image reconstruction

For the image reconstruction of backscattered energy, the two-dimensional space-time beamformer algorithm "Delay and Sum" (DAS) was implemented. For each two-dimensional image reconstructions, signals from 16 antennas (8 transmitters and 8 receivers) were used. To improve the final image we left out channels (from reconstruction procedure) of an angle wider than 90° between antennas according to [100].

The DAS algorithm enables calculation of the sum intensity of each focal point respecting antenna positions and using knowledge of average propagation wave velocity in the phantom. The DAS algorithm can be described according to the following formula for multi-static antenna array [101]. The signal intensity I of focal point (r_0) is:

$$I(\boldsymbol{r}_0) = \left(\sum_{n=1}^{N} \sum_{\tau_w=-T_w/2}^{T_w/2} y_d(t + \tau_w(\boldsymbol{r}_0) + T_w) \right)^2 \qquad (5.6)$$

where N is the number of channels, y_d is recorded radar signal without clutter, $\tau_w(r_0)$ is time delay of focal point and T_w is predefined time-window.

5.6.3 Experiment and 2D imaging results

Results from two-dimensional reconstruction using breast phantom are presented in Fig. 5.16. Initial state of all breast phantom parts was 20 °C. This is taken for the background subtraction. During the experiment the water inside the phantom was circulating and continuously heated from 20 °C to 45 °C, with steps being one degree per 8 seconds. The complete measurement duration was 480 seconds. The system is able to obtain all signals needed for reconstruction in every 8 seconds. Image reconstruction time needed for one image is around 20 seconds for all procedures involving signal processing. The reconstructed data are affected by artefacts which are obviously caused by insufficient number of antennas.

With higher number of antenna, the inhomogeneity would decrease.

To correlate temperature change with intensity at given point we measured the temperature at two test points placed in the phantom (because of artefacts we choose points in the radiating axis of antenna where data is least affected by artefacts). The first one was in fact the temperature of water circulating through the phantom (position [50 mm, 50 mm] in the Fig. 5.16) and the second one was placed at the 1.5 cm distance from the centre of the phantom (position [30 mm, 50 mm] in the Fig. 5.16). Normalized data of intensity at focal points (which is a sum of all signals from given chosen distance r_0) coming from temperature measurement are demonstrated in the Fig. 5.17. Data was normalized according the eq. (5.7).

$$\vartheta_{norm} = \frac{\vartheta_{measured}}{\vartheta_{max}} \qquad (5.7)$$

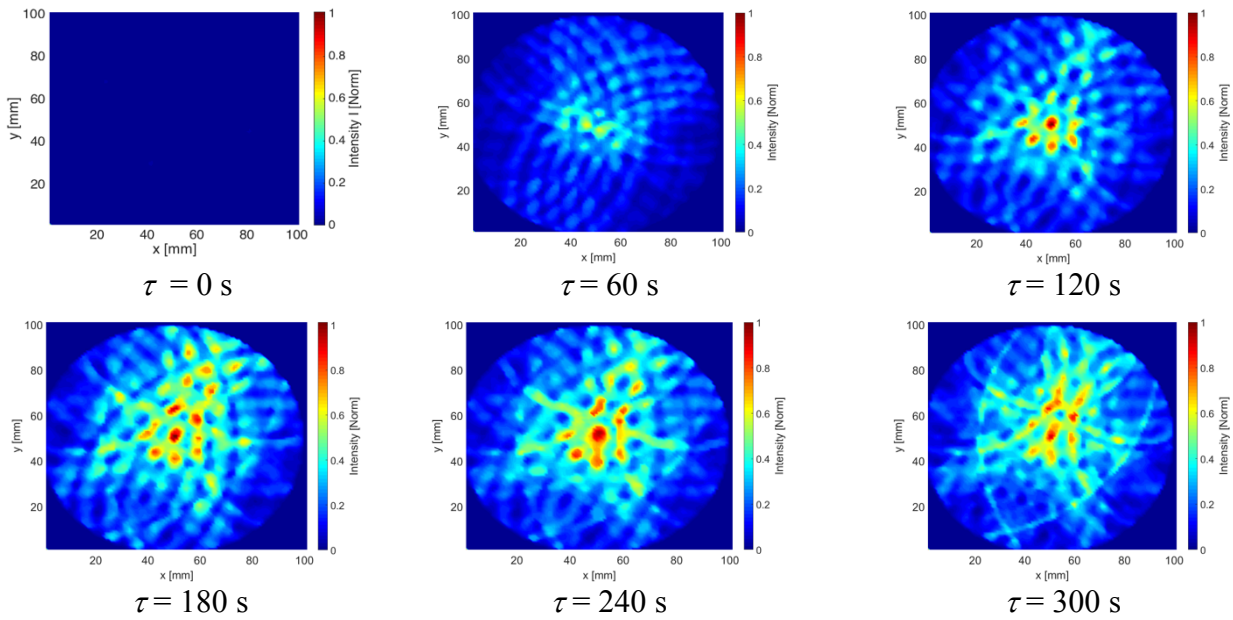

Fig. 5.16 Reconstructed 2D results images obtained each 60 seconds.

Presented results of normalized point intensity (sum of signals) of measured and normalized temperature (Fig. 5.17) are corresponding to our findings in previous section resulting that the reflectivity is correlated with temperature (nearly linear relation). The Pearson's correlation coefficient for water (blue curve) is $R = 0.97$ (standard deviation $\sigma = 0.05$). For gelatine phantom (orange curve) is $R = 0.91$ and $\sigma = 0.025$.

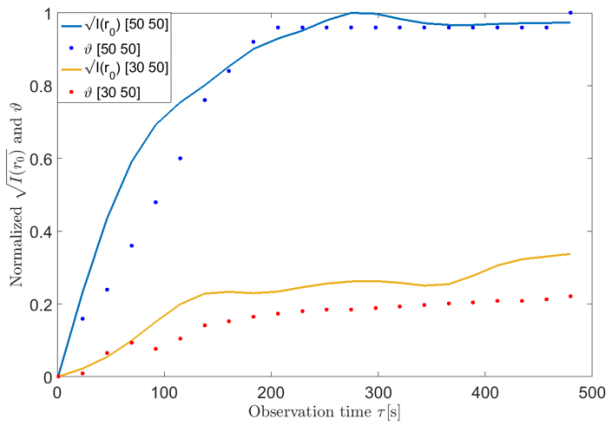

Fig. 5.17 Normalized rooted point intensity $\sqrt{I(r_0)}$ of reconstructed 2D figures from Fig. 5.16 and corresponding temperature plotted in time dependence.

5.7 Conclusion of chapter 5

In this part of the dissertation thesis we described and further explained the principle of temperature change detection using UWB radar. We proposed first initial experiments (using resistor as a heater) and the results of experiments show that it is even possible to detect some changes in the reflected signal which are caused by heating. Due to the problems with temperature stability of the oil-gelatine phantom in the following experiments an agar phantom was used. In the following experiments, we extended our initial experiments with the reflected signal variations from a heated area. We proposed some specific measurements with evaluation which were conducted to explore a correlation and relationship between changes in reflectivity and temperature. Results gained from bi-static measurements were quantified. The temperature was mapped by using the control temperature probes and by infrared camera. According to our results the UWB M-Sequence radar sensor technology is apparently applicable for this kind of application. The experiment with homogenous phantom has shown that the sensor is able to detect weak signal variations at a depth of 3.5 cm with decent accuracy. The results of the experiment with static hot water were compared with numerical simulation results. The data from thermocouples were compared to the measured reflected signal intensity from the heated phantom with good agreement. The result is that spatial resolution of this method is sufficient. In our opinion, this method is feasible and stable with sufficient temperature and spatial resolution. It is suitable for clinical temperature monitoring usage in thermotherapy. The second experiment was concerning a breast shape phantom with an external heating system. For the measurement, an experimental MIMO system of 24 antennas was used. We implemented a two dimensional

reconstruction algorithm mainly based on generally known Delay and Sum algorithm. The system was tested on a proposed heterogeneous phantom of breast with heating. In this study we found that it is possible to detect changes in a UWB radar receiving signal caused by temperature changes within temperature ranges of hyperthermia treatment. The image refresh rate is now around 20 seconds but this can be improved by faster hardware and better signal processing procedure implementation. In that way, the limiting factors of the radar approach in temperature changes detectability are noise, material conductivity and the strength of the temperature permittivity change.

6 Chapter: Combination of Microwave Hyperthermia Applicator System and UWB Temperature Change Detection System

This chapter is based on following published papers:

- O. Fiser, I. Merunka, and J. Vrba, "Microwave hyperthermia system for head and neck area with noninvasive UWB temperature change detection," in *2017 Progress In Electromagnetics Research Symposium - Spring (PIERS)*, 2017, pp. 1657–1662.
- O. Fiser, I. Merunka, and J. Vrba, "Numerical feasibility study of new combined hyperthermia system for head and neck region," in *2017 47th European Microwave Conference (EuMC)*, 2017, pp. 719–722.

6.1 Introduction

The main topic of this chapter is the study of the combination of the two systems:

A) the hyperthermia treatment (i.e. for treatment of tumors in head and neck region)

B) the differential non-invasive temperature monitoring system based on UWB radar measurement.

The main idea is to use the temperature monitoring system as a feedback and controlling system for the hyperthermia treatment systems during the heating (schema can be seen in the Fig. 6.1). The UWB differential temperature measurement system offers advantages compared to other methods that are currently used in hyperthermia for temperature monitoring. The "etalon" in hyperthermia non-invasive temperature measurement system is MRI. Compared to this method the temperature change detection based on UWB radar is of a lower purchase price. Also, the maintenance cost is negligible in comparison with the UWB radar cost. The MRI has very good temperature resolution in the centre of the gantry (in the middle of the human body). With the distance from the centre the temperature resolution is decreasing. According to our results from the previous sections the temperature resolution of the UWB radar is on the contrary decreasing with the distance from antennas. This means that the temperature resolution of the UWB radar method decreases with the distance from the surface.

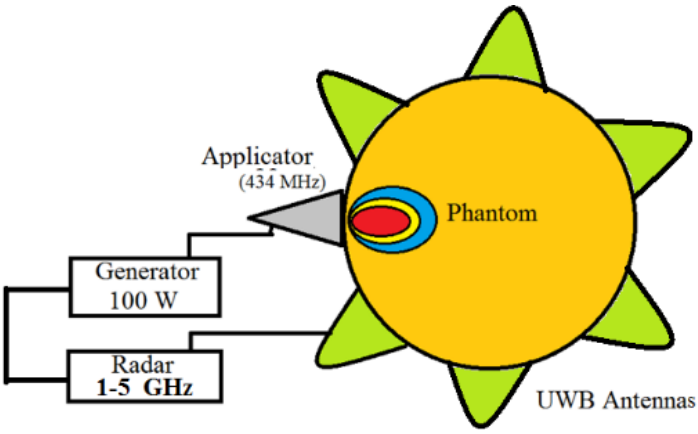

Fig. 6.1 Schema of the microwave hyperthermia system controlled by UWB radar system as a thermometer.

This chapter is divided into two subchapters. In the first chapter, we present a feasibility study of usability of UWB temperature system based on UWB radar in head and neck region. We combined this system with our microwave hyperthermia system proposed in previous chapters. The second subchapter deals with the measurement of the transmission between

single element of the hyperthermia system for head and neck system and passive UWB dipole antennas.

6.2 Expected interference problems

The combination of the microwave hyperthermia system working on the frequency 434 MHz and UWB radar working on the frequency band 1-8 GHz can cause some interference problems that can be expected and must be avoided.

The hyperthermia system is using output power 100-500 Watts (based on the application). The working frequency band of the used UWB radar is relatively very close to the operational frequency of the applicator. This can cause interference between these two systems. In case of the higher power transmission the radar sensor could be destroyed.

When the transmitted power between hyperthermia system and UWB radar sensor is below the level at which the sensor will not be destroyed, the non-invasive temperature measurement can be performed also in case of microwave tumor heating. This is opening very challenging tasks and problems how to perform the signal processing.

6.3 The numerical feasibility study in head and neck region

The main topic of this sub-chapter is the design and demonstration of combination of the hyperthermia applicator system for head and neck area (previously described) working on frequency 434 MHz with UWB radar antenna array for differential temperature monitoring.

The premise of safety and successful hyperthermia treatment is the careful treatment planning (using 3D patient model) and quite controlled temperature distribution in heated area. The most widely used method for temperature measurement during hyperthermia treatment is the classic invasive thermometric probe deployment (e.g. thermocouples in local points).

6.3.1 Differential temperature imaging system

The detection principle of temperature change via UWB radar signal is based on a fact that the complex permittivity is changing with temperature. And temperature changes with the distance. In [96] we have demonstrated that it is possible to detect these changes by UWB microwave radar in biological tissues. The antenna array for non-invasive differential temperature change detection is composed of 8 dipole antennas (dipole dimensions: 21 x 11

mm). These antennas are excited by the UWB pulse in the frequency band 1-8 GHz. The values of relative permittivity and specific conductivity of all considered tissue temperature (at starting temperature 37 °C) have been taken from IT'IS Foundation database [47].

6.3.2 UWB antennas for differential temperature imaging system

For temperature change detection, we proposed the UWB bow-tie antenna on Rogers substrate RO4003C with thickness 1.524 mm. The antenna overall length (both arms and the gap together) is 20 mm (see Fig. 6.2 (A)) with 1.5 mm gap between arms. The best performance of the antenna is in the bandwidth 1-6 GHz (reflection coefficient frequency course in the frequency bandwidth 1-5 GHz can be seen in Fig. 6.2 (B)). The resonant frequency is at 1.654 GHz. The transmitted Gaussian pulse used in this numerical feasibility study can be seen in the Fig. 6.3.

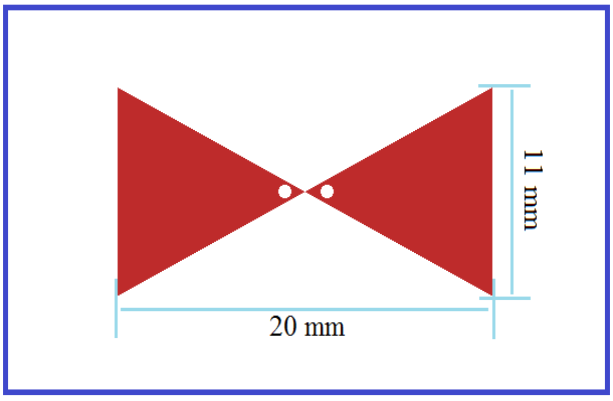

(A)

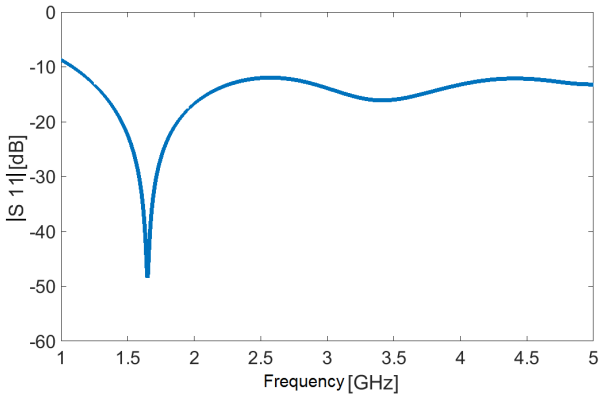

(B)

Fig. 6.2 Bow-tie imaging antenna (A) and antenna reflection coefficient $|S_{11}|$ (B).

6.3.3 Numerical phantom design

For numerical feasibility study, we proposed two phantoms. The change in dielectric parameters due to heating (temperature increases in tumor) we formulated a model using the

pure water temperature dependency model which we adopted from [92]. This approach was enabled due to high water content in tissue. The estimation of relative permittivity is described by eq. (4.11) and specific conductivity σ by eq. (4.12).

The estimation of temperature dependence of relative permittivity and specific conductivity of human muscle in the temperature range from 36 – 50 °C can be seen in the Fig. 6.4 (A) and (B).

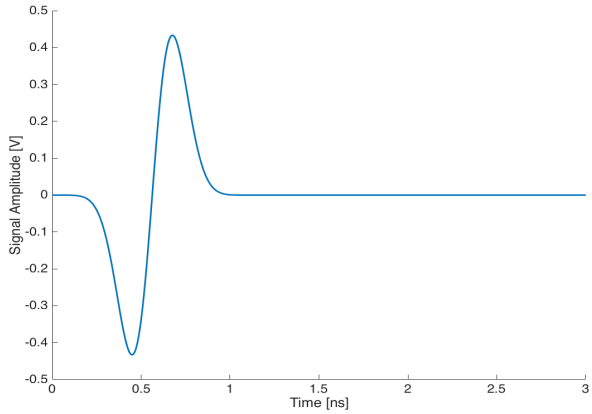

Fig. 6.3 Transmitted Gaussian pulse in time domain (frequency bandwidth 1-8 GHz).

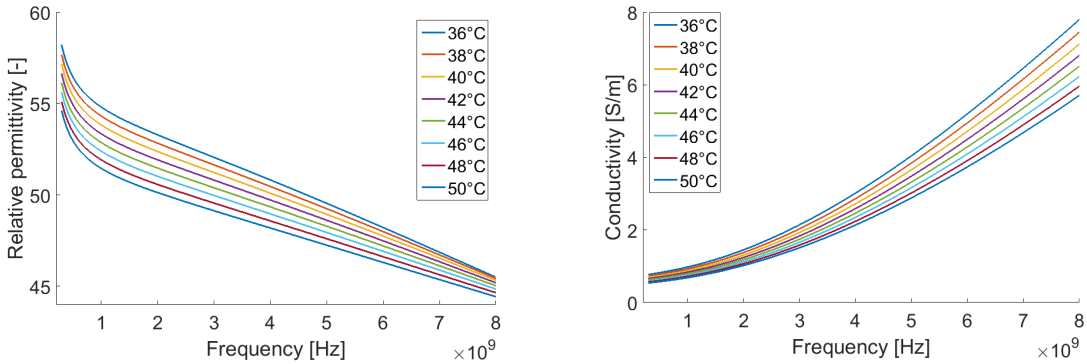

(A) (B)

Fig. 6.4 Estimated frequency and temperature dependence of relative permittivity (A) and specific conductivity (B).

a) Simple cylindrical phantom

In order to demonstrate functionality and performance of the UWB antenna array we proposed a simple homogenous phantom. The muscle phantom is of cylindrical shape, 160 mm in diameter and of constant temperature 37 °C. This simplified model is representing the average size of the head and neck. There are 8 UWB dipole antennas 10 mm under phantom surface. Opposite to the antennas there are three hemispheres representing the heated volumes with constant temperature (45 °C, 42 °C and 40°C) inserted to each other. The distance between antennas and first layer of an inhomogeneity is 70 mm in first case

and 90 mm in second case (valid for all antennas in the model). Whole numerical model can be seen in Fig. 6.5 (A).

b) 3D model of real oncological patient

The second numerical model is a model of real oncological patient with large tumor. The 3D model was reconstructed from CT scans by segmentation software iSeq. The numerical patient is modelled with our hyperthermia system (four waveguides and water bolus) and differential imaging system using 8 UWB dipole antennas (see Fig. 6.5 (B) and with temperature distribution after 8 minutes of heating (C)). After EM simulation we used distribution of the Specific absorption rate (*SAR*) for calculation of temperature distribution using Penne's Bioheat relationship. For reconstruction purposes the average relative permittivity of the phantom was used (this approach will be used also in clinical practice). The average relative permittivity was derived from "time of pulse flight" through the phantom for each antenna separately. This model is very close to the real scenario. After heating, the heated part (tumor mostly) was divided into 24 layers (width of each layer was 1 mm) of different temperature. The dielectric parameters were updated according to the dependency in the Fig. 6.4.The numerical phantom can be seen in Fig. 6.5 (B) and Fig. 6.6 (A), (B).

6.3.4 Simulation setup and image reconstruction

We used results from hyperthermia thermal simulation (temperature distribution) which were used for the creating of sandwich structure creating in the phantom according to the temperature distribution. Consequently, we performed the EM simulation in time domain using dipole array. We reconstructed the final image using reflected signals from heated part and Delay and Sum reconstruction algorithm (eq. (5.6)). All EM and thermal simulations were made using Sim4life simulator. Because the signal reflection from heated area is overlapped by background (i.e. antenna crosstalk, clutter, attenuation and other unwanted reflections in phantom), we subtracted these phenomena from all signals. The sum signal intensity I of focal point (r_0) according to the Delay and sum algorithm.

The updated complex permittivity distribution in heated area was inserted into the numerical phantom. The dielectric parameters were corresponding to the temperature at each position in the model. Then we performed 8 numerical simulations for each case of temperature distribution. In each radar simulation we set 1 transmitting and 7 receiving UWB dipole antennas. The transmitted signal is a Gaussian signal shape with bandwidth 1

– 8 GHz. Overall 64 signals were gained and used for temperature profile reconstruction purposes.

Before reconstruction procedure of very small signal variations the two following phenomena were mitigated:

- Clutter subtraction
- Signal intensity correction (due to attenuation in phantom)

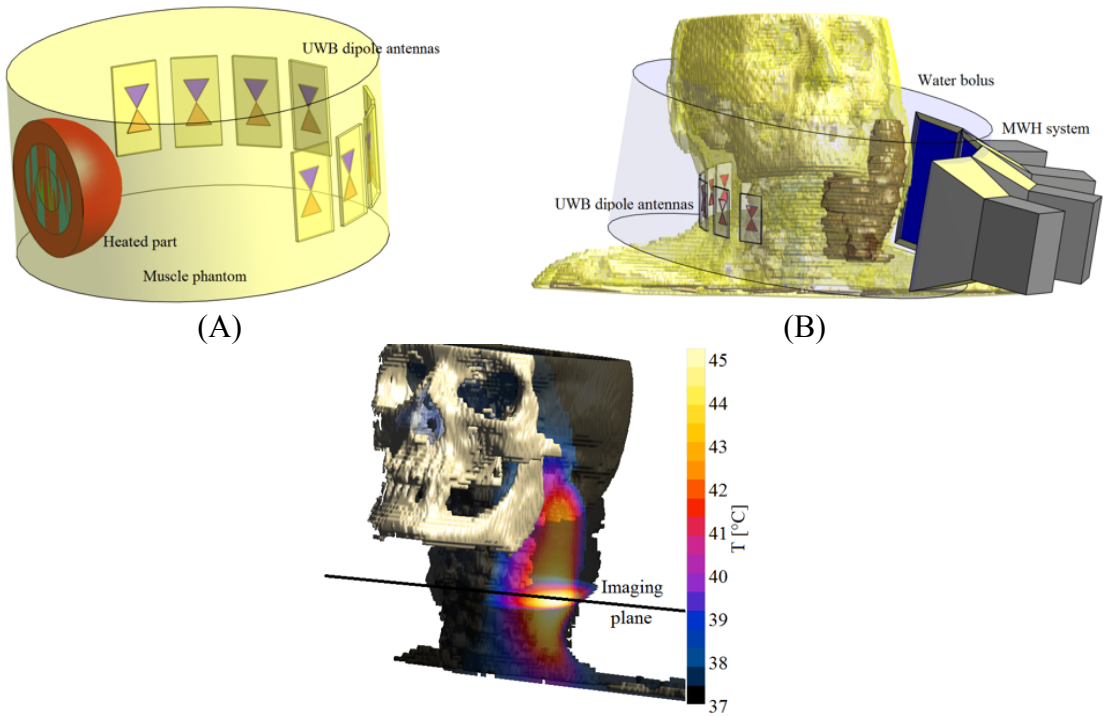

Fig. 6.5 Numerical model of homogenous phantom with 8 UWB antennas (A), numerical model of oncological patient with hyperthermia system with differential temperature imaging system (B) and temperature distribution in tumor after 6 minutes of heating (C).

6.3.5 Reconstruction results

The results gained from the image reconstruction are presented in this section. The transmission crosstalk between antennas is - 60 dB in average. The change in antenna reflection coefficient parameter in case of change of complex permittivity due to the heating is of the order of several percent.

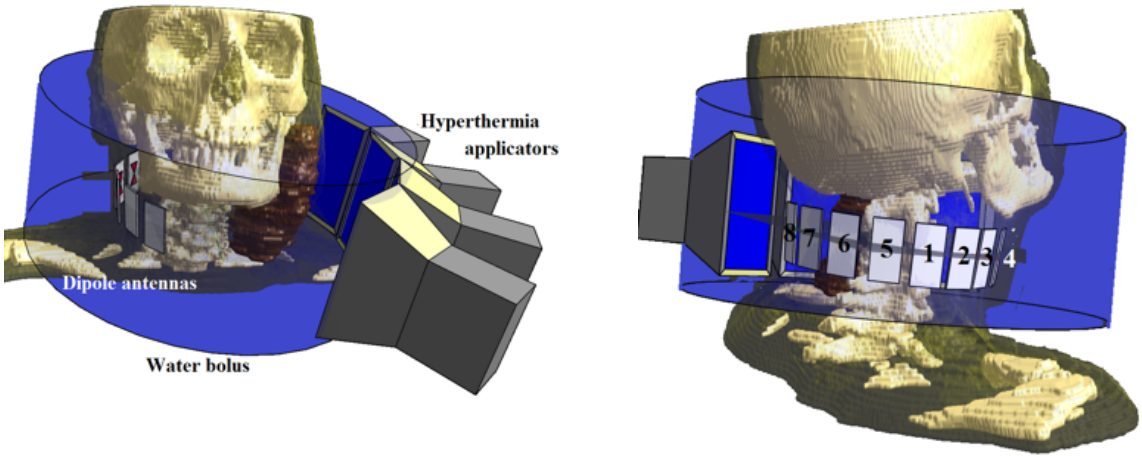

(A) (B)

Fig. 6.6 Numerical 3D model of real patient with large tumor (A) and another view with number of antennas (B).

a) Simple cylindrical phantom

In the Fig. 6.7 (A) and (B) the 2D reconstructed signals intensity (mapped using the Delay and Sum beamforming algorithm) of simple cylindrical phantom are presented (with marked layers positions representing temperature changes; (A) position one, (B) position two). In reconstructed image the reflection from each layer can be clearly identified. In both cases, the greatest reflection is from the first layer. In the Fig. 6.7 (C) there is a cross section of the reconstructed images in the centre of axis X=80 mm. There are three peaks corresponding to each layer being distinguishable for both positions. The maximum detectable distance of inhomogeneity for the first layer was 100 mm from antennas (in numerical simulation). Beyond this limit the changes in signal were undetectable due to the high losses in tissue. In the Fig. 6.8 there is an example of reflected signals from heated area used in reconstructions. The blue curve is the reflected signal between antenna number 6 and 1. The red curve between antenna number 4 and 1 (the heated area is further).

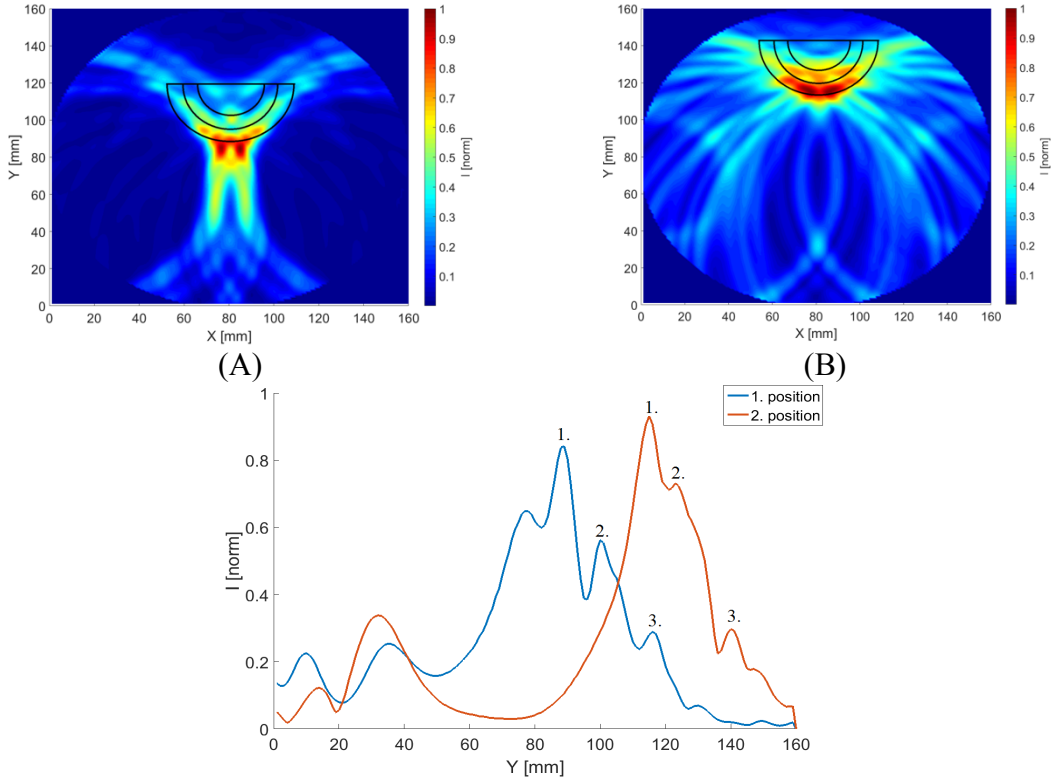

Fig. 6.7 2D reconstructed images with marked position and shape of inhomogeneity for the first position (A) and second position (B). (C) is the cross section of reconstructed images (A) and (B) in centre position X=80 mm.

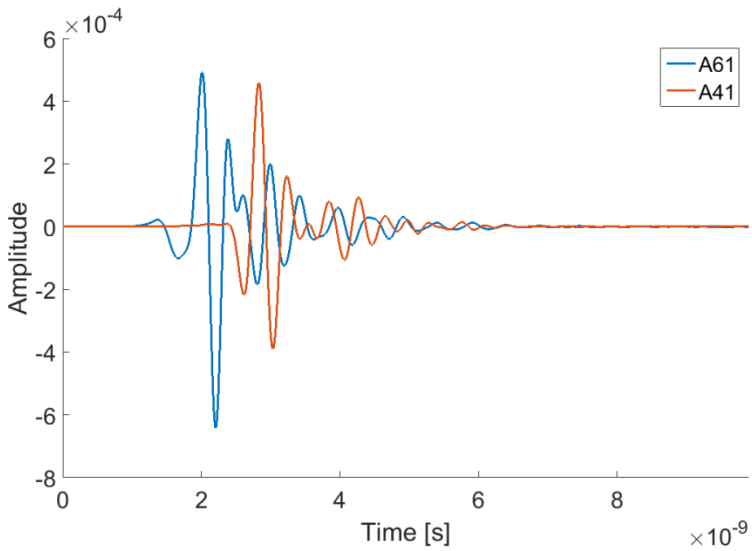

Fig. 6.8 Signals received as reflections from heated part in the homogenous numerical phantom for specific antennas.

b) Patient model with tumor

The Fig. 6.9 (B) shows the reconstructed image of reflected signals from heated part of tumor after 8 minutes of heating. The strongest reflection was detected on the transition between antenna and skin subtracted from signal as a background. This effect weakens signal propagating through the phantom to the heated area. Despite these effects the changes in the target are clearly visible and some changes in tumor were detected. The reconstructed image (Fig. 6.9 (B)) is corresponding to the simulated temperature distribution in the Fig. 6.9 (A). However the correlation between temperature and obtained image is not perfect. This problem is caused by the high specific conductivity in our model, low number of antennas, antenna positions and by reconstruction algorithm.

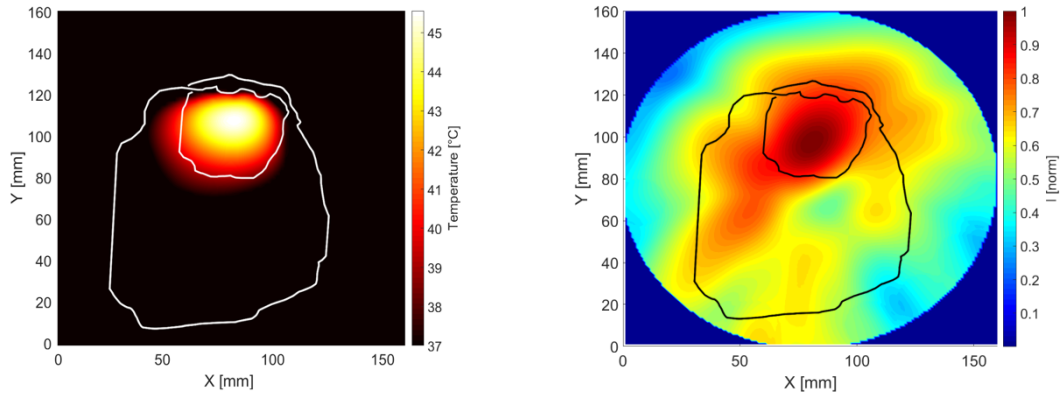

(A) (B)

Fig. 6.9 Temperature distribution gained from numerical simulation (A) and reconstructed image (B) with marked neck and tumor position.

To examine new possibilities of this technique, three temperature distributions from Fig. 6.10 (A_1, A_2 and A_3) were used for reconstruction and following analysis with improved reconstruction algorithm. The results gained from 2D reconstruction are presented in the Fig. 6.10 (B_1, B_2, B_3). In all reconstructed images the contours of neck in imaging plane and contours of the tumor position are marked. The antenna beam width in the improved DAS algorithm was set to 64°. The starting temperature of all tissues was set to 37 °C.

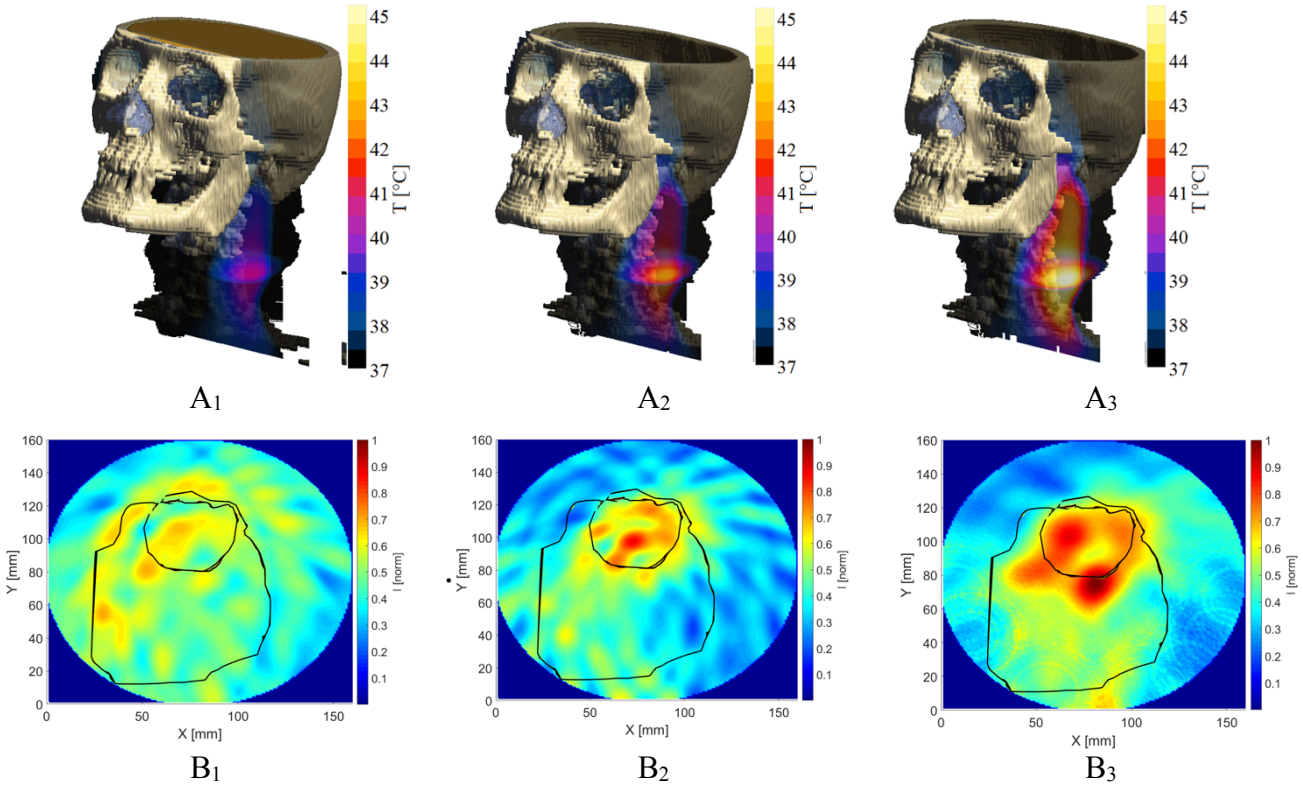

Fig. 6.10 A_1, A_2, A_3 are temperature distribution after 2,4 and 6 minutes of heating (total power 100 W). B_1, B_2, B_3 are reconstructed images of each temperature distribution.

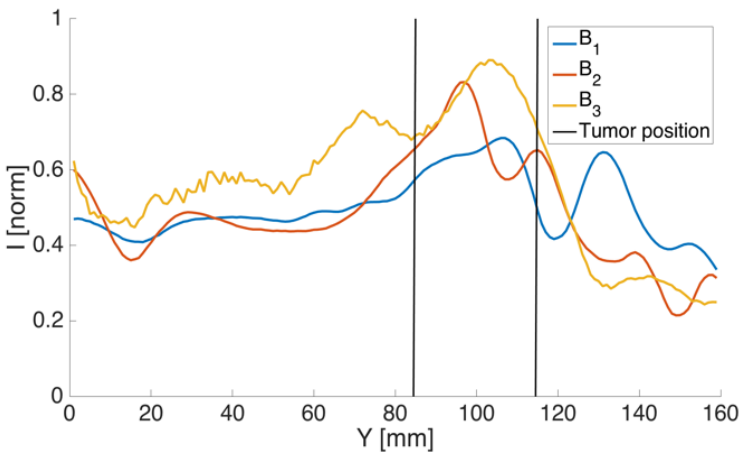

Fig. 6.11 Cross section through reconstructed images $B_{1\text{-}3}$ from Fig. 6.10 when X=80 mm.

In the Fig. 6.10 (B_1) there is the reconstructed image after 2 minutes of heating. The maximum temperature in the phantom was 39 °C - this represents only 2 °C increase. The long distance (between antennas and reflections) and low contrast in complex permittivity change is causing uncertainty in the location of the temperature change and low signal to

noise ratio. Despite these effects, the highest intensity in the image is located in the tumor position.

Fig. 6.10 (B_2) is the reconstructed image of the temperature distribution A_2 (after 4 minutes of heating). The temperature equally increased by 2 °C in the heated area against A_1. The reconstructed image B_2 shows also the intensity increase of the intensity in the tumor location and in the surrounding area. This is caused by the principle of the DAS reconstruction algorithm.

According to our study results, the minimum detectable temperature change (corresponding to our simulation setup in head and neck region) is 1.2 °C. This temperature change (actually the change of complex permittivity) caused the sufficient contrast which was clearly visible in our 2D reconstructed images. The temperature resolution is depending on the distance between antennas and reflection. This is because of the attenuation in the phantom. After 6 minutes of heating the wanted temperature distribution was achieved (temperature range 41-45 °C was achieved in 96 % of the tumor). The reconstructed image can be seen in the Fig. 6.10 (B_3). The maximum intensity is located in the tumor and signal/clutter it is the highest because of the higher contrast between heated tumor and surrounding area.

6.4 Chapter 6 conclusion

The results from our numerical experiments show the potentiality of this approach. According to this study, it is possible to detect low changes in tumor permittivity, which is caused by local temperature change. For simulation purposes two numerical models with frequency and temperature dispersive parameters of biological tissues were used.

We presented an experimental antenna setup for UWB temperature change detection within the microwave hyperthermia treatment. To avoid the interference between hyperthermia system and UWB radar signal the system will measure the differential temperature. This measurement will be done at the moment when the microwave heating will be turned off.

The numerical simulation of the homogenous phantom shows that we can detect layers of different dielectric parameters. From reconstructed image, we are partially able to reconstruct the shape and position of the simulated inhomogeneity (heat wave). From this simulation we establish the maximum distance between antennas and inhomogeneity for the

inhomogeneity detection. For head and neck this distance is 10 cm and is limited due to the attenuation in tissues. For real measurements scenarios, this distance will be lower.

To approach to the real measurement, the heterogeneous numerical phantom of real patient of large tumor was implemented. According to the results, the maximum reconstructed signal intensity was detected in the position of tumor, but the reconstructed signal intensity is spread in surrounding area, where the temperature increase did not occur. The way how to improve the chance for more accurate differential temperature reconstruction is to set the higher number of antennas closer to the heated area utilization and to correct the signal due to its attenuation. The transmission coefficient between antennas was about – 70 dB (reflection from heated tumor). According to the results gained from the simulation of the 3D real patient we concluded that the heat wave (first heated layers) can be detected.

7 Chapter: Measurement of Transmission between Hyperthermia Waveguide Applicator and UWB Antennas

7.1 Introduction

We performed measurement of transmission between waveguide hyperthermia applicator and UWB bowtie antennas (loan from TU Ilmenau). We used a 4-port VNA R&S ZVA vector analyser for frequencies up to 68 GHz. All measurements were carried out on agar phantom which we are using for most of our hyperthermia measurements. Its relative permittivity is 60 while conductivity being 0.8 S/m (for 434 MHz).

7.2 Used hyperthermia waveguide applicator

For the measurement purposes the waveguide applicator with a stripline horn aperture working on 434 MHz was used (part of proposed applicator system for head and neck region further described in chapter 3.5.3). The impedance matching ($|S_{11}|$) of this waveguide applicator to an agar phantom can be seen in the Fig. 7.1.

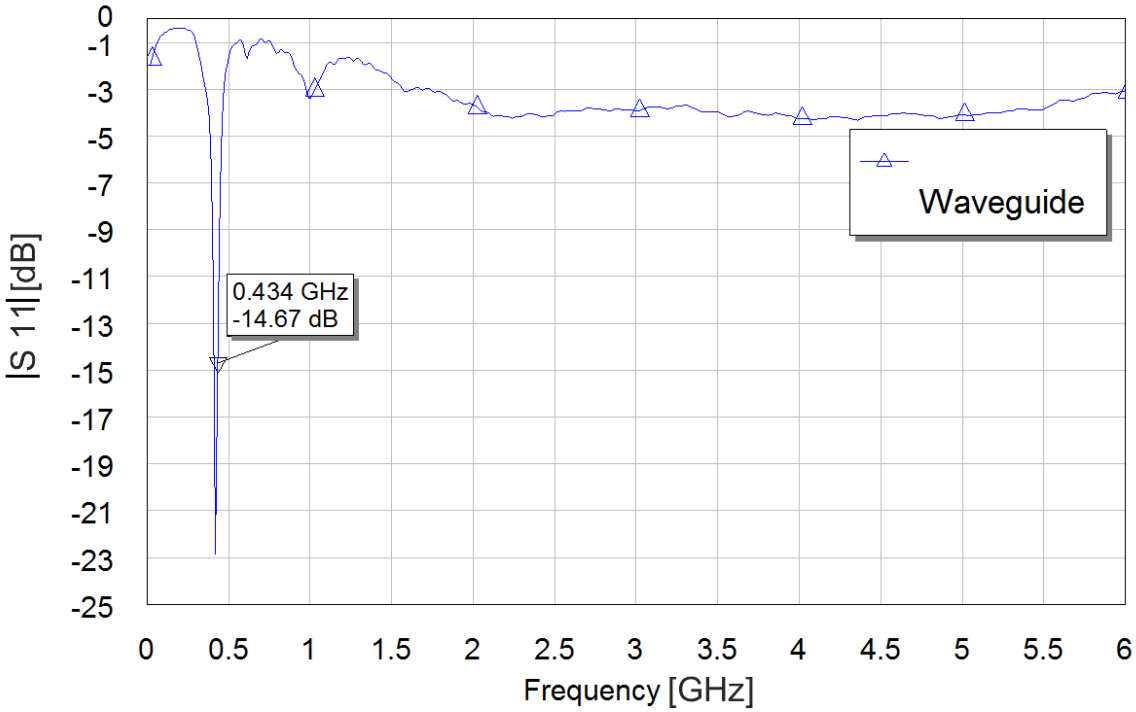

Fig. 7.1 Measured reflection coefficient of waveguide applicator in the measured frequency band.

7.3 Tested UWB antennas

We selected six passive UWB antennas suitable for the possible usage in the head and neck region. The active antennas are not usable, because in case of heating the whole spectrum is decreasing and the differential amplifier in the antennas is heated. This is causing extreme amplitude drift which is unpredictable. The antennas differ in size and by the type of substrate. All UWB antennas can be seen in the Fig. 7.2. They are differentially fed.

7.3.1 Differential feeding of UWB antennas

For verification of the correctness results of the differential antenna feeding we used three methods.

1) Modal decomposition in MATLAB
2) Analysis in Microwave studio (AWR): 180° hybrid
3) True differential mode (VNA)

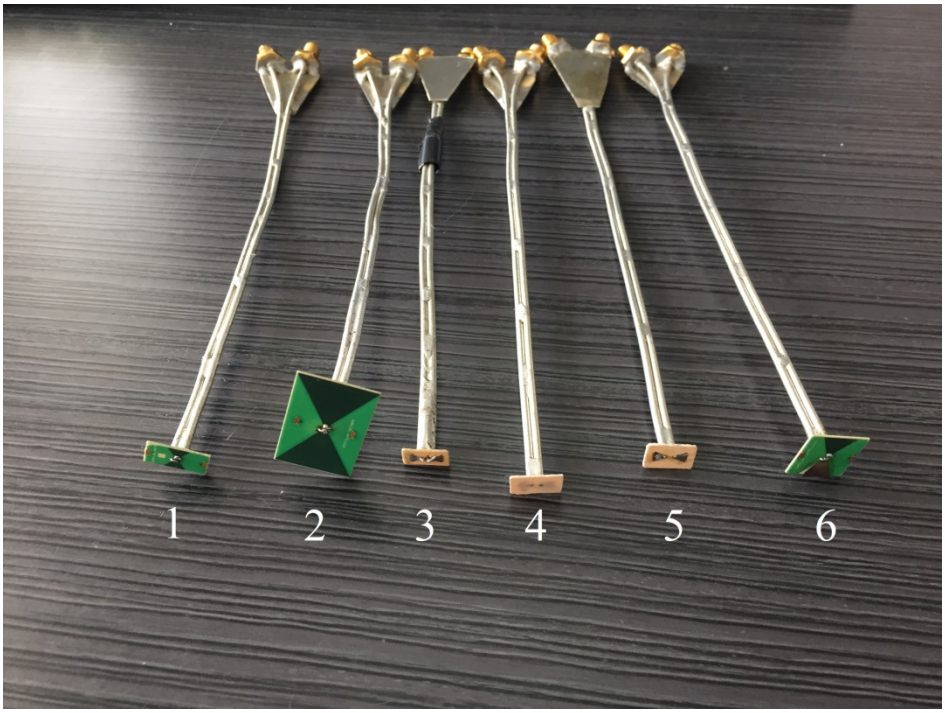

Fig. 7.2 Used UWB passive antennas of the differential feeding.

7.3.2 Antenna positioning and polarization

The measurement was performed for two mutual positions of applicator and UWB antennas. UWB antennas have always vertical polarization.

Pol_1 = copolar polarization, Pol_2 = orthogonal polarization. Pos_1 = waveguide against UWB antenna, Pos_2 = waveguide beside UWB antenna. The measurement setups are visible in the Fig. 7.3.

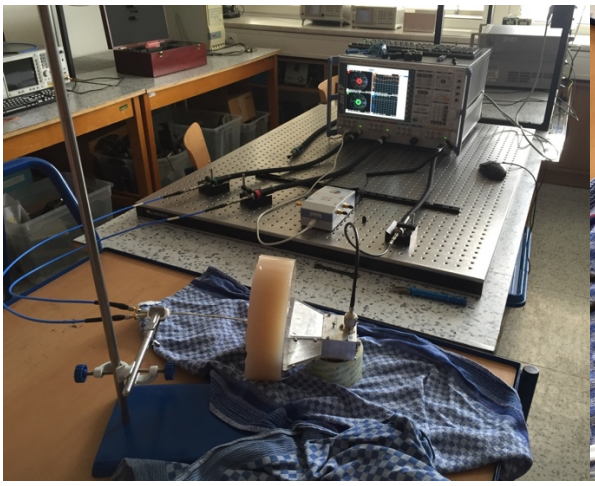

Pol1_Pos1

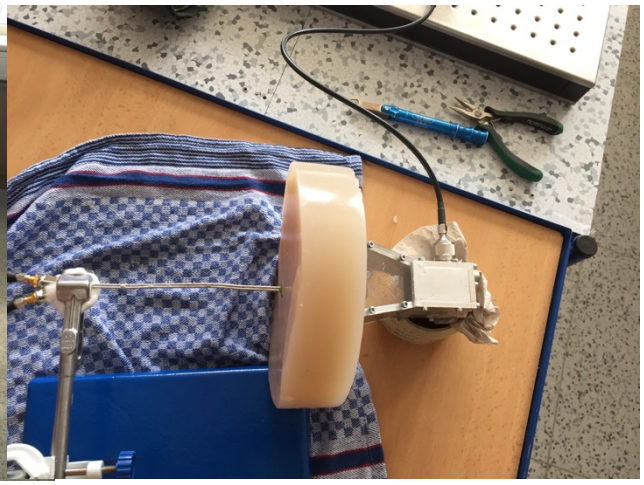

Pol2_Pos1

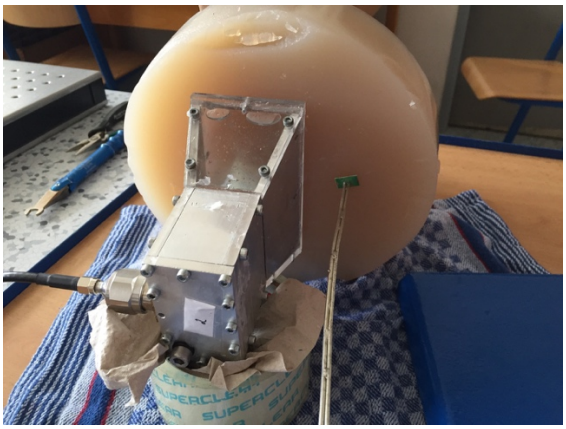

Pol2_Pos2

Fig. 7.3 Measurement setup of different polarisation (Pol) and position (Pos) of applicator and UWB antennas.

7.4 Results

We found that the most suitable antennas for hyperthermia/radar combination are antennas 4 and 5 from the transmission graphs in the Fig. 7.4 according to our measurement where the lowest transmission respectively reflection was found. According to our previous measurements with the passive antennas, the antenna number 6 achieved very good results in case of temperature measurements. We also performed a test of antenna's heating under 100 W. The temperature of antennas did not increase as in case of active antennas.

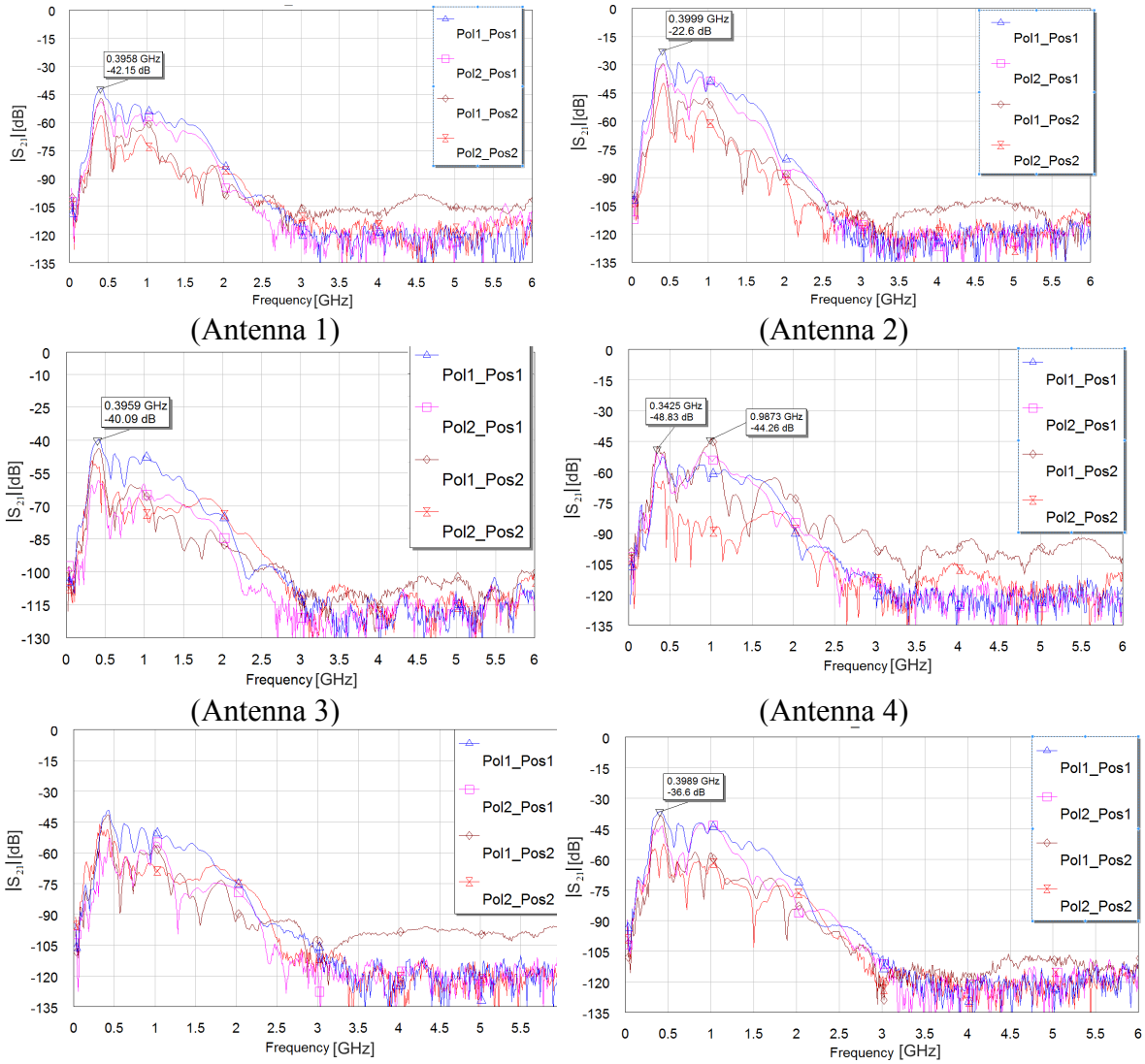

Fig. 7.4 Transmission between waveguide applicator and various UWB antennas labelled according to the Fig. 7.3. Polarisation is labelled “Pol” and position “Pos”.

8 Thesis Conclusion

In this chapter I would like to conclude and summarize the main results described in my dissertation thesis - which I consider to be my own "dissertable" contributions to here discussed topics. It consists from three main closely interconnected parts:

1. Microwave hyperthermia in head and neck region with definition of the main procedure for the effective multi-aperture applicator.
2. The research of a proposal utilization of new non-invasive temperature change detection system based on UWB radars in microwave hyperthermia.
3. Combinations of the microwave hyperthermia system and non-invasive differential temperature change detection system with the aim to verify possibility of hyperthermia treatment control by aid of UWB radars.

1) New applicator system for microwave hyperthermia for head and neck tumor treatment

In this part, the proposal of the new applicator system for microwave hyperthermia of head and neck tumor treatment is presented. The applicator system is optimized in order to achieve the best effectivity with the clinically used optimizer. We carried out a parametrical numerical study of the microwave energy focusing at 434 MHz to the point of target. The various applicators setups were investigated. The applicator system is composed of water filled waveguide applicator with strip line horn aperture. We generally formulated the main steps of the applicator system design including detailed applicator system requirements. For the gained results evaluation of two parameters were proposed. The first parameter is related to the absorbed energy (*SAR*) referred as SAR_{25}. The second parameter, T_{41} is related to the temperature distribution.

The proposal and optimization process of our applicator system is divided into six parts which we call "Studies". The Study I and II deals with the comparison of the *SAR* coverage of optimized and non-optimized EM fields. The EM field steering is performed through the amplitude and phase settings of each applicator. The best results were achieved for the setup with four applicators. The results were compared through the parameter SAR_{25}.

In our Study III the position optimization of microwave hyperthermia applicator system for deeply placed tumors treatment in head and neck area was performed. We tested the influence of the applicators polarization against the patient's body with the observation of the homogeneity of the EM field distribution. The aim of the second part of the Study III

was to observe the influence of the distance between the applicator system and patients surface. According to both evaluation parameters (SAR_{25} and T_{41}) the best result was achieved by the distance of 55 mm.

In Studies I-III the final setup of the applicator system was proposed. In the Study IV the applicator system robustness was numerically tested. The system robustness is important to take into account its clinical usability. In microwave hyperthermia treatment the temperature of the water bolus is in the temperature range from 15 °C to 40 °C. We concluded through the change of the water bolus temperature the resonance frequency of the applicator system is shifted by +/- 5MHz at maximum.

In the Study VI, the influence of the neck dimensions on the reflection coefficient and the *SAR* coverage of the selected target in the simplified neck phantom are analysed.
Finally, we constructed our first prototype of the hyperthermia system for head and neck treatment. We performed couple of measurements (as reflection coefficient measurement, *SAR* and temperature distribution after short time of heating). We observed very good agreement between simulation results and the results from real measurement. According to our results we concluded that the proposed applicators system constructed by four waveguide applicators has a very high treatment effectivity.

2) Non-invasive temperature monitoring using UWB radar

The second part of my thesis is focused on the non-invasive temperature monitoring, this novel approach of temperature monitoring using UWB radar was proposed and investigated by us. Based on mathematics and physics we derived basis for this - an original equation for monitoring of non-invasive change in temperature in the human body by the UWB radar using. This relation expresses the mathematical description of the radar signal reflection from the areas where the temperature is continually changing and thus the complex permittivity at given distances is changing as well.

Using the Ellison model of the temperature dependence of water complex permittivity (in microwave band), we estimated the temperature dependence of complex permittivity of the used phantom (agar phantom). These estimated trends of relative permittivity and specific conductivity were confirmed by real measurements on the prepared agar phantom while high correlation between estimation and measurement was acknowledged.

We derived a simplified Mason graph of layered medium based on the layered (very thin layers) temperature distribution. We implemented the algorithm into the MATLAB program environment for one-dimension temperature distribution case. We performed numerical studies containing also determination of the effective frequency bandwidth of UWB signal for one reflection from different distances from antennas in human muscle. In another numerical analysis we focused on the study of reflected signal amplitude dependence on the temperature difference between layers for the whole frequency spectrum. We conclude that the expected relationship between reflected signal intensity and temperature change is of a linear character. All assumptions were verified by several experiments with a real UWB radar system (in cooperation with TU Ilmenau, Germany). Various experiments were performed with the optimization of signal processing procedures which improves the detectability of the very low signal reflection from heated tissue. We carried out a feasibility studies of the possibility of detection temperature changes in reflected signal. We designed sophisticated experiments with different local heaters for bi-static and multi-static radar measurements. Based on the results the linear relationship between the reflected signal intensity and the temperature change was confirmed.

To show the potential of the temperature change detection the method using UWB MIMO M-sequence radar was used. We prepared the experiment using a hemispherical antennal array containing 24 active antennas arranged in the breast shape. We reconstructed the received signals using Delay and Sum algorithm. The reconstructed image was correlated with the expected temperature distribution. The resulting images suffered from the artefacts due to the low number of antennas.

3) Combinations of the microwave hyperthermia system and non-invasive differential temperature change detection system

In this part of my doctoral thesis we investigated a combination of two proposed systems mentioned above. We proposed possible treatment setup which consists of the hyperthermia system and 8 UWB bowtie antennas attached to the patient body. We numerically proved that it is possible to detect the changes in temperature in the treated area up to distance 7 cm from antennas by UWB radar. In the second part we performed measurement of the transmission between waveguide applicator and UWB antennas intended for the radar measurements in human body. From our investigation it is obvious that the active antennas are impropriate for this kind of application (because of the saturation

of the amplifier). But the passive antennas are suitable for this measurement. The 434 MHz frequency is easy to filter from the signals but the problem is the drift effect caused by non-predictable heating of antennas and the system.

According to the obtained results the greatest benefits of this doctoral thesis is the proposal of an original applicator system which is able to efficiently and selectively heat the tumor in the head and neck region. The second benefit of this thesis, closely to the first one, is the development and investigation of the new method of non-invasive monitoring of temperature change during hyperthermia treatment by using UWB radar. We proved that the UWB radar is able to detect temperature changes in the tissue. According to the numerical simulation results we demonstrated that this method is of sufficient spatial and temperature resolution. Our method also benefits among other methods of temperature monitoring systems used in microwave hyperthermia. The vast majority results of this thesis were presented in several international conferences (e.g. European Microwave Week, EuCAP, PIERS and ESHO), the resulting hyperthermia system for head and neck cancer treatment was published in the journal with impact factor as well as our contribution of the non-invasive temperature change detection is under review at the moment in the journal with impact factor.

In the future I would recommend to develop advanced algorithms to find temperature changes in patient's tissue through equation solving (to find $\vartheta'(x)$ in equation 4.8). First algorithm was developed by me and successfully tested but the optimization is needed. This would be a good topic for diploma student of mathematics. Of course, the development of the optimal antenna placement for hyperthermia or for temperature change measurement should continue and must be tested by computer simulations and/or by actual measurement. The next step could be applicator setup rearrangements for heating of brain tumors which is very challenging area. I recommend performing temperature change profile measurement on animals and slowly to put it into practice respecting all safety rules.

In my opinion my doctoral thesis fulfilled the main goals. Initially there was my own research inspired by the COST Action TD1301: "Development of a European-based Collaborative Network to Accelerate Technological and Clinical in the Area of Medical Microwave Imaging". Major part of the research work within this dissertation thesis has been done in the frame of the research projects granted from the Czech Science Foundation, number 17-20498J: "Non-invasive temperature estimation inside of human body based on physical aspects of ultra-wideband microwave channel" and the German Science Foundation

(DFG) in the project HE 6015/2-1. In part it was supported by CTU grant SGS17/182/OHK3/3T/13, too.

The idea of combination of the hyperthermia system and UWB radar system for differential temperature measurement was presented in the program of PIERS 2017 in St. Petersburg. Committee of the Best Student Paper Contest decided to award my presentation by the Second Prize of this contest.

References

[1] A. Chicheł, J. Skowronek, M. Kubaszewska, and M. Kanikowski, "Hyperthermia – description of a method and a review of clinical applications," *Reports Pract. Oncol. Radiother.*, vol. 12, no. 5, pp. 267–275, Sep. 2007.

[2] Vrba J., Medical Applications of Microwave Technique. Press CTU in Prague, 2003.

[3] A. Boag, Y. Leviatan, and A. Boag, "Analysis and optimization of waveguide multiapplicator hyperthermia systems," IEEE Transactions on Biomedical Engineering, vol. 40, no. 9, pp. 946-952, 1993.

[4] M. M. Paulides *et al.*, "Laboratory prototype for experimental validation of MR-guided radiofrequency head and neck hyperthermia," *Phys. Med. Biol.*, vol. 59, no. 9, pp. 2139–2154, May 2014.

[5] M. R. Horsman, "Tissue physiology and the response to heat," *International Journal of Hyperthermia*, vol. 22, no. 3, pp. 197–203, May 2006.

[6] R. Valdagni, F.-F. Liu, and D. S. Kapp, "Important prognostic factors influencing outcome of combined radiation and hyperthermia," Int. J. Radiat. Oncol., vol. 15, no. 4, pp. 959–972, Oct. 1988.

[7] R. Valdagni and M. Amichetti, "Report of long-term follow-up in a randomized trial comparing radiation therapy and radiation therapy plus hyperthermia to metastatic lymphnodes in stage IV head and neck patients," International Journal of Radiation Oncology*Biology*Physics, vol. 28, no. 1, pp. 163–169, Jan. 1994.

[8] C. Vernon, J. Hand, S. Field, D. Machin, J. Whaley, J. Zee, W. Vanputten, G. Vanrhoon, and J. Vandijk, "Radiotherapy with or without hyperthermia in the treatment of superficial localized breast cancer: Results from five randomized controlled trials," International Journal of Radiation OncologyBiologyPhysics, vol. 35, no. 4, pp. 731–744, Jul. 1996.

[9] J. van der Zee, D. Gonzalez Gonzalez, G. C. van Rhoon, J. D. P. van Dijk, W. L. J. van Putten, and A. A. M. Hart, "Comparison of radiotherapy alone with radiotherapy plus hyperthermia in locally advanced pelvic tumours: a prospective, randomised, multicentre trial," Lancet, vol. 355, no. 9210, p. 1119, 4/1/2000 2000.

[10] V. Milani and M. R. Horsman, "Cellular and vascular effects of hyperthermia," International Journal of Hyperthermia, vol. 24, no. 1, pp. 1–2, Feb. 2008.

[11] J. Kubes, "Immodulation effects of the hyperthermia in cancer treatment", Doctoral Thesis, Charles University in Prague, 2007.

[12] P. Srivastava, "INTERACTION OF HEAT SHOCK PROTEINS WITH PEPTIDES AND ANTIGEN PRESENTING CELLS : Chaperoning of the Innate and Adaptive Immune Responses," *Annu. Rev. Immunol.*, vol. 20, no. 1, pp. 395–425, Apr. 2002.

[13] R. Hesketh, *Introduction to Cancer Biology*. Cambridge: Cambridge University Press, 2012.

[14] M. H. Falk and R. D. Issels, "Hyperthermia in oncology.," *Int. J. Hyperthermia*, vol. 17, no. 1, pp. 1–18.

[15] G. M. Hahn, "Metabolic aspects of the role of hyperthermia im mammalian cell inactivation and their possible relevance to cancer treatment.," *Cancer Res.*, vol. 34, no. 11, pp. 3117–23, Nov. 1974.

[16] J. J. Skitzki, E. A. Repasky, and S. S. Evans, "Hyperthermia as an immunotherapy strategy for cancer.," *Curr. Opin. Investig. Drugs*, vol. 10, no. 6, pp. 550–8, Jun. 2009.

[17] R. W. Y. Habash, R. Bansal, D. Krewski, and H. T. Alhafid, "Thermal therapy, part 2: hyperthermia techniques.," *Crit. Rev. Biomed. Eng.*, vol. 34, no. 6, pp. 491–542, 2006.

[18] R. Issels, E. Kampmann, R. Kanaar and L. H. Lindner, "Hallmarks of hyperthermia in driving the future of clinical hyperthermia as targeted therapy: translation into clinical application", Int J Hyperthermia. 2016 January, 32:1, pp. 89-95.

[19] B. Thiesen and A. Jordan, "Clinical applications of magnetic nanoparticles for hyperthermia," *International Journal of Hyperthermia*, vol. 24, no. 6, pp. 467–474, Sep. 2008.

[20] A. Argiris, M. V. Karamouzis, D. Raben, and R. L. Ferris, "Head and neck cancer," The Lancet, vol. 371, no. 9625, pp. 1695–1709, May 2008.

[21] J. van der Zee, D. González, G. C. van Rhoon, J. D. van Dijk, W. L. van Putten, and A. A. Hart, "Comparison of radiotherapy alone with radiotherapy plus hyperthermia in locally advanced pelvic tumours: a prospective, randomised, multicentre trial," The Lancet, vol. 355, no. 9210, pp. 1119–1125, Apr. 2000.

[22] Christ A, Kainz W, Hahn E G, Honegger K, Zefferer M, Neufeld E, Rascher W, Janka R, Bautz W, Chen J, Kiefer B, Schmitt P, Hollenbach H P, Shen J, Oberle M, Szczerba D, Kam A, Guag J W, and Kuster N, "The Virtual Family - development of surface-based anatomical models of two adults and two children for dosimetric simulations, Physics in Medicine and Biology, " 55(2): N23-N38, 2010.

[23] G. Arcangeli et al., "Effectiveness of microwave hyperthermia combined with ionizing radiation: Clinical results on neck node metastasest," Int. J. Radiat. Oncol., vol. 6, no. 2, pp. 143–148, Feb. 1980.

[24] R. Valdagni et al., "Radical radiation alone versus radical radiation plus microwave hyperthermia for N3 (TNM-UICC) neck nodes: a prospective randomized clinical trial.," Int. J. Radiat. Oncol. Biol. Phys., vol. 15, no. 1, pp. 13–24, Jul. 1988.

[25] R. Valdagni and M. Amichetti, "Report of long-term follow-up in a randomized trial comparing radiation therapy and radiation therapy plus hyperthermia to metastatic lymph nodes in stage IV head and neck patients.," Int. J. Radiat. Oncol. Biol. Phys., vol. 28, no. 1, pp. 163–9, Jan. 1994.

[26] N. G. Huilgol, S. Gupta, and C. R. Sridhar, "Hyperthermia with radiation in the treatment of locally advanced head and neck cancer: a report of randomized trial.," J. Cancer Res. Ther., vol. 6, no. 4, pp. 492–6, 2010.

[27] Y. Hua, S. Ma, Z. Fu, Q. Hu, L. Wang, and Y. Piao, "Intracavity hyperthermia in nasopharyngeal cancer: A phase III clinical study," Int. J. Hyperth., vol. 27, no. 2, pp. 180–186, Mar. 2011.

[28] C. Zhao, J. Chen, B. Yu, and X. Chen, "Improvement in quality of life in patients with nasopharyngeal carcinoma treated with non-invasive extracorporeal radiofrequency in combination with chemoradiotherapy," Int. J. Radiat. Biol., vol. 90, no. 10, pp. 853–858, Oct. 2014.

[29] M. Amichetti et al., "Hyperfractionated radiation in combination with local hyperthermia in the treatment of advanced squamous cell carcinoma of the head and neck: a phase I–II study," Radiother. Oncol., vol. 45, no. 2, pp. 155–158, Nov. 1997.

[30] M. M. Paulides, J. F. Bakker, E. Neufeld, J. van der Zee, P. P. Jansen, P. C. Levendag, and G. C. van Rhoon, "The HYPERcollar: A novel applicator for hyperthermia in the head and neck.," *International Journal of Hyperthermia*, vol. 23, no. 7, pp. 567–576, Nov. 2007.

[31] P. Togni, Z. Rijnen, W. C. M. Numan, R. F. Verhaart, J. F. Bakker, G. C. van Rhoon, and M. M. Paulides, "Electromagnetic redesign of the HYPERcollar applicator: toward improved deep local head-and-neck hyperthermia," *Physics in Medicine and Biology*, vol. 58, no. 17, pp. 5997–6009, Sep. 2013.

[32] M. M. Paulides, W. C. M. Numan, T. Drizdal, G. Kotek, D. T. B. Yeo, and G. C. van Rhoon, "Feasibility of MRI-guided hyperthermia treatment of head and neck cancer,"

in *2014 8th European Conference on Antennas and Propagation (EuCAP)*, 2014, pp. 1474–1477.

[33] H. D. Trefna, P. Togni, R. Shiee, J. Vrba, and M. Persson, "Design of a wideband multi-channel system for time reversal hyperthermia," *International Journal of Hyperthermia*, vol. 28, no. 2, pp. 175–183, Mar. 2012.

[34] H. D. Trefna, J. Vrba, and M. Persson, "Time-reversal focusing in microwave hyperthermia for deep-seated tumors," Physics in Medicine and Biology, vol. 55, no. 8, pp. 2167–2185, Apr. 2010.

[35] H. D. Trefna, J. Vrba, and M. Persson, "Evaluation of a patch antenna applicator for time reversal hyperthemia," Int. J. Hyperthermia, vol. 26, no. 2, pp. 185–197, 2010.

[36] M. M. Paulides, "Development of a clinical head and neck hyperthermia applicator, " Proefschrift Erasmus Universiteit Rotterdam, 2007.

[37] Z. Rijnen, J. F. Bakker, R. A. M. Canters, P. Togni, G. M. Verduijn, P. C. Levendag, G. C. Van Rhoon, and M. M. Paulides, "Clinical integration of software tool VEDO for adaptive and quantitative application of phased array hyperthermia in the head and neck," *International Journal of Hyperthermia*, vol. 29, no. 3, pp. 181–193, May 2013.

[38] H. P. Kok, S. Ciampa, R. de Kroon-Oldenhof, E. J. Steggerda-Carvalho, G. van Stam, P. J. Zum Vörde Sive Vörding, L. J. A. Stalpers, E. D. Geijsen, F. Bardati, A. Bel, and J. Crezee, "Toward Online Adaptive Hyperthermia Treatment Planning: Correlation Between Measured and Simulated Specific Absorption Rate Changes Caused by Phase Steering in Patients," *International Journal of Radiation Oncology*Biology*Physics*, vol. 90, no. 2, pp. 438–445, Oct. 2014.

[39] SPEAG AG, SEMCAD X Reference Guide. [Online]. Available:http://download.speag.com/releases/semcad/1485/documentation/SEMCAD-X-Manual.pdf

[40] C. Boutelier, L. Bougues, and J. Timbal, "Experimental study of convective heat transfer coefficient for the human body in water," J Appl Physiol Respir Environ Exerc Physiol, vol. 42, no. 1, pp. 93-100, Jan. 1977.

[41] M. M. Paulides, D. H. M. Wielheesen, J. Van Der Zee, and G. C. Van Rhoon, "Assessment of the local SAR distortion by major anatomical structures in a cylindrical neck phantom," Int. J. Hyperth., vol. 21, no. 2, pp. 125–140, Mar. 2005.

[42] M. M. Paulides, S. H. J. A. Vossen, A. P. M. Zwamborn, and G. C. van Rhoon, "Theoretical investigation into the feasibility to deposit RF energy centrally in the head-and-neck region," Int. J. Radiat. Oncol., vol. 63, no. 2, pp. 634–642, Oct. 2005.

[43] B. Vrbova and J. Vrba, "Microwave Thermotherapy in Cancer Treatment: Evaluation of Homogeneity," *Prog. Electromagn. Res.*, vol. 129, pp. 181–195, 2012.

[44] O. Fiser, J. Vrba, „Oriented Array of Waveguide Applicators for Local Thermotherapy", in 8th European Conference on Antennas and Propagation, 2014. EuCAP 2014, 2014, pp. 2169-2172, 2014

[45] O. Fiser, I. Merunka, L. Vojáčková, J. Vrba, Utilization of Waveguide Applicators Combination for Electromagntic Field Focusing, In 24th International Conference Radioelektronika 2014. Bratislava: Slovak University of Technology, 2014.

[46] O. Fiser, I. Merunka, L. Vojackova, J. Vrba, „Space Distribution of SAR and Temperature in Human Model with Tumor Using Waveguide Applicator Array, In European Microwave Week 2014 Conference Proceedings. London: Horizon House Publications, 2014, p. 484-487, 2014.

[47] P. Hasgall, E. Neufeld, M. Gosselin, A. Klingenböck, and N. Kuster. (2011) IT'IS database for thermal and electromagnetic parameters of biological tissues. [Online]. Available: www.itis.ethz.ch/database.

[48] J. Vrba, B. Vrbova, J. Vrba, and D. Vrba, 'Microwave thermotherapy: Study of hot-spots induced by electromagnetic surface waves', in *2013 7th European Conference on Antennas and Propagation (EuCAP)*, 2013, pp. 3125–3126.

[49] B. Vrbova, P. Novakova, M. Halfarova, J. Vrba, „Planning of head and neck tumours treatment", in 29th Annual Meeting of the European Society for Hypertermic Oncology, 2014. ESHO 2014, 2014, pp. 32-33

[50] O. Fiser, I. Merunka, L. Vojackova, J. Vrba, „Space Distribution of SAR and Temperature in Human Model with Tumor Using Waveguide Applicator Array, In European Microwave Week 2014 Conference Proceedings. London: Horizon House Publications, 2014, p. 484-487, 2014.

[51] R. Zajicek, L. Oppl, J. Vrba, "Broadband measurement of complex permittivity using reflection method and coaxial probes", Radioengineering, vol. 17, pp 14-19, 2008.

[52] M. M. Paulides, J. F. Bakker, M. Linthorst, J. van der Zee, Z. Rijnen, E. Neufeld, P. M. T. Pattynama, P. P. Jansen, P. C. Levendag, and G. C. van Rhoon, "The clinical

feasibility of deep hyperthermia treatment in the head and neck: new challenges for positioning and temperature measurement," Physics in Medicine and Biology, vol. 55, no. 9, pp. 2465–2480, May 2010.

[53] E. Schena, D. Tosi, P. Saccomandi, E. Lewis, and T. Kim, "Fiber Optic Sensors for Temperature Monitoring during Thermal Treatments: An Overview," Sensors (Basel), vol. 16, no. 7, Jul. 2016.

[54] M. D. Sherar *et al.*, "Beam shaping for microwave waveguide hyperthermia applicators," *Int. J. Radiat. Oncol.*, vol. 25, no. 5, pp. 849–857, Apr. 1993.

[55] P. M. A. van Haaren, H. P. Kok, P. J. Zum Vörde Sive Vörding, J. D. P. van Dijk, M. C. C. M. Hulshof, P. Fockens, J. J. B. van Lanschot, and J. Crezee, "Reliability of temperature and SAR measurements at oesophageal tumour locations," International Journal of Hyperthermia, vol. 22, no.7, pp. 545–561, Nov. 2006.

[56] H. P. Kok, C. A. T. V. den Berg, P. M. A. V. Haaren, and J. Crezee, "Artefacts in intracavitary temperature measurements during regional hyperthermia," Physics in Medicine and Biology, vol. 52, no. 17, pp. 5157–5171, Sep. 2007.

[57] L. Frich, "Non-invasive thermometry for monitoring hepatic radiofrequency ablation," Minim. Invasive Ther. Allied Technol., vol. 15, no. 1, pp. 18–25, Jan. 2006.

[58] W. Wlodarczyk, M. Hentschel, P. Wust, R. Noeske, N. Hosten, H. Rinneberg, and R. Felix, "Comparison of four magnetic resonance methods for mapping small temperature changes," Phys Med Biol, vol. 44, no. 2, pp. 607–624, Feb. 1999.

[59] L. Lüdemann, W. Wlodarczyk, J. Nadobny, M. Weihrauch, J. Gellermann, and P. Wust, "Noninvasive magnetic resonance thermography during regional hyperthermia," International Journal of Hyperthermia, vol. 26, no. 3, pp. 273–282, May 2010.

[60] Ø. Klemetsen and S. Jacobsen, "Improved Radiometric Performance Attained by an Elliptical Microwave Antenna With Suction," IEEE Transactions on Biomedical Engineering, vol. 59, no. 1, pp. 263–271, Jan. 2012.

[61] L. Dubois, J.-P. Sozanski, V. Tessier, J.-C. Camart, J.-J. Fabre, J. Pribetich, and M. Chive, "Temperature control and thermal dosimetry by microwave radiometry in hyperthermia," IEEE Transactions on Microwave Theory and Techniques, vol. 44, no. 10, pp. 1755–1761, Oct. 1996.

[62] K. T. Karathanasis, I. A. Gouzouasis, I. S. Karanasiou, and N. K. Uzunoglu, "Experimental Study of a Hybrid Microwave Radiometry-Hyperthermia Apparatus

With the Use of an Anatomical Head Phantom," IEEE Transactions on Information Technology in Biomedicine, vol. 16, no. 2, pp. 241–247, Mar. 2012.

[63] R. M. Arthur, W. L. Straube, J. W. Trobaugh, and E. G. Moros, "Non-invasive estimation of hyperthermia temperatures with ultrasound," International Journal of Hyperthermia, vol. 21, no. 6, pp. 589–600, Sep. 2005.

[64] S. Ueno, M. Hashimoto, H. Fukukita, and T. Yano, "Ultrasound thermometry in hyperthermia," in Ultrasonics Symposium, 1990. Proceedings., IEEE 1990, 1990, pp. 1645–1652 vol.3.

[65] P. M. Meaney, T. Zhou, M. W. Fanning, S. D. Geimer, and K. D. Paulsen, "Microwave thermal imaging of scanned focused ultrasound heating: Phantom results," Int. J. Hyperth., vol. 24, no. 7, pp. 523–536, Jan. 2008.

[66] P. M. Meaney, K. D. Paulsen, M. W. Fanning, D. Li, and Q. Fang, "Image accuracy improvements in microwave tomographic thermometry: phantom experience," Int. J. Hyperth., vol. 19, no. 5, pp. 534–550, Jan. 2003.

[67] P. M. Meaney et al., "Microwave thermal imaging: initial in vivo experience with a single heating zone," Int. J. Hyperthermia, vol. 19, no. 6, pp. 617–41.

[68] M. Haynes, J. Stang, and M. Moghaddam, "Real-time Microwave Imaging of Differential Temperature for Thermal Therapy Monitoring," IEEE Transactions on Biomedical Engineering, vol. 61, no. 6, pp. 1787–1797, Jun. 2014.

[69] M. Miyakawa, "Tomographic measurement of temperature change in phantoms of the human body by chirp radar-type microwave computed tomography," Med Biol Eng Comput, vol. 31 Suppl, no. S1, pp. S31-6, Jul. 1993.

[70] M. Bertero, M. Miyakawa, P. Boccacci, F. Conte, K. Orikasa, and M. Furutani, "Image restoration in chirp-pulse microwave CT (CP-MCT)," IEEE Trans. Biomed. Eng., vol. 47, no. 5, pp. 690–699, May 2000.

[71] J.-C. Bolomey, C. Durix, and D. Lesselier, "Determination of conductivity profiles by time-domain reflectometry," IEEE Trans. Antennas Propag., vol. 27, no. 2, pp. 244–248, Mar. 1979.

[72] N. Petrovic, MEASUREMENT SYSTEM FOR MICROWAVE IMAGING TOWARDS A BIOMEDICAL APPLICATION, Doctoral thesis, Marlandan University, Sweden, 2014.

[73] S. Noghanian, A. Sabouni, T. Desell, and A. Ashtari, Microwave Tomography. New York, NY: Springer New York, 2014.

[74] D. Byrne, M. O'Halloran, E. Jones, and M. Glavin, "A comparison of data-independent microwave beamforming algorithms for the early detection of breast cancer," in *Engineering in Medicine and Biology Society, 2009. EMBC 2009. Annual International Conference of the IEEE*, 2009, pp. 2731–2734.

[75] R. Nilavalan, A. Gbedemah, I. J. Craddock, X. Li, and S. C. Hagness, "Numerical investigation of breast tumour detection using," *Electronics Letters*, vol. 39, no. 25, pp. 1787–1789, Dec. 2003.

[76] Hooi Been Lim, Nguyen Thi Tuyet Nhung, Er-Ping Li, and Nguyen Duc Thang, "Confocal Microwave Imaging for Breast Cancer Detection: Delay-Multiply-and-Sum Image Reconstruction Algorithm," *IEEE Transactions on Biomedical Engineering*, vol. 55, no. 6, pp. 1697–1704, Jun. 2008.

[77] A. Shahzad, M. O'Halloran, E. Jones, and M. Glavin, "A PREPROCESSING FILTER FOR MULTISTATIC MICROWAVE BREAST IMAGING FOR ENHANCED TUMOUR DETECTION," *Progress In Electromagnetics Research B*, vol. 57, pp. 115–126, 2014.

[78] E. J. Bond, X. Li, S. C. Hagness, and B. D. Van Veen, "Microwave imaging via space-time beamforming for early detection of breast cancer," *IEEE Transactions on Antennas and Propagation*, vol. 51, no. 8, pp. 1690–1705, Aug. 2003.

[79] Y. Xie, B. Guo, L. Xu, J. Li, and P. Stoica, "Multistatic Adaptive Microwave Imaging for Early Breast Cancer Detection," *IEEE Transactions on Biomedical Engineering*, vol. 53, no. 8, pp. 1647–1657, Aug. 2006.

[80] E. C. Fear, P. M. Meaney, and M. A. Stuchly, "Microwaves for breast cancer detection?," *IEEE Potentials*, vol. 22, no. 1, pp. 12–18, Feb. 2003.

[81] A. J. Surowiec, S. S. Stuchly, J. R. Barr, and A. Swarup, "Dielectric properties of breast carcinoma and the surrounding tissues," *IEEE Transactions on Biomedical Engineering*, vol. 35, no. 4, pp. 257–263, Apr. 1988.

[82] A. M. Campbell and D. V. Land, "Dielectric properties of female human breast tissue measured in vitro at 3.2 GHz," *Physics in Medicine and Biology*, vol. 37, no. 1, pp. 193–210, Jan. 1992.

[83] M. Helbig, J. Sachs, F. Tansi, and I. Hilger, "Experimental feasibility study of contrast agent enhanced UWB breast imaging by means of M-sequence sensor systems," in *2014 8th European Conference on Antennas and Propagation (EuCAP)*, 2014, pp. 311–315.

[84] M. Klemm, D. Gibbins, J. Leendertz, T. Horseman, A. W. Preece, R. Benjamin, and I. J. Craddock, "Development and testing of a 60-element UWB conformal array for breast cancer imaging," in *Proceedings of the 5th European Conference on Antennas and Propagation (EUCAP)*, 2011, pp. 3077–3079.

[85] M. Klemm, I. Craddock, J. Leendertz, A. Preece, and R. Benjamin, "Experimental and clinical results of breast cancer detection using UWB microwave radar," in *IEEE Antennas and Propagation Society International Symposium, 2008. AP-S 2008*, 2008, pp. 1–4.

[86] J. Sachs, "*M-Sequence radar*", in D.J. Daniels ed., "*Ground Penetrating Radar*", 2nd edition, IEE Radar, Sonar, Navigation and Avionics Series 15, pp. 225-237, 2004.

[87] M. Helbig, I. Hilger, M. Kmec, G. Rimkus, and J. Sachs, "Experimental phantom trials for UWB breast cancer detection," in *Microwave Conference (GeMiC), 2012 The 7th German*, 2012, pp. 1–4.

[88] M. O'Halloran, M. Glavin, and E. Jones, "ROTATING ANTENNA MICROWAVE IMAGING SYSTEM FOR BREAST CANCER DETECTION," *Progress In Electromagnetics Research*, vol. 107, pp. 203–217, 2010.

[89] M. A. Elahi, A. Shahzad, M. Glavin, E. Jones, and M. O'Halloran, "Hybrid Artifact Removal for Confocal Microwave Breast Imaging," *IEEE Antennas and Wireless Propagation Letters*, vol. 13, pp. 149–152, 2014.

[90] N. R. Epstein, A. G. Golnabi, P. M. Meaney, and K. D. Paulsen, "Conformal microwave tomography using a broadband non-contacting monopole antenna array," in *2012 IEEE International Conference on Ultra-Wideband (ICUWB)*, 2012, pp. 192–196.

[91] M. Lazebnik, M. C. Converse, J. H. Booske, and S. C. Hagness, "Ultrawideband temperature-dependent dielectric properties of animal liver tissue in the microwave frequency range," Phys Med Biol, vol. 51, no. 7, pp. 1941–1955, Apr. 2006.

[92] W.J. Ellison, "Permittivity of pure water, at standard atmospheric pressure, ver the frequency range 0-25 THz and the temperature range 0-100 °C, "Journal of Physical and Chemical Reference Data, vol.36, no. 1, pp 1-18, 2007.

[93] M. Lazebnik, D. Popovic et al. "A large scale of the ultrawideband microwave dielectric properties of normal, benign and malignant breast tissues obtained from cancer surgeries," Physics in Medicine and Biology, vol. 52, pp. 6093–6115, 2007.

[94] H. Kato, M. Hiraoka, and T. Ishida, "An agar phantom for hyperthermia," Medical Physics, vol. 13, no. 3, pp. 396–398, May 1986.

[95] J. Sachs, “Handbook of Ultra-Wideband Short-Range Sensing: Theory, Sensors, Applications”, Wiley-VCH, Berlin, 2012.

[96] O. Fiser, M. Helbig, S. Ley, J. Sachs, and J. Vrba, “Feasibility study of temperature change detection in phantom using M-sequence radar,” in 2016 10th European Conference on Antennas and Propagation (EuCAP), 2016, pp. 1–4.

[97] M. Helbig, J. Sachs, F. Tansi, and I. Hilger, “Experimental feasibility study of contrast agent enhanced UWB breast imaging by means of M-sequence sensor systems,” in 2014 8th European Conference on Antennas and Propagation (EuCAP), 2014, pp. 311–315.

[98] M. Lazebnik, E. L. Madsen, G. R. Frank, and S. C. Hagness, “Tissue-mimicking phantom materials for narrowband and ultrawideband microwave applications,” Phys. Med. Biol., vol. 50, no. 18, p. 4245, 2005.

[99] J. Vrba, M. Lapeš, and L. Oppl, “Technical aspects of microwave thermotherapy,” Bioelectrochemistry and Bioenergetics, vol. 48, no. 2, pp. 305–309, May 1999.

[100] M. Helbig, M. Kmec, J. Sachs, C. Geyer, I. Hilger, and G. Rimkus, “Aspects of antenna array configuration for UWB breast imaging,” in 2012 6th European Conference on Antennas and Propagation (EUCAP), 2012, pp. 1737–1741.

[101] R. C. Conceição, J. J. Mohr, and M. O’Halloran, Eds., An Introduction to Microwave Imaging for Breast Cancer Detection. Cham: Springer International Publishing, 2016.

Author's Publications

Publications in journal with impact factors related to the thesis

- O. Fiser, I. Merunka, and J. Vrba, "Waveguide Applicator System for Head and Neck Hyperthermia Treatment", Journal of Electrical Engineering & Technology. 2016, 11(6), 1744-1753. ISSN 1975-0102.
- O. Fiser, M. Helbig, J. Sachs, S. Ley, I. Merunka and J. Vrba, "Microwave Non-invasive Temperature Monitoring using UWB Radar for Cancer Treatment by Hyperthermia", 2017, under review in journal Progress in Electromagnetic Research.

International conference contributions related to the thesis

In WoS

- O. Fiser, J. Vrba, "Space Distribution of SAR and Temperature in Human Body Model with Tumor Using Waveguide Applicator Array",in Microwave Conference (EuMC), 2014 44th European, 2014, pp. 484–487.
- O. Fiser, I. Merunka, L. Vojackova and J. Vrba, "Utilization of Waveguide Applicators Combination for Electromagnetic Field Focusing", In: 24th International Conference Radioelektronika 2014. Bratislava: Slovak University of Technology, 2014, ISBN978-1-4799-3713-4.
- O. Fiser, J. Vrba, "Oriented Array of Waveguide Applicators for Local Thermotherapy", in for 8th European Conference on Antennas and Propagation, 2014. EuCAP 2014, 2014, pp. 2169-2172
- O. Fiser, M. Helbig, S. Ley, J. Sachs, and J. Vrba, "Feasibility study of temperature change detection in phantom using M-sequence radar", in 2016 10th European Conference on Antennas and Propagation (EuCAP), 2016, pp. 1–4.

In Scopus and others

- O. Fiser, I. Merunka, and J. Vrba, "Hot Spots by Oncological Patients with Metal Implants in Head and Neck Region", in Progress in Electromagnetics Research Symposium in Prague. Cambridge: Electromagnetics Academy, 2015, pp. 2593-2597.

- O. Fiser, I. Merunka, and J. Vrba, "Microwave hyperthermia system for head and neck area with noninvasive UWB temperature change detection," in *2017 Progress In Electromagnetics Research Symposium - Spring (PIERS)*, 2017, pp. 1657–1662.
- O. Fiser, I. Merunka, and J. Vrba, "Optimization of microwave hyperthermia applicator system for deep placed tumors treatment in head and neck area," in *2017 Progress In Electromagnetics Research Symposium - Spring (PIERS)*, 2017, pp. 1733–1738.
- O. Fiser, I. Merunka, and J. Vrba, "Numerical feasibility study of new combined hyperthermia system for head and neck region," in *2017 47th European Microwave Conference (EuMC)*, 2017, pp. 719–722.

International conference contributions not related to the thesis

In WoS

- J. Moll, J. Vrba, I. Merunka, O. Fiser, and V. Krozer, "Non-invasive microwave lung water monitoring: Feasibility study", in 2015 9th European Conference on Antennas and Propagation (EuCAP), 2015, pp. 1–4.
- I. Merunka, O. Fiser, L. Vojackova, J. Vrba, D. Vrba, "Utilization Potential of Balanced Antipodal Vivaldi Antenna for Microwave Hyperthermia Treatment of Breast Cancer—, in 8th European Conference on Antennas and Propagation, 2014. EuCAP 2014, 2014, pp. 804-808
- I. Merunka, O. Fiser, L. Vojackova, J. Vrba, and D. Vrba, "Array of balanced antipodal Vivaldi antennas used for microwave hyperthermia treatment of neck cancer", in Radioelektronika (RADIOELEKTRONIKA), 2014 24th International Conference, 2014, pp. 1–4. (cited: 1)
- L. Vojácková, O. Fiser, I. Merunka and J. Vrba, "Thermoablation for breast cancer treatment using microwave interstitial helix applicators", in Microwave Conference (EuMC), 2014 44th European, 2014, pp. 794–797.
- I. Merunka, O. Fiser, L. Vojackova, J. Vrba, and D. Vrba, "Microwave hyperthermia treatment of neck cancer using eight UWB antennas", in Microwave Conference (EuMC), 2014 44th European, 2014, pp. 790–793.

In Scopus and others

- O. Fiser, I. Merunka, and J. Vrba, "Design, evaluation and validation of planar antenna array for breast hyperthermia treatment", in 2015 Conference on Microwave Techniques (COMITE), 2015, pp. 1–4. (cited: 1)
- O. Fiser, I. Merunka, and J. Vrba, "UWB waveguide breast tumor detection system based on delay and sum reconstruction algorithm", in Progress in Electromagnetics Research Symposium in Prague. Cambridge: Electromagnetics Academy, 2015, pp. 1506-1509.
- O. Fiser, et al. "Comparison of three UWB microwave antennas intended for brain stroke detection system" [online]. In: *Progress in Electromagnetic Research Symposium (PIERS).* 2016 Progress in Electromagnetic Research Symposium (PIERS). Shanghai, Cambridge, MA: The Electromagnetics Academy. 2016, s. 4648.
- I. Merunka, O. Fiser, J. Vrba, J. Vrba, and D. Vrba, "Comparative study of antennas for microwave tomography", in *2017 Progress In Electromagnetics Research Symposium - Spring (PIERS)*, 2017, pp. 727–731.
- I. Merunka, O. Fiser, L. Vojackova and J. Vrba, "Waveguide hyperthermia applicator with circular polarization", In: Progress in Electromagnetics Research Symposium in Prague. Cambridge: Electromagnetics Academy, 2015, pp. 2589-2592. ISSN 1559-9450. ISBN 9781934142301.
- I. Merunka, O. Fiser, and J. Vrba, "E-field distribution measurement system for hyperthermia applicators with LED sensor", in 2015 Conference on Microwave Techniques (COMITE), 2015, pp. 1–3.
- L. Vojackova, J. Vrba, O. Fiser, I. Merunka and K. Červinková, "Feasibility study of microwave interstitial applicator array for treatment pancreatic cancer", In: Progress in Electromagnetics Research Symposium in Prague. Cambridge: Electromagnetics Academy, 2015, pp. 2613-2617. ISSN 1559-9450. ISBN 9781934142301.
- L. Vojáčková, I. Merunka, O. Fišer, and J. Vrba, 'Interstitial applicators for breast cancer treatment by microwave thermoablation', in *2014 24th International Conference Radioelektronika*, 2014, pp. 1–4. (cited: 1)

Projects participation

International projects:

- **GAČR/17-20498J:** "Non-invasive temperature estimation inside of human body based on physical aspects of ultra-wideband microwave channel", 3-years project with DFG (2017-2019), supported by the Czech Science Foundation (Grant Agency of the Czech Republic), Member of the research team.
- **COST Action TD1301:** "Development of a European-based Collaborative Network to Accelerate Technological, Clinical and Commercialization Progress in the Area of Medical Microwave Imaging". Member of the research team.
- **COST Action BM1309:** "European network for innovative uses of EMFs in biomedical applications (EMF-MED)". Member of the research team.

Czech projects

- **GAČR/17-00477Y: "**Physical nature of interactions of EM fields generated by MTM structures with human body and study of their prospective use in medicine", 3-years project (2017-2019), supported by the Czech Science Foundation (Grant Agency of the Czech Republic), Member of the research team.
- **SGS17/182/OHK3/3T/13:** "Development of optical sensors and systems and microwave biomedical technologies", 3-years project (2017-2019), Member of the research team.
- **SGS14/189/OHK3/3T/13:** "Interaction of the EM field with biological systems and their applications in medicine", 3-years project (2014-2016), support of CTU in Prague. Member of the research team.

International awards

Second place: Best Student Paper Award, Piers 2017 (Progress in Electromagnetics Research Symposium v St. Petersburg (Russia)), category „Remote sensing, Inverse problems, Imaging, Radar and Sensing".

Membership in conference organizing committee

Member of organizing committee of PIERS 2015 (Progress in Electromagnetic Research, July 6 – 9, 2015, Prague, Czech Republic).

Short time scientific missions

8-11/2015, Technical University in Ilmenau, Germany

Topic: Temperature change detection using UWB radar

6/2017, Technical University in Ilmenau, Germany

Topic: Temperature dependence of dielectric parameters of used phantoms

Reviews of manuscripts for journal with IF

5x review for journal Radioengineering